INCORPORATION OF MAGNETIC RESONANCE IMAGING AND DIGITAL ANGIOGRAPHY IN THE APPLICATION OF STEREOTACTIC RADIOSURGERY

By

Soon Nyung Huh

A DISSERTATION PRESENTED TO THE GRADUATE SCHOOL
OF THE UNIVERSITY OF FLORIDA IN PARTIAL FULFILLMENT
OF THE REQUIREMENTS FOR THE DEGREE OF
DOCTOR OF PHILOSOPHY

UNIVERSITY OF FLORIDA

1994

ACKNOWLEDGEMENTS

I would like to express my sincere thanks to the members of my supervisory committee for their help and guidance throughout this work. I would like to give special thanks to my committee chairman, Dr. F. Bova, for his invaluable suggestions and sincere help through this research. I would also like to give special thanks to Dr. J. Fitzsimmons for invaluable suggestions about the custom-made head coil fabrication. Also I would like to thank Dr. W. Friedman for his kind explanation about the applications of the birdcage resonator and the MR-compatible BRW head ring for the radiosurgery, as well as valuable clinical information about the radiosurgery system during regular radiosurgery treatment. Special thanks should be given to Dr. G. Roessler, Dr. W. Properzio, Dr. J. Honeyman, and Dr. L. Fitzgerald for their discussions, corrections, and encouragement. I could not forget the kind help of the MR technologists, Ms. C. Meyer and Ms. M. Bentham, who helped to make possible the development of the BRW head ring and the birdcage head coil.

I would like to give special thanks to Ms. P. Mydock for her excellent job in proofreading the draft of this manuscript. I could not forget my fellow graduate students,

physicists, and doctors at Shands Cancer Center who encouraged me when I was struggling: K. Kalbaough, L. Ewald, R. Craig, T. Mitchell, R. Good, P. Somoneau, F. Harmon, S. Meeks, C. Yang, D. Moss, D. DeBois, R. Williams, H. Rao, Dr. M. Kasper, Dr. D. Blatt, Dr. M. Sombeck, Dr. J. Palta, Dr. M. Mclaughlin, Dr. W. Mendenhall, and Dr. N. Mendenhall.

TABLE OF CONTENTS

ACKNOWLEDGEMENTS ii

ABSTRACT vii

CHAPTERS

1 INTRODUCTION 1

Stereotactic Radiosurgery System 1
Historic Development of Radiosurgery 1
Linear Accelerator Based Radiosurgery System . . . 4

2 STEREOTACTIC RADIOSURGERY PROCEDURE 7

Stereotactic Radiosurgery Equipment 7
Patient Setup 9
CT Imaging Procedure 10
Angio Imaging Procedure 11
Imaging Registration for CT 12
Imaging Registration for Angiograms 18
Localization Procedure 18
Computer Treatment Planning 22
Quality Assurance (QA) 26
Patient Treatment 28

3 STATEMENT OF PROBLEMS AND LITERATURE SURVEY 31

Introduction 31
Literature Survey for MRI 34
Literature Survey for Digital Angiography 46

4 MR-COMPATIBLE BRW HEAD RING 57

Introduction 57
MR Water Phantom Fabrication 59
MR Imaging Technique and MR Unit 60
MR Images with Initial MR-Compatible BRW Head Ring 62
BRW Head Ring and Its Fixtures 64
Fixation Pin Fabrication 66

Clinical Application with MR-Compatible BRW Head Ring 69
Problem with Body Coil 71

5 CUSTOM-MADE HEAD COIL RESONATOR 73

Introduction to Birdcage Resonator 73
Design Concept 74
Structure of the Lowpass Version 76
Number of Rungs in the Birdcage Coil 79
Electrical Characteristics of the Birdcage Coil . 86
Theoretical Calculation of Birdcage Resonator . . 87
Characteristics of Copper Foil 88
Determination of Capacitors and Inductors 88
Impedance Matching Network 89
Electrical Characteristics of Siemens MR Scanner . 91
Tuning Procedure 92
Phantom Study of the Birdcage Coil 98
Clinical Application of the Birdcage Coil 98
Conclusion 100

6 ANALYSIS OF MR IMAGES WITH BIRDCAGE RESONATOR 102

Introduction 102
Specification of Imaging Parameters 104
Correlation between CT and MR Images 115
Conclusion 122

7 CORRELATION ANALYSIS 124

Introduction 124
Procedure for the Correspondence 128
Correlation with Radiosurgery Patients 130
Correlation with Depth Electrode Placement 133
Artifacts in MR Images 137
Conclusion for Correspondence 141

8 REGISTRATION OF MR IMAGES 143

Introduction 143
Review of Global Thresholding Technique 145
Registration Procedure 150
Overall Registration Procedure 158
Conclusion 159

9 DIGITAL RADIOGRAPHY 161

Introduction 161
Experimental Setup for Phantom Test 164
DA Target Phantom Information 167
Unwarping Algorithm 169

Conclusion 215

10 CONCLUSION AND FUTURE WORK 219

Introduction 219
Magnetic Resonance Imaging 220
Digital Angiography 222

APPENDICES

A Bio-Savart Law 223
B Signal-to-Noise Ratio 224
C Statistics in Background Noise 226
D Spatial Distortion of Digital Radiography 228

REFERENCE LIST 230

BIOGRAPHICAL SKETCH 240

Abstract of Dissertation Presented to the Graduate School of the University of Florida in Partial Fulfillment of the Requirements for the Degree of Doctor of Philosophy

INCORPORATION OF MAGNETIC RESONANCE IMAGING AND DIGITAL RADIOGRAPHY IN THE APPLICATION OF STEREOTACTIC RADIOSURGERY

By

Soon Nyung Huh

April, 1994

Chairperson: Frank J. Bova
Major Department: Nuclear Engineering Sciences

This paper outlines and implements a method of including magnetic resonance imaging and digital radiography as secondary imaging modalities for stereotactic radiosurgery. Computed tomography and film angiography have been used in University of Florida stereotactic radiosurgery. Magnetic resonance imaging can provide more clinical information than computed tomography, and digital radiography can provide more information about blood vessel structure than film angiography.

An MR-compatible BRW head ring and its fixtures are developed experimentally, and a custom-made head coil is fabricated. The experimental approach to fabricate the MR-compatible head ring and fixtures is introduced. The linear type birdcage resonator is developed, and the resultant images

are analyzed with a computer program. The correlation between computed tomography and magnetic resonance imaging is investigated using a water phantom and patients who are treated at the University of Florida.

The unwarping algorithm is developed to correct spatial distortion inherent in digital radiography. The unwarping algorithm with sub-pixel fiducial marker detection algorithm is tested with film radiography to examine the accuracy of the algorithm. The accuracy is found to be 0.4mm using a special phantom. Digital radiography can be fully used to study digital subtraction angiography as well as blood flow after the spatial distortion is removed by using the unwarping algorithm.

CHAPTER 1
INTRODUCTION

Stereotactic Radiosurgery System

Stereotactic radiosurgery is a technique for obliterating intracranial targets that are inaccessible or unsuitable for open surgical techniques, by means of well collimated beams of ionizing radiation. The main goal is to deliver a large dose of radiation to the target volume in the brain with a high degree of spatial accuracy, as well as to give a steep dose gradient to minimize the radiation dose to the rest of the brain. Targets usually occupy a relatively small volume of brain, less than 33 cubic centimeters (cc), and are inaccessible using conventional neurosurgery. In contrast to conventional radiotherapy techniques, where the prescribed dose of a few thousands of cGray is given in multiple fractions, in radiosurgery the target dose is given in one fraction. Therefore, the most important factor in the stereotactic radiosurgery is the physically determined concentration of the radiation on the target.

Historical Development of Radiosurgery

In 1951, the Swedish neurosurgeon Leksell built a

stereotactic instrument for radiological operations [Lek51]. An intracranial target could be irradiated through a large number of small, stationary portals by fixing a semicircular stereotactic frame at different angles and by moving a collimator along the frame. In 1955 Leksell began clinical studies, initially using 300kVp x-rays to treat functional disorders. Leksell first used the term "radiosurgery" in reference to the orthovoltage x-ray unit in 1951. Subsequently, the use of multiple, fixed, focal ^{60}Co gamma-ray sources was developed and designated the Gamma Knife. The first Gamma Knife was installed in 1968 and produced a more or less disc-shaped isodose distribution. In 1974, it was replaced with a second Gamma Knife that produced a more spherically shaped isodose distribution, which is more suitable for treatments of clinical targets. When fully loaded, the Gamma Knife contains about 5500 Curies of cobalt distributed in 201 sources over a portion of a hemisphere (extending an angle of +/- 48 degrees angle along the cephalocaudal direction and +/- 80 degrees along the right-to-left direction) such that circular beams from collimators of 4, 8, 12, and 18mm diameter enter the skull through a large number of points. The Gamma Knife has no moving parts once a patient is locked into place. There is no loss of focusing precision due to mechanical tolerance of moving parts in the radiation source or patient support assembly. It has been estimated that radiation beam accuracy is within +/- 0.3mm and

a helmet- locking inaccuracy is +/- 0.1mm. The overall mechanical accuracy of the 201 cobalt sources is within +/- 0.4mm [Lun89]. The accuracy between the radiation focus and the mechanical focus is within 0.25mm [Lux93].

In the 1940s, Wilson first suggested the medical usage of particle beams. Early radiosurgical groups utilized the proton beam produced by synchrocyclotrons. A Swedish group [Lar58] employed high-energy intersection proton beams analogous to the intersecting cobalt beams of the Gamma Knife. The use of high-energy proton or heavy-ion charged particle beams in place of photon beams as the radiation source results in an improved dose concentration in the targets. The physical property of particle beams is the sharp increase in ionization density (Bragg peak) that occurs near the end of the particle track. The potential suitability of high energy deuteron and alpha particles was first discussed by Tobias [Tob52]. The depth of the Bragg peak is determined by the particle energy; this can be decreased by placing material in the beam line upstream of the point of entry into the tissue. Multiple beams are used and their beam paths are fixed. The use of narrow, high-energy proton beams to produce sharply delineated lesions in experimental animals was described in a 1958 report from Uppsala [Lar58]. Groups in Boston and Berkeley used the Bragg peak effect to maximize the radiosurgical effectiveness of the proton beam. A 160MeV

proton beam with a 10mm wide Bragg peak was used in Boston [Kje77]. Generally, the radiation is delivered through twelve portals in one fraction. A 130MeV helium ion beam was used for radiosurgery with a synchrocyclotron at the Berkeley installation [Fab85]. Typically, the radiation is delivered to a dose of 25 to 45 Gy, through three to five entry points, in one to three fractions or treatment sessions. The limitation of this approach is the requirement of a synchrocyclotron to generate the radiation beam.

Linear Accelerator Based Radiosurgery System

The advent of modern brain imaging techniques in the mid-1970s, particularly CT scanning, led to the development of new stereotactic instruments, resulting in the resurgence of the stereotactic technique to localize intracranial structures.

In 1972 Larsson wrote that the choice between the roentgen and gamma radiation should be for technical, clinical, or economic reasons rather than physical considerations [Lar74]. The linear accelerator was developed in the United States and in Great Britain in the 1950s. During the 1980s, a number of investigators developed radiosurgical systems that utilized the linear accelerator

(linac) as the radiation source. Most linac-based radiosurgery systems rely upon an arching beam technique where a moving beam is always focusing on the stereotactically defined target. Most linac-based radiosurgery systems use multiple arcs of radiation with changes between arcs in either couch or patient position or in both of them. The dose distribution is similar to those produced by the Gamma Knife with the exception that most Linac systems have the ability to augment the basic arc set to produce nonspherical dose distribution.

Betti and his colleagues described, in 1984 [Bet84], a radiosurgical system using the linear accelerator as the source of radiation. A Talairach stereotactic device was used to position a patient's target at the isocenter of a 10MV beam from a linear accelerator. Reported isocentric accuracy was 0.8mm. Betti's system is unique because the patient is seated in a chair, which moves on rails to reposition the patient. In 1985 Colombo and associates [Col85] reported on a 4MV Varian linear accelerator based system with the linear accelerator collimator jaws used to adjust the desired field size. Detailed phantom studies demonstrated a maximum mechanical inaccuracy of 1.5mm. The dose fall-off was improved by developing multiple noncoplanar convergent arc techniques on the isocentric linear accelerator. In 1985 Hartmann reported a linear accelerator based system [Har85].

A Riechert-Mundinger type stereotactic device was used to position a patient's target at the isocenter of a 15MV beam from a Siemens linear accelerator. Tertiary collimation was achieved using a circular tungsten collimator of 2 to 20mm in diameter. In 1979, the Brown-Roberts-Wells (BRW) image-guided stereotactic system was developed at the University of Utah. The precision adaptation of the BRW system to a standard linear accelerator by Winston and Lutz at Harvard in 1986 demonstrated that radiation can be delivered with an accuracy of 0.5mm +/- 0.2mm with a properly adapted and calibrated linear accelerator [Lut88]. In 1988, Podgorsak et al. [Pod88] reported a linac radiosurgery system in use in Montreal, Canada. A Oliver-Bertrand-Talairach (OBT) frame and tertiary circular collimators were used for stereotactically identifying a target. This system is unique in that a treatment couch rotates 150 degrees while the gantry rotates 300 degrees. This dynamic radiosurgery produces a dose gradient very similar to that of the Gamma knife.

In 1989 Friedman and Bova at the University of Florida developed a three-axis bearing system with the BRW stereotactic instrument to couple a tertiary collimator to the head of the linear accelerator, increasing the accuracy to 0.2mm +/- 0.1mm [Fri89]. To date this is the most accurate system reported in the literature.

CHAPTER 2
STEREOTACTIC RADIOSURGERY PROCEDURE

Stereotactic Radiosurgery Equipment

There are four major components of the University of Florida (UF) Stereotactic Radiosurgery System: a linear accelerator, a stereotactic system, a mechanical stand, and a computer treatment planning system. A standard 6MV Philips linear accelerator (SL75/5) is used to treat conventional radiation therapy patients, and is converted for Stereotactic Radiosurgery System use by attaching a three-axis bearing system and a tertiary collimator.

The UF stereotactic system consists of several pieces of equipment: a Brown-Roberts-Wells (BRW) head ring, a computed-tomography (CT) localizer, an angiography (angio) localizer, a CT table adapter, and an angio support. The BRW head ring is fixed to a patient's skull to provide a rigid reference frame. The CT localizer is then locked onto the BRW head ring before scanning for the determination of BRW coordinates. The CT table adapter is attached to the CT scanner table, which fixes the BRW head ring and the patient's skull for the scanning procedure. The scanning procedure takes

approximately 15 minutes with the GE9800 Advantage™ scanner. The CT imaging procedure is performed for vascular and nonvascular diseases and used for target identification as well as dosimetry. Vascular diseases such as arteriovenous malformation (AVM) require the angio support to be attached to the BRW head ring. The angio localizer is then locked onto the BRW head ring before the angiographic procedure. The angio support is used to prevent patient motion during long angiographic imaging procedures. Angiographic examinations lasting more than one hour are common. The BRW head ring will be attached to the patient's skull until the radiation treatment is completed.

The mechanical stand of the linear accelerator has a swinging arm to hold the tertiary collimator for precise delievery of the radiation to the target. The BRW head ring, attached to the patient skull, is screwed to the supporter on the top of the mechanical system. By adjusting three vernier screws (adjusting x, y, and z axes corresponding to the anterior/posterior, lateral, and axial coordinates of the BRW coordinates), the center of the target is placed on the isocenter of the linear accelerator within an accuracy of 0.2mm. The patient couch is rotated about the isocenter of the linear accelerator. A high precision three bearing system holds the tertiary collimator, which is focused on the isocenter of the linear accelerator. A gimble system allows

the tertiary collimator to follow the movement of the treatment head of the linear accelerator by decoupling the gantry sagging up to 2mm, which is common to standard linear accelerators.

The computer treatment planning system runs on a SUN SPARC station using the X-window environment. Currently, two imaging modalities are used to determine the target volume and position in terms of BRW coordinates. CT images are used to define the target for the treatment of solid tumors. Initially, for cases involving vascular targets such as arteriovenous malformations (AVM), biplane scout films are used to define the center position of the AVM and to estimate the projected lesion size on each view. However, because of inadequate target information (such as AVM) the CT images are also used to estimate the target position and volume [Bov89]. The high dose region is conformed to the target volume by altering various treatment parameters of the stereotactic radiosurgery system, for example, number of arcs, arc weights, start and stop angle of each arc, number of isocenters, the distance between isocenters, isodose prescription line to cover the target, etc.

Patient Seup

The patient is seen in a clinic exam room where the BRW

head ring is attached onto the patient skull. Four localization pins in the pin supporters attach the BRW head ring to the patient's skull. This procedure is carried out under local anesthesia. Before fixing the localization pins, the CT localizer is placed onto the BRW head ring to see that the top of the CT localizer cage will be above the top of the patient head. Therefore, the beam path of each arc for dosimetry can be determined in the CT images.

CT Imaging Procedure

CT imaging is done on a GE9800 Advantage™ using standard techniques for head scanning, with 5 mm/1 mm scanning thickness without overlapping, 34.5 cm field-of-view (FOV), and 512*512 resolution. The inplane resolution is 0.67 mm and the axial resolution is either 5 mm or 1 mm depending upon the target position. The bracket is used to fix the BRW ring onto the CT scanning table for immobilization purpose. The CT localization cage is attached onto the BRW head ring.

Scout views are taken to determine the axis tilt angle, which is defined as the angle between the z-axis of the BRW coordinates and the CT scanner. It can be adjusted in increments of 0.5 degrees. This tilt angle adjustment is not mandatory, but it eliminates the rotation or spinning

procedure during the image reconstruction process. Therefore, the x and y coordinates of the CT images can be directly registered to the AP and lateral coordinates of the BRW coordinates system. The CT images are directly used without the rotation procedure when the orthogonal views (anterior/posterior, lateral, and trans-axial) are examined during the computer treatment planning procedure. The slice thickness is 5 mm for the trans-axial planes that do not cover the target (above or below the target), and the slice thickness is reduced to 1 mm in the planes which do cover the target volume. Therefore, the in-plane pixel width is 0.67 mm (345 mm/512) and the axial pixel width is 1 mm. These resolutions are on the order of the inaccuracy (approximately 1 mm) of cranial target identification based upon radiological imaging [Lux93].

Angio Imaging Procedure

Historically, the standard procedure for the target identification of an arteriovenous malformation (AVM) is a set of an AP and lateral angiograms. The patient is placed in a supine position on the exam table. To immobilize the patient during the angiogram procedure an angio bracket is used to hold the BRW head ring.

A radiologist performs the selective femoral

catheterization procedure. The scout films are taken without any contrast agent to insure that possible target position and fiducial markers are captured in the anterior/posterior (AP) and the lateral views. If these are not present, the patient is readjusted and the scout images are obtained. A series of angiograms is obtained while the contrast materials are being injected. Cut films are used in the AP and lateral views. Filming rates of up to four films per second are utilized. This rate is the maximum of the conventional angiography unit. The timing relationship between the AP and the lateral views is shown in Figure 2.1. The timing delay between the AP and lateral views is a potential source of ambiguity when the target position is reconstructed from the two sets of biplane film angiograms. Because of the fast movement of the contrast material in the AVM, different structures of the AVM are taken in the AP and lateral view. Sixteen sets of images are usually obtained for each view. A neurosurgeon and a neuro radiologist select one set of the film that best displays the target. This set of films is used to define the nidus of the AVM in the stereotactic coordinates.

Image Registration for CT Images

A CT localizer cage is the main device to register the CT images in BRW coordinates. The CT localizer consists of

six vertical rods equally spaced around the BRW head ring

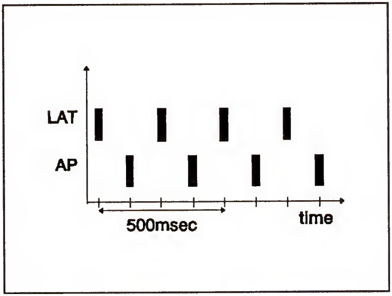

Figure 2.1 Timing Relationship between AP and lateral view. Four sets of angiograms per second are usually obtained. The time delay between the AP and lateral views is approximately 125msec.

and three additional slanting rods, joining each pair of the vertical rods, forming an N-shaped configuration as shown in Fig. 2.2. The relationship between the two coordinates has been described by Saw [Saw87]. The coordinate transformation equation in Cheng's paper is used to register the CT images in the BRW coordinates. The z coordinates of the rod 2, 5, and 8 are modified to set the center of the CT localizer to axial coordinate of 0 mm. The transformation equations are rewritten below:

For Rod2: $X_2 = D*[1-(q/Q)*\cos 60^0]$ Eq.2.1.

$Y_2 = D*(q/Q)*\sin60^0$ $\qquad$ $Z_2 = [(q/Q)-0.5)*H$

For Rod5: $X_5 = D*[\{1-(q/Q)\}*\cos60^0-1]$

$Y_5 = D*[1-(q/Q)]*\sin60^0$ $\qquad$ $Z_5 = [(q/Q)-0.5)*H$

For Rod8: $X_8 = D*[(q/Q)-0.5]$

$Y_8 = -D*\cos30^0$ $\qquad$ $Z_8 = [(q/Q)-0.5]*H$

Where, D and H is the diameter of the CT localizer (140 mm), the height of the CT localizer (190 mm), and q and Q are described in the Fig. 2.2

There are three major parameters that define the geometric orientation of the localizer in BRW coordinates: (1) image spin angle, (2) axis tilt angle, and (3) flatness factor. The image spin angle is defined as the angle by which the line formed by rods 1 and 6 deviates from the horizontal in the CT image plane. The image spin angle and the axis tilt angle (will be explained later in this section) are used to spin or rotate the CT images. Thus, the CT images can be directly used during the computer treatment planning procedure without repeating rotation or spin when the dose distribution in one of three orthogonal planes is examined. Image spin angle compensation is not considered unless the image spin angle is greater than 0.385 degrees.

The CT bracket is set to keep the image spin angle within 0.385 degrees. The axis tilt angle is defined

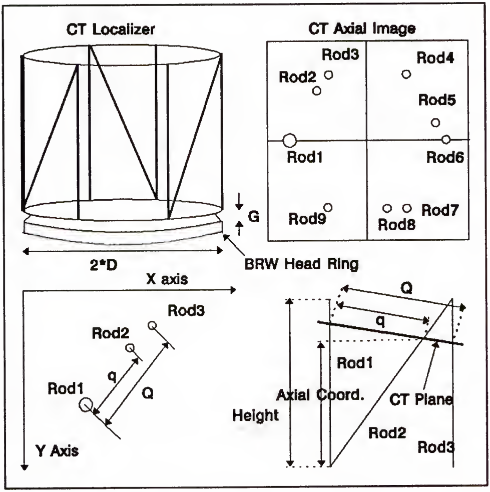

Fig. 2.2 The geometry of BRW coordinates and a cross section of the CT localizer and the relationship between CT and BRW coordinates [Saw87]. Rod 2, 5 and 8 are the slanting rods and other rods are straight rods. D is the distance between rod 1 and rod 6 (28 cm) and the Height (19 cm) is the height of the N-shaped rods. The ratio (q/Q) is the ratio of the distances from a slanted and a vertical rod to the other vertical rod. The G is the gap (8 mm) between the CT localizer and the top of the BRW head ring. The center of the localizer is the origin of the stereotactic coordinate.

as the angle between the z-axis of BRW coordinates and the axis normal to the CT imaging plane. Also, the axis tilt angle is ignored when it is less than 0.385 degrees. The specifications of the image spin and the axis tilt angle represent one pixel (about 0.67 mm) deviation over 10cm distance (one half of a typical skull size). The image spin angle and the axis tilt angle are shown in Figure 2.3.

Three angles are needed to relate precisely the axis of the CT localizer and the axis normal to the CT imaging plane. The image spin and the axis tilt angles are always less than 0.385 degrees for CT images. The weight of the head could produce a tilt angle larger than 2 degrees. In this case the angle is compensated for by setting the scanning plane in the CT images to be parallel with the top of the CT localizer.

The flatness is defined as the deviation of one of three distances between two sets of straight opposite rods (for example, the distance between rod 1 and rod 6) from the average of three distances. The flatness is less than one pixel for CT images because of linear characteristics of the CT images. This is a convenient measure of the nonlinearity of MR images and is investigated in the chapter 6.

Once each slice of the CT images is registered in the

stereotactic coordinates, background is clipped. The middle portion of the CT image showing anatomical structures is selected in order to minimize the memory requirements. The coronal and sagittal images are reconstructed from trans-axial images. These reconstructed images are used to define the tumor in the sagittal and coronal views as well as to display the dose distribution when the treatment planning is performed.

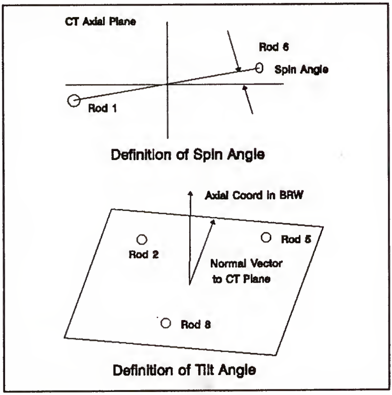

Figure 2.3 Definition of the Image Spin and Axis Tilt Angle
The image spin angle is defined as the angle between two lines. One line is determined by connecting the centers of rod 1 and rod 6. The other line is the horizontal plane of the CT imaging plane. The axis tilt angle is the angle between two vectors. One vector is defined as the normal vector to the plane, which is defined by three points in the stereotactic coordinates.

Image Registration for Angiograms

Target localization is accomplished with a specially designed intracranial localizer box that is rigidly attached to the BRW head ring. The localizer box is shown in Figure 2.4. Four radio-opaque markers, in a rectangular configuration, are fixed to each of the anterior, posterior, right, and left faces on the angio localizer box. The coordinates of the sixteen markers are precisely known with respect to the BRW coordinates. Four radio-opaque markers in each plate forms the vertices of a square with 6.0 cm sides. In order to locate the target center precisely, target position and magnification factor should be determined; a detailed procedure for projective geometry is described by Siddon [Sid89].

Localization Procedure

The boundary of the AVM is drawn on the AP and the lateral films by a neurosurgeon, and the eight fiducial markers are defined using a digitizer. This information is digitized to the computer to calculate the target position in BRW coordinates. Three algorithms can be used to calculate the center of the AVM: the center of the mass, the geometric center (GC), and the user-defined center (UC). For many stereotactic radiosurgeries the GC of the target is

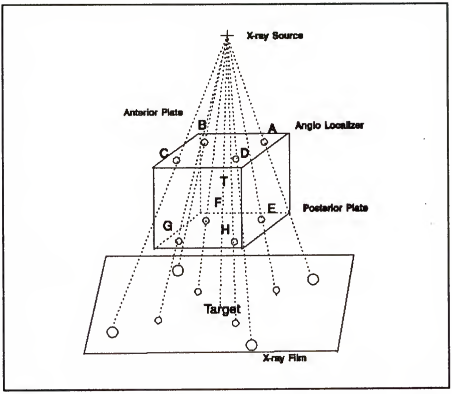

Figure 2.4. Angio Localizer for AP film. The fiducial markers of the anterior plate are represented by A, B, C, D and those of the posterior plate by E, F, G, H. The point target is represented by T. For the AP view, eight fiducial markers and a target are usually utilized to determine the magnification factor and the target position with those of the lateral view.

used as a starting point for dose planning procedure. The GC of the target is determined by placing the target at the center of the smallest sphere that fully circumscribes the target. This procedure is performed for each view. If the centers of these two circles are projected back toward the x-ray source and if the target is consistent, they intersect at the target's GC. However, if the projection of these two

targets seldom meet, the result is the skew distance. This distance is the closest distance between the projected lines. The skew distance is shown in Fig. 2.5. A detailed explanation of skew distance is given by Siddon [Sid87]. The skew distance is a very sensitive indicator of possible erroneous data input. For correct and consistent data entry, the skew distance is typically less than 1.0 mm with a point target.

There are four major reasons for interpreting the nidus differently on the two views: (1) different overlapping with arteries, veins, and the nidus, (2) timing differences between two views (see Fig. 2.1), (3) inadequate definition of different vascular components, and (4) planar projection of a three dimensional structure. Bova [Bov89] and Spiegelman [Spi92] explain in detail the possible sources of introducing errors in identifying the target center.

CT images are used to define both vascular and solid tumor in three dimensional views. This localization procedure is carried out using three planes of the CT images: trans-axial (or axial), sagittal, and coronal planes. The target boundary is drawn in each plane by a neurosurgeon. The GC, CM, and UC are defined in each plane and the skew distances are calculated from any two or three views. When three views are used, three possible center

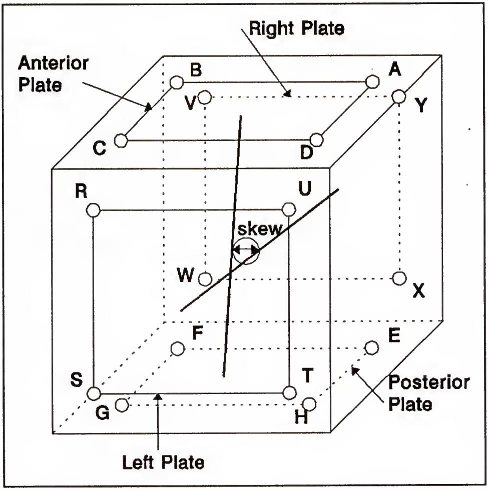

Figure 2.5 Definition of the Skew Distance. The small circle represents the shortest distance between two projected lines.

skull is contoured automatically, and the ray path along each depth of the arc is computed and displayed. A dose model, whose parameters include tissue path length, off-axis distance, field size, and x-ray source-to-point distance, is used to compute the dose distribution generated by that arc [Suh90]. The user then selects additional arcing planes or modifies the preselected plane and repeats this procedure.

positions of the vascular or solid tumor from any two sets of planes are averaged. When two views are used, the skew distances are examined and one set of two planes giving the smallest skew distance is chosen for the starting point of the target position and the target size for the dose planning procedure. The target size is used to determine the initial collimator for the standard nine arc dose plan. In the case of a spherical vascular or solid tumor, this approach is very effective to estimate the target position as well as the collimator size. However, in the case of a complex shape tumor, the tumor is first divided into two or three regions; different collimator size is tried on each based upon the size as well as the separation between two or three regions of the complex tumor.

Computer Treatment Planning

The target center is imported from the localization procedure mentioned in the earlier section: the target center of the AVM is imported from the angio localization and that of the solid tumor is imported from the CT localization procedure. The first step in the computer treatment planning process is the selection of arcing planes. The computer reconstructs an image plane through which the center of the arcing radiation will pass. A user selects start and stop angles for the radiation beam. The

For the spherical tumor, the standard nine arc plan (see Fig. 2.6) is applied to review overall dose distribution to the tumor as well as neighboring tissue. The plan variables of this standard nine arc plan are shown in Table 2.1 and each arc is represented on a reconstructed view of the skull. Note that the table angles describe nine equally spaced arc positions; all arcs are 100 degrees (start to stop angle), weight for each arc and collimator size, target position in trans-axial, coronal, sagittal plane. The initial collimator size is determined by the previously described localization procedures. The collimator factor is defined as the dose at the depth of dmax as a function of collimator size, normalized to unity for a standard field size, e.g., 10cm*10cm field size. Plan variables may be changed to give uniform dose distribution over the target, to avoid radiation exposure to a critical organ, or to increase the dose gradient in a specific anatomical direction.

The standard five arc plan is a frequently used variation of the standard nine arc plan. The four arcs of the standard nine arc plan with table angles of 50, 70, 330, and 350 degrees are eliminated (see Table 2.1 and Fig. 2.6). When a critical structure lies lateral to the isocenter, one may need to steepen the lateral dose gradient. This can be done by eliminating the arcs' planes that pass through that

region, i.e., most lateral arcs. This will increase the gradient of the lateral distribution, and it will increase the relative weights to the remaining arcs.

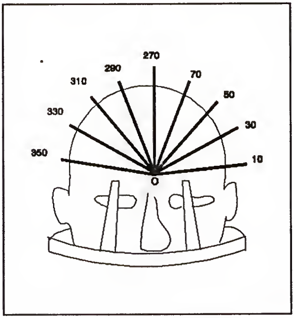

Fig. 2.6 Arc Orientation of the Standard Nine Arc Plan. The numbers of each arc represents the table angles and 0 represents a single isocenter. The gantry rotates 100 degrees for each arc.

For an irregularly shaped tumor, multiple isocenters are used with two or three sets of five to nine arc plans in order to cover the target volume with uniform dose distribution. The separation distances between isocenters and positions of each isocenter are determined heuristically by the shape of the tumor as well as the relationships between the target and critical organs. For each arc plan,

the following parameters may be changed: start and stop angles, table angle, isocenter position, collimator size, and arc weights. The dose distributions in three planes are examined with different plan variables until the optimum plan is obtained. Dose profiles and dose volume histogram (DVH) within the target volume are also reviewed to see that the target volume is uniformly irradiated and there is no significant radiation outside the target volume. The DVH can reveal significant differences between treatment alternatives. For the treatment plan that includes two or three isocenters, the nine arc plan is replaced by a five arc plan in order to decrease the treatment time. The plan variables of the five arc plan are shown in Table 2.2. There is no clinical difference between the nine arc plan and the five arc plan above the twenty percent isodose level.

According to the University of Florida radiosurgery treatment protocol, radiation dosages are frequently prescribed in 250 cGy increments from 750 to 2500 cGY. The radiation dose is prescribed to a percentage isodose line. For a single isocenter, eighty or ninety percent isodose lines are used. For multiple isocenters, a seventy percent isodose line is frequently used. Prescriptions also depend upon collimator size, previous radiation treatment, number of isocenters, tumor type, tumor location, etc. Plan

optimization is done by the visual, iterative method. This procedure can take an hour in the case of complex shaped targets.

Quality Assurance (QA)

The stereotactic radiosurgery system is attached to the linear accelerator (SL75-5, 6MV Philips system). The linac is also used to treat conventional radiation therapy patients. X-ray jaws of the linac are set to 5 cm*5 cm, and gantry and collimator angles of the linear accelerator are set to zero degrees. The gimble bearing is attached on the treatment head with four screws (see Fig. 2.7) [Bov89]. The tertiary circular collimator is inserted onto the rotating arms of the mechanical subsystem. The head of the BRW floor stand is adjusted so that the isocenter of the linac coincides with the isocenter selected by the computer treatment planning. Also the target phantom (see Fig. 2.7) is adjusted on a phantom base so that the target is set to the isocenter of the linac. The target phantom is screwed to the head of BRW floor stand. Before exposing the x-ray film for the quality check, the light field of the linear accelerator is turned on and the precession of the shadow of the target phantom on the film is observed while the isocentric subsystem (ISS) is rotated. If the presession is

observed, the target phantom and the head of the BRW floor stand are readjusted. The machine setup is shown in Figure 2.6.

Table 2.1 Standard Nine Arc plan

No	Collimator Size (cm)	Collimator Factor	Table Angle	Start Angle	End Angle	Arc Weight
1	10	0.840	10^0	130^0	30^0	100
2	10	0.840	30^0	130^0	30^0	100
3	10	0.840	50^0	130^0	30^0	100
4	10	0.840	70^0	130^0	30^0	100
5	10	0.840	350^0	130^0	30^0	100
6	10	0.840	330^0	230^0	330^0	100
7	10	0.840	310^0	230^0	330^0	100
8	10	0.840	290^0	230^0	330^0	100
9	10	0.840	270^0	230^0	330^0	100

Table 2.2 Five Arc Plan.

No	Collimator Size	Collimator factor	Table Angle	Start Angle	End Angle	Arc Weight
1	10	0.840	25^0	130^0	30^0	100
2	10	0.840	55^0	130^0	30^0	100
3	10	0.840	335^0	330^0	230^0	100
4	10	0.840	305^0	330^0	230^0	100
5	10	0.840	270^0	330^0	230^0	100

A series of x-ray films are taken at multiple couch, table, and gantry angles with the steel ball target on the isocenter. The gantry and the table angles in Table 2.3 are used to make sure that the isocenter of the tumor is on the isocenter of the linear accelerator. The differences between the center of the steel ball target and the center of the radiation fields are reviewed to verify the proper setup of the mechanical system. It takes about fifteen minutes to do this quality assurance.

Patient Treatment

The patient is brought into the treatment room and attached to the head stand. The treatment procedure is explained to the patient, treatment then proceeds as defined by the computer treatment plan. At the conclusion of treatment, the BRW head ring is removed and the patient is free to leave. For those patients who have undergone the angio localization procedure, there is a minimum time span of six hours required for post-angio observation before they leave. Follow up consultation and angiography takes place usually at six month intervals.

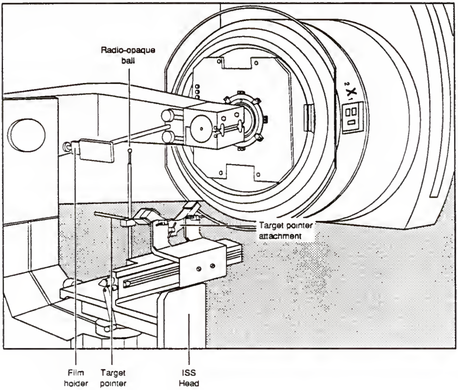

Figure 2.7 Setup for Isocenter Verification [Phi92].
The target phantom (consisting of a radio-opaque ball and a target pointer) are separately adjusted on the phantom base, which is not shown in this figure. After the target phantom and the ISS head are adjusted, the shadow of the radio-opaque ball on the film holder is observed.

Table 2.3 Table and Gantry Setup for QA Procedure

Exposure	Gantry Angle	Table Angle
1	270^0	0^0
2	225^0	-45^0
3	225^0	-90^0
4	315^0	-90^0
5	315^0	-45^0
6	90^0	0^0
7	135^0	45^0
8	45^0	45^0

CHAPTER 3
STATEMENTS OF PROBLEMS AND LITERATURE SURVEY

Introduction

The current University of Florida (UF) stereotactic radiosurgery system includes CT images and conventional biplane film angiography. This system has been successfully used to treat about 250 patients with arteriovenous malformations (AVM) and tumors (acoustics, meningioma, glioblastoma, metastatic diseases and pituitary tumors). To aid in the definition of the target tissues, magnetic resonance imaging (MRI) is needed as a secondary imaging modality. Digital radiography is also needed to take advantage of the digital image processing capability such as mask subtraction, dual energy subtraction, time interval differencing and temporal filtering. Mask subtraction is the most common at present, but other three remaining techniques are beginning to see clinical use.

However, the direct use of the MR imaging modalities was not possible with the initial BRW system. The ferromagnetic materials, used to fabricate the CT localizer and the BRW head ring and its fixtures (see chapter 4 for detailed components for the BRW head ring), were not compatible with the MR unit.

Therefore, MR-compatible materials had to be found while satisfying the mechanical strength of the head ring. In chapter 4, the materials for the MR Localizer (geometrically the same as the CT localizer) and the MR-compatible BRW head ring (MR BRW head ring) and its fixtures are found experimentally and images thus obtained are analyzed with standard MR scanning techniques.

The standard head coil could not be used with the MR localizer because of its bulky size (about 300mm diameter and more than 200 mm height including the MR BRW head ring and the MR localizer). The body coil built into an MR unit was used, resulting in low signal-to-noise ratio (SNR). In order to improve SNR, 5mm slice thickness has been used with the body coil, causing low axial resolution while keeping the same in-plane resolution (512*512 matrix with 345mm Field-of-View). The inplane resolution is 0.67 mm and the axial resolution is 5 mm. Thus, the custom-made head coil called "the linear type birdcage resonator" was developed to improve the SNR, thus improving the axial resolution to 3 mm. 3 mm is the minimum slice thickness used with spin-echo pulse sequence and 0.9 mm is the minimum slice thickness with 3D imaging sequence using the Siemens MagnetomTM SP4000 Scanner. The detailed procedure to design the linear type birdcage resonator will be presented in chapter 5.

Digital subtraction angiography (DSA) is the generic term for any digital radiographic method of implementing subtraction angiography. Many digital imaging processing techniques can be applied to DSA, for example, amplification of the low-concentration intravascular contrast signals to visible levels for diagnosis of major vascular disorders (for example, AVM). DSA consists of x-ray equipment and high-speed image processing equipment. The x-ray equipment is a combination of x-ray generator and a large-field image intensifier coupled to television (TV) camera. The signal from the TV camera is digitized and fed to an image processing computer system. The description of x-ray generator and x-ray tube is given in depth given in many places [Cur90] [Kru80] [See85] [Fol85] [Ovi85] [Cur90].

The image processing equipment includes several characteristics: (1) real time image acquisition capability up to 30 frames per second, (2) various digital imaging processing capabilities, for example, edge enhancement, frame averaging, mask subtraction, image enhancement, time interval differencing, temporal filtering, preprocessing and postprocessing [Ovi85] [Rit85] [See85] [Ter83] [Van88] and (3) dual energy subtraction. However, these capabilities could not be directly utilized for stereotactic radiosurgery system due to required high level of accuracy (approximately 1 mm). This high level of accuracy could not be achieved because of

spatial distortions (including internal and external sources) and the resolution limit inherent in finite digital images [Lov87] [Nai87].

Literature Survey for MRI

Because of the different physiological information provided by MR imaging, several groups have developed MR-compatible frames which can be used with the CT and MR imaging procedures. There are many factors to evaluate the MR-compatible stereotactic instrument: (1) artifacts due to the stereotactic frame and its fixtures (for example, localization pins), (2) coordinate determination procedure to take care of spatial distortion, fiducial marker detection procedure or coordinate determination procedure, (3) inplane and axial-plane resolution (matrix size FOV and slice thickness), for example, on the order of 1mm, (4) material of the fiducial markers, (5) type of the head coil, (6) MR scanning techniques (3D vs 2D scanning) and (7) main magnetic field strength (0.5 to 1.5 Tesla). These factors are not independent from each other, but related to each other factor.

The materials used to make the stereotactic instrument and its fixtures should be non-ferromagnetic and should not affect the fiducial markers. The fiducial markers are easily affected by the metal type of the stereotactic frame because

a portion of those fiducial markers are close to the frame. This might be related to radio-frequency (RF) interaction of the frame with the fiducial markers. Therefore, the interaction of the frame with the dynamic RF fields (called the eddy current effects) should be examined as well as with the static magnetic field, which are both determined by the main magnetic fields (usually 0.5 to 1.5 Tesla MR unit).

The materials for the fiducial markers should be carefully chosen so that the fiducial markers are shown in MR images with different scanning techniques: (1) T1, (2) T2 and (3) proton-weighted imaging. The proton-weighted imaging is rarely used because of lack of pathological information. Diluted $CuSO_4$ solution and propylene glycol (1,2-propanediol, $C_0H_8O_2$) are used inside the fiducial marker tubes as a contrast agent, thereby insuring the fiducial markers show up as bright spots. The detailed information about the concentration of the diluted $CuSO_4$ and the propylene solution is examined by Price [Pri90].

The slice thickness determines the axial resolution. The slice thickness is limited to 3 mm when the SE sequence is used. Although it is possible to use smaller slice thickness, but the scan time required is prohibitive with the required image matrix size of 512*512. The slice thickness can be reduced to less than 1 mm when 3D volume imaging systems (for

example, gradient recalled acquisition imaging technique or fast imaging with steady state free precession) is used [Sie89]. However, the 3D imaging technique does not compensate for phase reversal, causing dark signals in the region where two regions with different susceptibilities meet. The 3D imaging techniques are frequently used to examine AVM or solid tumors. The real advantage of the 3D imaging procedure is the higher resolution (less than 1 mm) compared with that of SE procedure (3 mm slice thickness). Therefore, resolution in three planes are on the order of 1 mm.

To increase SNR a custom-made head coil is a necessary component for stereotactic MR scanning. Two types of head coil fabrication are commonly used in MR imaging: (1) birdcage resonator and (2) saddle type resonator. The saddle coil had been used to implement the standard head or knee coils. There are many publications about the theoretical approach of designing the head coil [Hay85] [Wat88] [Tro89] [Har91]. The birdcage resonator is very frequently used in spectroscopy applications demanding high level of uniformity at the center of the samples under test [Cal91]. The saddle coil is commonly used to implement the standard head coils. Since spatial resolution is critical in scanning for radiosurgery the birdcage resonator has been chosen even though the birdcage resonator is more difficult to fabricate than the saddle coil.

The first MR system in the stereotactic surgery was used for an MRI-guided stereotactic brain biopsy procedure [Hei87]. A body coil with 192*256 matrix size, TR=600 msec, TE=15 msec, FOV=280 mm, slice thickness=10 mm and distance factor=0 is used with the modified BRW stereotactic frame (anodized aluminum) and T1, T2 and proton-weighted imaging. Eddy current effects are eliminated by splitting the BRW ring into two pieces and filling the split with non-metallic insert to maintain rigidity. MR localizer box is made of polycarbonated rods with petroleum jelly (contrast material). The structure of the stereotactic instrument allowed retrieval of information in three planes of reference. The major problem with this system was that the slice thickness was too large for stereotactic radiosurgery, even though the inplane accuracy (on the order of 1mm) was acceptable. In order to use this system, a special head coil should be developed in order to decrease the slice thickness.

Schad et al. [Sch92] used MR Angiography (MRA) for stereotactic planning. They presented an MRA-based planning method for the treatment of AVM by stereotactic radiosurgery. Flow-compensated gradient echo pulse sequence is used for the acquisition of angiographic MR images. The system also includes a stereotactic marker system and an algorithm to correct geometric distortion of the MR images. Imaging is performed on a whole-body MR scanner operating at 1.5 Tesla

field strength. The 2D parameters used are: 2D fast low angle shot (FLASH) sequence with 30 msec TR, 10 msec TE and 60 degree flip angle. The 3D parameters used are: 3D fast imaging with steady precession (FISP) sequence with 35msec TR, 7msec TE and 15 degree flip angle. Depending upon the volume size to be imaged, one to three overlapping datasets are acquired with a slice thickness of 1 mm. For both techniques, a field of view of 265 mm is used, thus giving inplane resolution of approximately 1 mm. The localizer system, which is based upon the Riechert and Mundinger stereotactic head frame, includes a wooden base ring fixed to the patient's head with an individually adaptable face mold or with carbon fiber pins. The unique feature of this system is the distortion correction algorithm to remove the spatial distortion and the 3D imaging procedure to increase axial resolution up to 1 mm. This system uses a custom-made head coil. The imaging quality of the head coil was not presented.

The work of Schad et al. has several interesting points: (1) MRA is used to define an AVM rather than using angiography, (2) the 3D voxel size is 1 mm*1 mm*1 mm the same resolution in three coordinates and (3) 2D and 3D phantoms are used to correct spatial distortion with 4th order 2D polynomials, improving the displacement errors from 3mm to 1mm. This correction algorithm is based upon "global correction" rather than adaptive local correction, which is

used to correct the inhomogeneity and nonlinear gradient magnetic fields, excluding the susceptibility artifact due to patients. (4) the custom-made head coil (31 cm diameter and linear polarized head coil) with wooden head ring was developed, while most institutions use the metal rings.

Yanahima et al. [Yan89] developed MRI-guided stereotactic radiosurgery for functional neurosurgery using a Toshiba MRT-50A unit (0.5 Tesla) as the scanning system. They used a Komai-type stereotactic frame made of non-magnetic materials with spin-echo (SE) sequence. This approach has some disadvantages for local use: (1) Koami-type stereotactic unit is not compatible with the UF stereotactic radiosurgery system and (2) they use the body coil instead of custom-made coil.

Henri et al. [Hen90] reported in 1980 MR-compatible Oliver-Bertrand-Talairach (OBT) stereotactic frame, which is equipped with various apparati: anterior and posterior digital substraction angiography (DSA) fiducial marker plate. MR images are obtained using 1.5 Tesla whole-body imaging with T1-weighted 2D-multislice acquisitions, and 256*256*12 bits. The scan thickness is less than 5 mm in a 325 mm field-of-view (FOV). A series of interchangeable fiducial marker plates exist for each imaging modality (CT/MRI/DSA) and are attached during imaging, while the OBT frame is in place on a patient's head. They developed a simple matching algorithm to correlate

CT/DSA and MR/DSA with linear interpolation and implemented sub-pixel accuracy of the fully automatic matching procedure, by superimposing the DSA images onto translucent volume-rendered CT/MR images. The mean error difference of the matching procedure was 0.7 mm (0.6 pixels) in the imaging plane. To date this is the only reported matching procedure between CT/DSA and MR/DSA and stereoscopic target localization. This group used the smaller matrix (256*256) with larger slice thickness (greater than 3 mm) with body coil in order to maintain high SNR. The axial resolution is larger than 3 mm. From their presentation, the automatic matching procedure with subpixel accuracy and volume rendering technique was applied to superimposing DSA onto CT/MR images. This matching procedure introduced a method of 3D volume visualization in an area dominated by the 2D methods of imaging analysis. No special coordinate determination and no error analysis between CT and MR images was done.

Levesque et al. [Lev90] used a modified Leksell OBT stereotactic frame. This system is compatible with CT, MRI, DSA, and PET imaging. Aluminum tubing is used during CT scanning and copper sulfate solution (7 gm/l) is used in the tube channel for MR images. For PET scans the tube channel is filled with a gallium emitter. For DSA, the fiducial markers consist of four 1mm stainless steel disks placed at the four quadrants. MR images are obtained on a 0.3 Tesla MR Unit

(Model B3000, manufactured by FONAR Corp.) using a custom-made surface coil. The scanning technique is Inversion Recovery (IR) with TR=300 msec, TE=30msec, 512*256 matrix size, and 5 mm slice thickness. The reported geometric distortion is 1 mm in any plane with agreement between the computerized coordinate system and phantom targets. The accuracy and linearity of the MR stereotactic imaging shows a maximum distortion of +/-1 mm on sagittal MR images at the field peripheral. The smaller magnetic fields has a greater potential of introducing smaller spatial distortion, even though the slice thickness is 5 mm and one of the inplane resolutions is larger than 1mm.

Heilbrun et al. [Hei87] modified the BRW CT stereotactic guidance system to accommodate MR imaging. A smaller head ring, which fits in standard MR head coils, is constructed of a non-ferromagnetic aluminum ring that is split into two pieces and is anodized to prevent eddy current effects. This system was tested using a water phantom with T1 and T2-weighed pulse sequences. Also carbon posts and pins are replaced by hardened anodized aluminum. This system uses a smaller head ring and 3D localizer than the conventional BRW head ring. Image quality of the standard head coil was not reported. They used the test phantom, constructed of plastic cylinders containing Lucite™ rods with tips at known BRW coordinates. The tips of the rods were identified in axial, sagittal, and

coronal planes. The calculated and measured coordinates were compared. The average errors were found to be less than 5 mm in any planes. They did not employ any specific calibration procedure to register MR images to CT images even though the slice thickness were 5 mm.

Peters et al. [Pet90] used the OBT stereotactic frame (manufactured from aluminum and Torlon™) for CT/MRI/DSA imaging procedures. MR fiducial markers contain 0.7 gram/l of $CuSO_4$. Five free faces of the frame are used to place fiducial markers to allow sagittal and coronal as well as transverse plane imaging. The MR imaging technique used is 325 mm FOV, 2 NEX (number of excitation) and SE pulse sequence with TR=250 msec and TE=30 msec. The OBT frame was tested in a 0.5 Tesla MR unit and no significant distortion was found. Also it was tested with 1.5 Tesla MR unit and found that paramagnetic effects associated with the aluminum components of the frame, which is close to some of the fiducial markers, can have significant effect on the position of these fiducial markers in the image. This introduced errors up to 3-4 mm in the trans-axial plane. They found that all components of the frame should be not only nonferrous but also nonmetallic, unless suitable nonparamagnetic alloys can be found. Also they found that the accuracy, in the transverse planes, of coordinate determination to be +/-1 mm. Their system appears to have artifacts due to the frame. The coordinate

determination algorithm does not correct for these artifacts nor does it correct for spatial distortion caused by the frame, the MR unit or patient-induced distortion. An accuracy of 3-4 mm error in trans-axial coordinates is not acceptable for radiosurgery applications.

Kondziolka et al. [Kon88] [Kon92] used the Leksell Model G stereotactic frame (Eleka Instrument, Tucker, GA) and a coordinate-determination system to obtain the CT and MR images. A MR-compatible stereotactic frame was constructed from a non-ferromagnetic aluminum alloy. Two MR units were used: 1.5 Tesla Signa™ MR scanner and 0.5 Tesla MAX™ scanner with T1, T2 and T1 gadolinium diethylene-triamine-pentaacetic acid-enhanced spin-echo image. MR images were obtained at 3 or 4 mm slice intervals with no intervals between slices and FOV of 250 mm. The imaging matrix is 256*192, yielding a pixel sizes of 1.95 mm in x-dimension and 2.6 mm in y-dimension. They investigated the correlation of CT and MR images in trans-axial, sagittal and coronal planes with 41 patients totalling 53 targets. Coordinates were measured in each plane and as vector distance between the target and the center of the stereotactic frame on axial or coronal MRI studies. They found that absolute axial plane MR and CT distances varied an average of 2.13+/-1.59 mm and the mean difference in the lateral axis was 1.19 mm and 1.5 mm in the AP axis. Central targets (defined less than 2 cm from the

center) have a mean MR/CT difference of 2.09 mm+/-1.79 mm and peripheral targets (greater than 2cm from the center) differed by 2.17+/-1.3 mm. They found also that MR field strength (0.5 vs 1.5 Tesla) did not relate to coordinate determination accuracy. Computer dose planning was usually based upon the MR scan to guide the treatment of pituitary microadenomas, small macroadenomas and pineal or brain stem lesions. Also they discussed the possible sources of the MR/CT differences: (1) inhomogeneous shimming of the MR scanner, (2) mechanical motion, (3) eddy current effects when noncylindrical or nonspherical structures are imaged, (4) susceptibility artifacts between air/tissue and air/water interface, (5) internal or external ferromagnetic objects and (6) inhomogeneity in the magnetic field caused by a patient and the nonlinear magnetic field gradients.

Several facts should be noted from Kondziolka's presentation [Kon88] [Kon92]. (1) chemical shift artifacts are important at fat/water interfaces but less important in intracranial imaging. (2) The lack of air/water and air/tissue interfaces in the brain should limit the occurrence of susceptibility artifacts that depend on the imaging sequence. (3) The most common artifact is caused by patient movement. The frame and the head coil should be rigidly attached to the MR scanner. (4) A difference of approximately 2 mm was identified between CT and MR images. This 2 mm error was

obtained by measuring target position in CT and MR images. However, it does not have any significance because the target shape is generally different in CT and MRI. Also the registration procedure should be employed to correct the nonlinear gradient magnetic fields and should be tested with a 3D phantom to verify the registration algorithm. (5) Field strength did not correlate with the coordinate determination. However, the coordinate determination has nothing to do with main magnetic fields, but is related to nonlinearity of the gradient magnetic fields. From their error analysis, the localization error is on the order of one pixel in-plane on the order of 2 mm.

Pelizzari et al. [Pel89] used the surface matching technique to correlate CT and MR images. They describe a method of image correlation in three dimensions based upon contours of each image set. This techniques does not use any stereotactic head frame, but needs user intervention to guide the matching process. This matching technique called head-hat matching is an excellent way to correlate two imaging modalities without any special frames. The head-hat matching algorithm needs user intervention in order to guide the matching procedure. The reported matching accuracy between CT and MR images are 1.36 mm +/- 0.45 mm for rms mismatch.

Literature Survey for Digital Angiography

Conventional biplane angiography has been used at the University of Florida to scan AVM patients. The angio procedure was explained in detail in chapter 2. Also in the previous section the various technical advantages of using digital radiography in the radiosurgery application are mentioned. The direct use of the digital angiography is not possible mainly because of spatial distortion, causing the misregistration of fiducial markers as well as target volumes. In some institutions, distorted digital angiograms have been used if the distortion is acceptable, for example, within a few mm. This procedure is performed by limiting the regions of the digital images using smaller magnification factors or by using data correlation with CT or MR images. This approach was not considered acceptable at UF. Therefore, the correction (or unwarping) algorithm was developed to improve the accuracy of digital radiography. In this section, the correction algorithm called "geometric transformation" and the source of spatial distortion in the digital radiography will be reviewed.

General Geometric Transformation

Historically, geometric transformations were first performed on continuous (analog) images using optical systems.

Early work in this area is described by Cutrona et al. [Cut60], a landmark paper on the use of optics to perform geometric transformations. Since then, numerous advances have been made in this field [Hor87] [Oha72]. Digital computer system have offered the flexibility to manipulate the geometric transformation digitally. The earliest work in the geometric transformation for digital images stems from remote sensing fields. This area gained attention in the mid-1960s, when the US National Aeronautics and Space Administration (NASA) embarked on an earth observation program. The objective was the acquisition of data for environmental research applicable to earth resource inventory and management. The project involved multi-image sets using different sensors at different times. The task was to align each image with every other image so that all corresponding points match. This process is known as image registration. Geometric transformation was originally introduced to correct distortion and to allow for the accurate determinations of spatial relationships and scale. This requires estimation of the distortion model, usually by means of reference points which may be accurately marked or readily identified. Detailed reviews are presented by Gonzales and Pratt [Gon 87] [Pra78]. In the vast majority of cases, the geometric transformation are modeled as a bivariate polynomial whose coefficients are obtained by minimizing an error function over the reference points. Usually, second-order polynomials are

used to account for translation, rotation, skew and pincushion distortion [Wol93]. For more local controls, affine transformation and piecewise polynomial mapping are widely used. See reviews for early work of the remote sensing [Har76].

Source of Distortions in Digital Radiography

As mentioned, the DSA consist of three major pieces of equipments: (1) x-ray generator and tube, (2) Image Intensifier and (3) camera and television (TV) imaging chain [Cur90]. The different physical characteristics of each equipment and its effects upon the image are different from each other. Each part will be described in detail.

(1) X-ray Generator and Tube

The parameters that affect image quality are described: focal spot size, acceleration voltage, and the energy distribution of the x-ray. The most common type of x-ray tube is the rotating anode configuration. The anode rotates at 180 revolution per second. For DSA purpose, the electron acceleration tube potential used is usually 50 to 100 KVp. The physical size of the anode is 1mm*6mm, but the effective focal spot size is 1 mm*1 mm. This finite size of the focal spot places resolution limitations on the final images.

For digital radiography it is crtical that the x-ray generator provides repeatable exposures. A small difference in the x-ray tube current or applied potential will result in an improper mask subtraction of the unchanged areas of the head, thus obscuring the visualization of the actual structures of interest.

(2) Image Intensifier

An x-ray image intensifier (II) is a device that converts an incident x-ray pattern, yielding a visible-light image of brightness substantially higher than that of a simple phosphor screen. The II is a large vacuum bottle containing a complex arrangement of an x-ray absorbing, light emitting phosphor, and specially shaped photocathode (curved structures to keep electron paths constant during focusing procedure and to maintain mechanical strength of the image intensifier) and electrodes for electronically focusing the electron beam. Therefore the image quality at the output of II depends upon the electron lens system.

The electron lens is governed by many of the same principles that govern the classical optical elements. To a first approximation, there are five primary aberrations. The first three: spherical aberration, coma and astigmatism directly affect partial resolution by causing the blurred

focusing. The final two aberrations are the distortion of the image by displacement and stretching.

Each aberration is applicable to II. For the II user, it is very difficult to measure the first three aberrations. In this research, the last two aberrations are examined to correct the spatial distortion.

(3) TV Imaging Chains

The formation of video images begins with the television pickup tube, a device that converts light into electrical charges. The signal current readout is very small, on the order of 1uA. This small current is passed through a large resistor and generates voltage. This signal is a 1D waveform that effectively codes a 2D image focused onto the pickup tube. Most DSA systems operate at the data rate of 512 or 1024 lines per frame and one frame on the order of 30msec. The TV camera systems have a SNR of 60dB or higher.

One important parameter of the TV camera is temporal response called "lag". The lag is a measure of the speed with which the TV camera can respond to rapid changes in the brightness. This lag can be classified into two different types of lag: buildup lag and decay lag. This phenomenon can cause deterioration of image quality in the digital

radiography requiring high temporal resolution. This should be considered with temporal filtering.

Literature Survey of Correction Procedure

Casperson et al. [Cas76] developed quantitative measurements of the spatial distortion and intensity variation of the image intensifer. This work made possible a quantitative comparison of image intensifiers with respect to distortions, such as pincushion or barrel distortion. They ignored local distortion like coma, astigmatism, aberration, which could not be represented by a global function. A 2D third order mapping function with a single parameter is used to analyze the performance of the image intensifier. Therefore, the correction function should take care of the locally occurring distortions. Conceptually, the global function can be used to correct gray level shading with a single parameter.

O'handley et al. [Oha72] described the correction procedure for removing camera-induced-system geometric distortion from the images obtained utilizing a vidicon camera installed in the Mariner 9 space probe. The "first-order" correction of the vidicon images are described. Small metallic squares are deposited on the active surface of the vidicon camera and appear as black spots within each sampled

image. Conceptually, the method used here could be directly applied to the application of the correction procedure of spatial distortion in digital angiography.

Charraboty at el. [Cha79] described a method to determine and correct the spatial distortion affecting images acquired with the image intensifier and video system. The distortion is separated into two physically distinct components: (1) a predominant one originating from the projection of the x-ray image into the curved input phosphor and (2) digitization procedure. A method is presented for determining the two components from calibration images of a grid phantom, which consists of orthogonal sets of straight lines: 0.76mm wide and 2.0mm deep, cut at 12.7mm intervals on blocks of aluminum (23cm*23cm*0.63cm). The distortion is modeled as a linear transformation and coefficients are experimentally derived. This approach corrects for global distortion without considering local distortion. For example, distortion resulting from nonuniform sensitivity of the tube are not corrected. The parameters should be known to apply the correction algorithm if the parameters are reproducible. Unfortunately, the accuracy of this approach has not been investigated.

Henri et al. [Hen90] described the incorporation of DSA in the stereotactic radiosurgery on Angiotron/Digitron™

(Siemens Medical System, Erlangen, Germany). Images are acquired with a 512*512*10-bit matrix using a 270 mm FOV for lateral view and 170 mm for AP views. Object magnification is restricted in order to maintain the fiducial markers within this limit. In order to quantify the pincushion distortion, a 1cm copper wire grid embedded in Plexiglass™ is attached to the surface of the image intensifier and images are taken at various orientations using each available FOV. The distortion is less than 0.5mm for all cases. They used the first-order linear approximation to correct the pincushion distortion. More fiducial markers were added to minimize uncertainty of determining the fiducial markers in the digital images. They did not implement an automatic method of identifying the fiducial markers. They did not test the accuracy of the unwarping algorithm with a phantom. The necessity of verifying the unwarping algorithm is a must.

Fujita et al. [Fuj87] used distortion procedures to remove pincushion distortion in chest radiography with a 57 cm image intensifier system. The wire mesh is placed on the image intensifier. They used the assumption that the spatial distortion is radially symmetric about the center of the image intensifier. The fifth order polynomial fitting function with bilinear interpolation is used to map from distorted to undistorted image. However, the accuracy of the fifth-order fitting function was not evaluated. As with the previous

approach, the global fitting function, which does not correct for local distortion, does not provide the required accuracy for the radiosurgery application (for example, less than 1mm).

Peters et al. [Pet 87] [Pet90] uses the OBT frame for a DSA imaging procedure. The fiducial markers consist of small steel pellets embedded in a Plexiglass™ plate at the corners of a square. Plates on each side of the frame and in front and back, yield eight points in each of the AP and lateral views. They rely on the iterative procedure by switching between the AP and the lateral images to estimate the three dimensional coordinates of the target depth. They estimate that +/-1 mm errors can be obtained by using 15 cm FOV and 24 cm image intensifier. While this error might be acceptable, the iterative procedure is time consuming and user-dependent.

Rudin et al. [Rud91] used two parameter fitting functions based upon the third-order circular coordinates compared with a single parameter fitting function of the Casperson approach mentioned earlier [Cas76]. The accuracy of this fit is far better than one parameter characterization of distortion. The standard error of the two parameter fit was less than 0.1mm or 0.03 percent. This approach is very accurate. Also several parameters of the fitting functions should be measured in applying this global fitting function. The accuracy of these parameters determine the accuracy of the correction functions.

If these parameters are measured accurately and reproducibly, this could be an excellent method to correct the spatial distortion.

Boone et al. [Boo91] intensively reviewed analysis and correction in the image intensifier and TV chains, including linear gray scale mapping, dc offset, veiling glare, pincushion distortion and shading correction. Shading can be removed by simply using the division operation. The deconvolution is used to remove the veiling glare. The pincushion distortion is handled by applying affine transformation on one of the sets of fiducial markers (three fiducial markers for each affine transformation) on the 2 cm rectilinear grid. The accuracy of this mapping function is not reported. Conceptually, the proposed method is worthy of a try in the radiosurgery application.

Reimann et al. [Rei93] developed an automated procedure to accurately correct the distortion present in x-ray image intensifiers. An image of a rectilinear grid of tin wire (250 um in diameter and 1 cm increments between grid) with 22 cm-diameter image intensifier is acquired. The wire cross points are obtained without user intervention. The points are associated with their true points by using the piecewise affine transformation [Wol93] [Pra78]. Each output pixel point is mapped to the distorted image by using the bilinear

interpolation [Wol93] to estimate the gray level at that point. After the calibration image is analyzed, all subsequent images are corrected using the table lookup algorithm. According to their conclusion, computation time to acquire the wire crossing points was long (about 83 minutes) and it took about 4 seconds to correct other images with the previously determined parameters. They did not use any phantom test to verify the accuracy of the correction algorithm, even though they mentioned that a near optimal fitting algorithm can be determined. For the application of radiosurgery, this lack of a verifying procedure is very weak point. One important point from their presentation, the pieceswise first order linear interpolation, like affine transformation, are good for the correction of the distortions caused by local magnetic fields or optical camera aberration.

CHAPTER 4
MR-COMPATIBLE BRW RING

Introduction

The use of CT scanning for stereotactic neurosurgical planning has extended to include MR imaging in many institutions [Sch92] [Yan89] [Hei87] [Kon92] [Pet90]. With this the University of Florida (UF) has fabricated a MR-compatible BRW head ring (MR ring) and its fixtures so MR images can be used directly with the current UF stereotactic radiosurgery system without major modifications in hardware and software. As mentioned in chapter 3, there are three components for CT scanning: (1) BRW head ring and its fixtures, (2) localizer and (3) CT bracket. The fixtures include the localization pins (4 pins), the supporters, 4 locks and four screws. Each component with MR water phantom is shown in Fig. 4.1. The localization pins are fixed onto the patient's skull under local anesthesia. The supports hold the localization pins and are attached onto the BRW head ring through the four screws, which are adjusted to set up the patient's skull for CT scanning.

The MR-compatible BRW head ring and the MR localizer were

constructed by Radionics. The anodized aluminum alloy (AL7075: 99 percent aluminum) is used to fabricate the MR ring, locks and screws. The MR ring is split into two pieces and is re-connected with screws. The MR localizer is constructed of Plexiglass™ and it contains nine plastic rods in which contrast material (propanediol) is used [Pri90]. The MR localizer is geometrically the same as the CT localizer and the MR scanning procedure is the same as the trans-axial scanning in the CT imaging currently used at the University of Florida. Therefore, all the software for registration procedure can be directly used processing MR images in the same way as CT images.

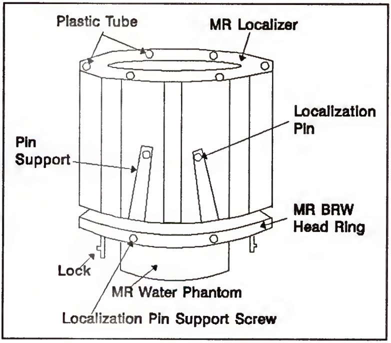

Fig. 4.1 Phantom Setup with MR BRW Ring, MR Localizer and MR Water Phantom. This setup is used to investigate spatial distortion from the MR-compatible BRW head ring and the localization pins.

In order to examine the image quality obtained using the MR ring, one water phantom was fabricated to simulate a human brain. The images are tested by using the MR ring and the MR localizer with two MR Units (1.5 Tesla GE Signa™ scanner and 1.0 Tesla Siemens Magnetom™ SP4000 scanner) utilizing standard head scanning techniques (see next section for detailed scanning parameters).

MR Water Phantom Fabrication

In order to test the initial MR-compatible device, the water phantom with dimensions of 14cm inside diameter and 17cm height and 1cm wall was fabricated from a Plexiglass™ to simulate the human head. Tap water with 0.25 percent saline is used to electrically mimic the human head. Also, a square structure was included in the water phantom in order to measure the spatial distortion due to the gradient magnetic fields as well as the inhomogeneity distortion. The square structure in the water phantom consists of two Plexiglass™ end plates with small hollow plastic tubes running from end to end. Fig. 4.2 shows the MR water phantom with the square structure and a cross section view of the square structure of the MR water phantom.

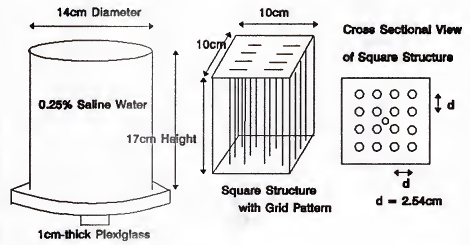

Figure 4.2 Structures of MR Water Phantom. The square meshy structure is placed in the water phantom to examine the inhomogeneity distortion and nonlinearity of gradient magnetic fields of the MR scanner. Square structures are used to investigate CT/MR correlation within the middle portion of the water phantom.

MR Imaging Technique and MR Unit

Two MR scanners have been used to qualitatively analyze the artifacts due to the materials which make up the BRW head ring and its fixtures. The testing is done on the Magnetom™ SP4000 Scanner (1.0 Tesla) and the Signa™ Scanner (1.5 Tesla) with the scanning techniques in Table 4.1.

Table 4.1 MR Scanning Parameters of T2-Weighted Imaging

No	Imaging Parameter	Used Values
1	Pulse Sequence	Spin Echo (SE) sequence
2	TR	500msec
3	TE	20msec
4	Slice Thickness	Body Coil: 5mm Custom-made Coil: 3mm
5	Slice Gap	0mm
6	Acquisition	2 NEX
7	Excitation Pattern	Interleaved
8	Flip Angle	90 degrees
9	Field-of-View (FOV)	345mm (Rectangular FOV)
10	Matrix Size	512*512, over-sampling

Phantom Setup for MR Scanning

In order to avoid motion artifacts during MR imaging procedure, the MR ring is attached to a Plexiglass™ support, which is fixed to the MR scanner. The MR localizer is locked onto the MR ring by three locks (see Fig. 4.1). The Plexiglass™ supporter is shown in Fig. 4.3.

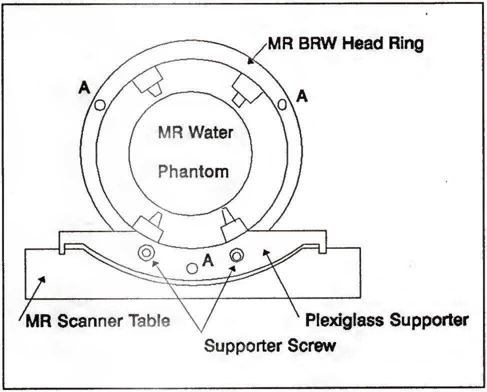

Fig. 4.3 Plexiglass™ Supporter attached on the MR Scanner and the MR BRW Head Ring. "A" represents one of three locks which is used to fix the MR localizer onto the MR ring. The locks are made of aluminum alloy (AL7075). The supporter is used to fix the MR-compatible BRW head ring onto the scanning table.

MR Images with Initial MR-compatible BRW Head Ring

The MR-compatible BRW head ring with its fixtures were attached to the water phantom (see Fig. 4.1 for phantom setup) and scanned with either Siemens Magnetom™ or GE Signa™ MR scanner. Images were revived on film. The MR images are shown in Fig. 4.4. The images are severely distorted by several fixtures, which are not ferromagnetic

materials. Small permanent magnet was used before scanning to test for ferromagnetic materials. However, there is no direct way to investigate the coupling between the fixtures and dynamically changing RF magnetic fields or gradient magnetic fields [You89]. The MR images demonstrate the importance of fixtures tested experimentally by scanning with either MR unit.

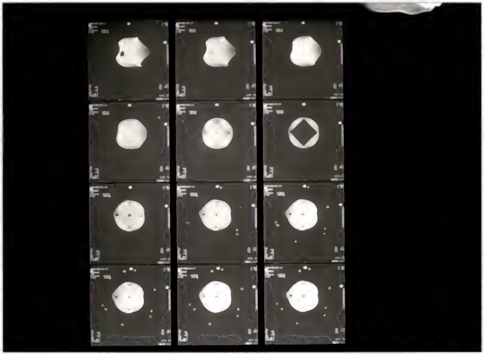

Fig. 4.4 MR Film Images Obtained with Initial MR Ring

BRW Head Ring and Its Fixtures

The aluminum alloy (AL7075) was selected for MR ring fabrication and its fixtures (locks, Plexiglass™ supporter screws, pin supporter screw), because it did not introduce noticeable artifacts or spatial distortion in the area of interest: (1) inside the MR water phantom (region 1) and (2) peripheral region (region 2), where the nine localization rods are located. These two major regions are shown in Fig. 4.5.

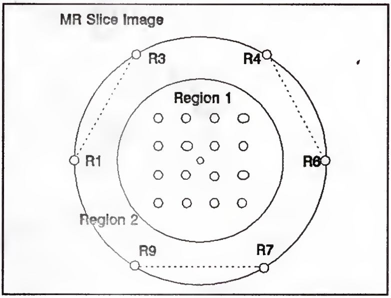

Figure 4.5 Two Regions for Artifacts Investigation
In the picture, slanting rods move along the dotted lines depending upon the axial coordinates of slice image. Region 1 (within the water phantom) is used for measuring inhomogeneity distortion and Region 2 (occupied by the rods of the MR localizer) is used for measuring nonlinearity of the gradient magnetic fields.

With this in mind, the MR images with new MR ring and its fixtures are scanned with the Siemens Magnetom™ SP4000. Each slice of the phantom image (with the setup configuration in Fig. 4.3) are hard copied to film and shown in the Fig. 4.6.

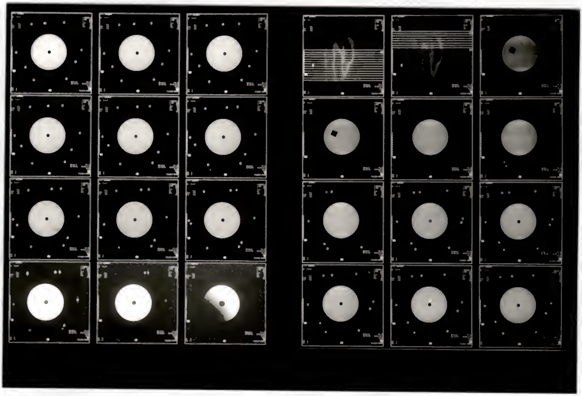

Figure 4.6 Film Images with Final MR BRW Head Ring
Two sets of MR images are shown to investigate the artifacts resulting from the MR BRW head ring and its fixtures. 10 slices in the left figure covers 4cm volume of the MR water phantom below and above the MR BRW head ring. The localization rods in the last three slices are not displayed. There is no noticeable artifacts from the ring. Siemens Magnetom™ scanner are used with the imaging technique in Table 4.1.

Two sets of MR images are printed to full size film (14" * 17" film). The artifacts or spatial distortion are analyzed on those images in the two regions. First, the region 1 was examined to investigate the spatial distortion. The radial distance of each hollow plastic tube (see Fig. 4.2) is measured. The spatial distortion in the MR water phantom is much less than one pixel (0.67 mm). Second, the radial distance from the center coordinates are measured for each straight rod. Also the radial distance is less than one pixel. The slanting rods are used to investigate the nonlinearity of the gradient magnetic fields by measuring the deviation from the line formed by the neighboring straight rods. The deviation was also found to be less than one pixel. This analysis is performed manually using a ruler. The MR slice images used for distortion analysis are shown in the Figure 4.7.

Fixation Pin Fabrication

Non-paramagnetic stainless steel was initially used to fabricate the fixation pins. They were used to treat the first patient with MRI. The film image is shown in Figure 4.8. The film shows the pin artifacts in four places around the skull. The 1cm-diameter regions are heavily distorted by the pins. Another artifacts in the film were introduced by a surgical clip, which was implanted in the patient head. Thus, new material should be found for the localization pins.

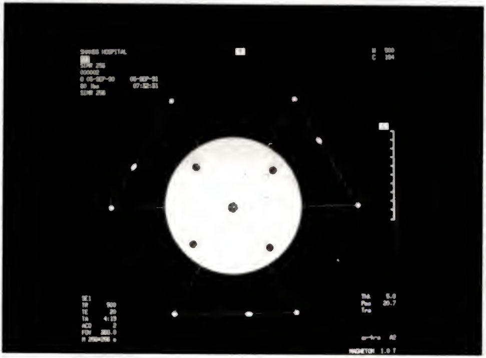

Figure 4.7. MR Film Images examined with Distortion Analysis

All straight rods are examined by drawing the circle on the film and measure the deviation of each rod from the circle. The deviation of a slanting rods are examined from the line formed by two neighbor straight rods.

Several materials for pin fabrication were investigated: aluminum alloy, industrial titanium, bio-compatible titanium, CoCr, and non-ferromagnetic stainless steel [Wen88] [Hin88] [Lov87]. Distortions caused by these materials were reviewed by using the film images and manually measuring the range of the distortion. This method is effective when the distortion occurs within the water

phantom. Three experimental setups were used to investigate the pin artifacts.

First, the various pins were taped on the outside of the MR water phantom. Most non-ferromagnetic materials do not introduce noticeable artifacts in the water phantom because the 1 cm thick Plexiglass™ provides some space

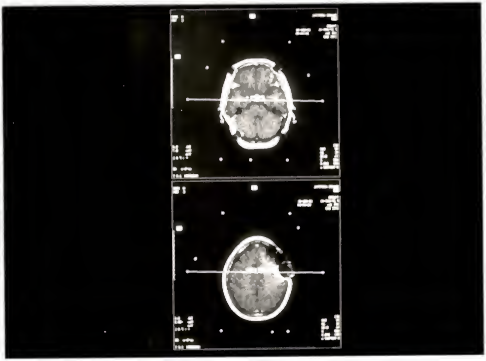

Fig. 4.8 Pin Artifacts
The upper figure demonstrate the artifacts resulting from the localization pins (made of nonferromagnetic tungsten). The line connecting rod 1 and rod 6 are measured to examine the nonlinearity of the MR scanner. The measured value is 279.3 mm (mechanical distance between two rods is 280 mm).

ranging from the water molecules to the metals. Fig. 4.6 shows that there are no noticeable pin artifacts over all MR images. Second, those pins are inserted into a bolus (gel material and tissue equivalent material used in radiation therapy treatment), which is also taped around the MR water phantom. Except for a few materials all materials (aluminum, CoCr, engineering titanium and and bio-compatible titanium) introduce some noticeable artifacts [Win88] [Hin88]. The experimental setup is shown in Fig. 4.9. Third, a few materials taped on polystyrene are put inside the water phantom. The bio-compatible titanium (Ti-6Al-4V) localization pins introduce minimum artifacts around the sharp tip (2 mm regions of the tip show arrow-shaped artifacts). However, this distortion does not introduce any artifacts in the clinical situation because the tip of the fixation pins is put into the bone and this bone extends the space between the localization pins and the brain.

Clinical Application with MR-compatible BRW Ring

A Plexiglass™ support was used to immobilize a patient's head during 16-minute scanning procedure. The MR scanner has a series of grooves along the two edges of the scanning table. The Plexiglass™ support has two tabs in both ends, which fit in the grooves, thus preventing motion artifacts (see Fig. 4.3). Motion artifacts have not been noticeable. The support is also used to set the image spin

angles (see Fig. 2.3) of the MR images by orienting the x and y axis of the MR localizer to the AP and the lateral axis of BRW coordinate system so that the rotation process is not necessary, thus reducing the image registration procedure.

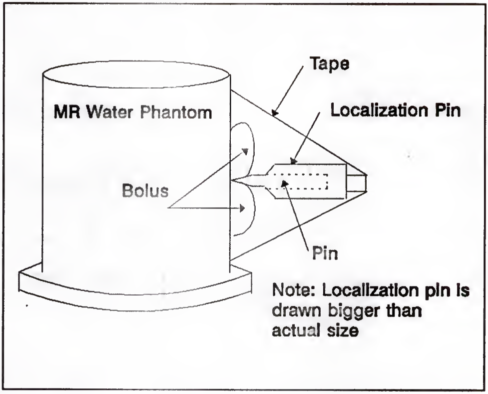

Figure 4.9 Experimental Setup for Localization Pin. The bolus is used to simulate the human skin in order to investigate the interaction between the pins and the tissue when RF is applied.

Problems with Body Coil and Comments

This BRW head ring and its fixtures (aluminum alloy AL7075 for the ring and its fixtures and biocompatible titanium for the localization pins) were used to treat six patients with acoustics, meningioma and pituitary glioma. The targets (or tumors) were defined on the trans-axial plane (pixel size is 0.67 mm in the trans-axial plane and 3 mm in the saggital and the coronal views), but it was very difficult to define the target on the computer reconstructed sagittal and coronal planes because of the low SNR.

The MR images of a patient with acoustic schwannoma are shown in the Figure 4.10. Note the poor definition of the tumor in coronal planes. These MR images were used to localize the tumor according to the CT localization procedure. The University of Florida radiosurgery system computer uses linear interpolation to reconstruct two orthogonal planes: coronal and sagittal planes. 5 mm slice thickness does not provide sufficient resolution with radiosurgery which needs high level of accuracy (compared with 1 mm slice thickness with CT images for the tumor plane). In order to decrease the slice thickness to 3 mm (the minimum slice thickness with the Magnetom™ scanner) and improve the SNR, the custom-made head coil is necessary [Sie89] [Syk91].

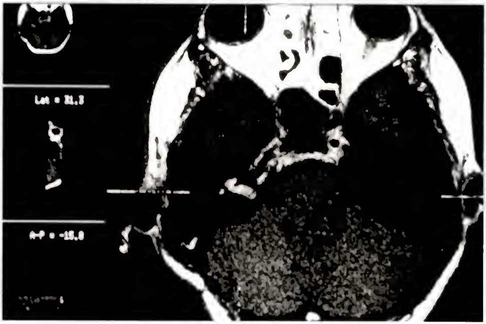

Fig. 4.10 MR Images of Acoustics Patient on Three Planes
The acoustic schwannoma of the left ear canal is shown in the right canvas (512 * 512). The right image is magnified using linear interpolation. The left three canvases (64 * 64) represents three imaging planes, which are reconstructed from the images on the trans-axial plane.

CHAPTER 5
CUSTOM-MADE HEAD COIL RESONATOR

Introduction to Birdcage Resonator

The body coil has been used to treat six patients streotactically at the University of Florida. The major problem of using the body coil was that the signal-to-noise ratio (SNR) was too low to define the small tumor volume in the reconstructed sagittal or coronal planes of MR images. The slice thickness (see Table 4.1) was set to 5mm in order to maintain reasonable SNR. In order to improve the SNR or decrease the slice thickness (see Appendix B for the formula about SNR), the fabrication of a custom-made head coil resonator was considered. In this chapter, the detailed procedure for the head coil fabrication is described. The image analysis obtained using the head coil will be described in chapter 6.

There are, in general application, three different types of head coil configurations: (1) surface (2) saddle and (3) birdcage [Cal91] [Mor86] [Hay85]. The saddle type head coil was very frequently used in the general application of head or knee coils [Tho86] [Cal91] [Mor90] and in the few institutions

which have developed radiosurgery systems. The saddle coil and the surface coil do not provide greater uniformity over large volume of imaging [Cal91] [Mor87] [Sco88]. Recently, there are many publications detailing the implementation of birdcage type coils. These coils gives more radio frequency (RF) uniformity and higher signal-to-noise ratio (SNR) than surface and saddle coil design [Tro89] [Hay85] [Har91] [Har90] [Pas91]. The uniformity of the birdcage head coil can obtain better than 95 percent over at least 80 percent of its diameter in the imaging plane [Vul92]. Another advantage of the birdcage head coil is that the coil's symmetrical structure allows quadrature drive and reception which decreases RF power requirements by a factor of two, thus reduces the RF power deposited on the sample and increases the SNR by approximately 40 percent [Hay85]. The symmetrical structures of the birdcage head coil also reduce the artifacts caused by an uneven penetration of the RF fields in the conductive sample [Sot88]. The linear type birdcage head coil resonator is chosen from previous discussion and its design concept is described in this chapter.

Design Concept

While several studies of the birdcage resonator have appeared in recent literatures, they have primarily focused on either lowpass [Har81] or highpass versions [Wat88] [Har90].

The basic structure of a birdcage resonator consists of two end rings connected by N (generally 4 to 16) parallel segments (called "rung" in Figure 5.1) at angles with capacitors inserted either in the legs or in the rings for lowpass or highpass coils (see Figure 5.1). The lowpass version of the birdcage resonator was chosen for our application, although the highpass version also works well. The formulation for the lowpass configuration is obtained by using lumped circuit analysis [Hay85] [Wat88] [Tro89]. Therefore, the lowpass configuration was selected to implement the linear type head coil resonator for radiosurgery.

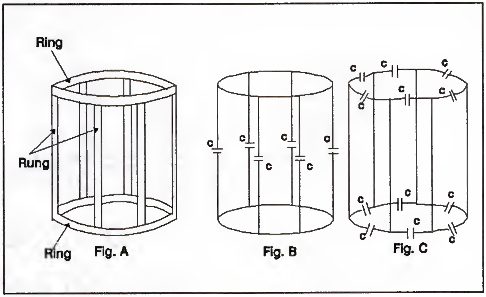

Fig. 5.1. Diagram of six-rung birdcage resonator (Fig. A), lowpass type (Fig. B) and highpass type (Fig. C). In Fig. B and Fig. C, the c represents a capacitor.

Structures of the Lowpass Version

In the following sections, the detailed information of the lowpass version of the birdcage resonator is described. It consists of two circular rings connected by N equally spaced straight segments (called rungs), each of which includes a capacitance. The two wires of the capacitor act as inductors in high frequency regions. Therefore, the capacitor wires are replaced by copper strips (see Fig. 5.2), which can be easily modelled and represented by L_2 Fig. 5.3. The birdcage resonator can be analyzed by using the lumped element balanced delay line, which is shown in the Fig. 5.3 [Hay85]. All inductors L_2 are coupled to each other by mutual inductance and all inductors L_1 are also inductively coupled. The effects due to the mutual inductance has been analyzed by Tropp [Tro89].

Structure of Former

The electronic circuits of the birdcage resonator are implemented on the thin mylar sheet. It is necessary to rigidly attach the mylar sheet on the mechanical structure called "MR former". A patient should be able to be comfortably placed into the MR former. The MR former

configuration is shown in Fig. 5.4. There are several requirements for the former fabrication. First, the MR former composition should minimize any artifacts due to the materials. A 1cm-thick Lucite™ cylinder is used to make the MR former. The MR former consists of the former cylinder and the supporter structure. The cylinder is cut into two halves: lower and upper pieces. The lower pieces are rigidly attached to the MR support structure. The upper portion is attached with lucite hinges to the lower.

The MR former should also include locks to fix the MR localizer onto the former during MR scanning. The MR localizer is fixed to the former through the localizer lock screw (see Fig. 5.4.B). A pair of nylon screws are used to attach the MR localizer. They are preadjusted to eliminate the need for spin angle compensation. The cylindrical axis of the MR former is aligned to the z-axis of the MR scanner by using a non-magnetic spirit water level.

The mechanical dimensions are set to 35cm inside diameter and 30cm length. The birdcage should be designed using these mechanical specification.

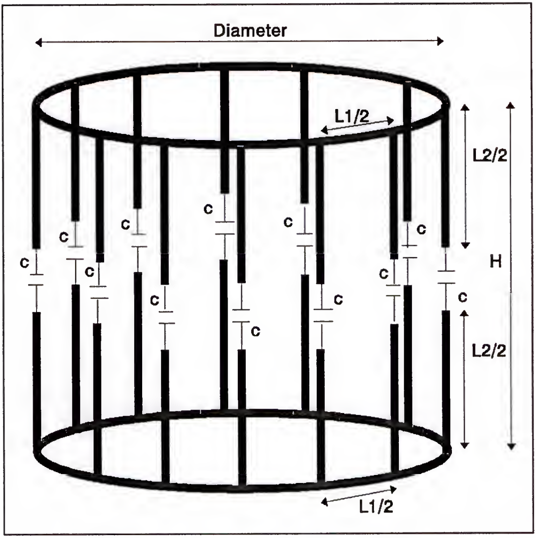

Figure 5.2 Lowpass Configuration of the Birdcage Resonator. H represents the height of the resonator (22cm). Diameter is about 35cm. The height and the diameter are shown in Fig. 5.9. L_2 represents the inductor of the rung between two end rings and it splits into two terms because the capacitor is placed between the two end rings. The thick lines represent 1cm-wide copper strips to make inductors. The copper strips and various capacitors are taped on the mylar sheet, which is placed onto the MR former. The MR former is the Lucite™ supporter. Refer to Fig. 5.3 for lumped circuit diagram for this structure.

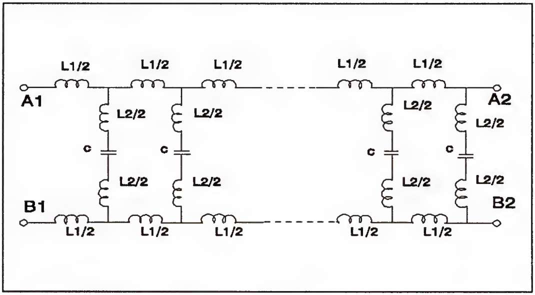

Figure 5.3 Lumped Element Equivalent of Twelve-Rung Lowpass Birdcage Resonator Configuration. Point A1 and B1 connect to point A2 and B2, respectively. L_1 is the inductance between two rungs and the L_2 is the inductance between two end rings.

Number of Rungs in the Birdcage Coil

The number of the rungs determines the uniformity of the RF magnetic field distribution. Normally, symmetric birdcage head coils consists of eight or more rungs and will resonate in N/2 frequencies [Vul90]. The symmetrical condition means that (1) each rung is identical and (2) uniform loading effects are due to a sample (a patient or MR water phantom).

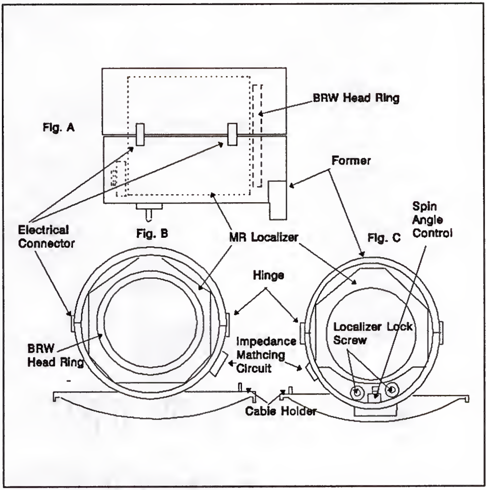

Figure 5.4 The MR Former Configuration.
Fig. A is the side view of the MR former, Fig. B is the bottom view and Fig. C is the top view. In Fig. A, the electrical connector, made of copper, is used to connect two circular end rings. In Fig. C, the MR localizer is screwed to the MR former by using the localizer lock screw. The MR former is immobilized onto the MR scanner table. The impedance matching network is installed on a printed circuit board and attached to one end of the birdcage ring.

Generally speaking, the more rungs, the more uniform is the RF magnetic field. The limiting factor to the number of rungs is (1) the width of the copper strips, (2) the interference between the birdcage coil and the gradient magnetic fields, (3) the geometric relationship between the rungs and the rod positions of the MR localizers and (4) mutual inductance (dominant and difficult to estimate the magnetic field when more rungs are added with the fixed diameter of the MR former). The magnetic field at the region close to each rung is not uniform because the strength of the magnetic field is inversely proportional to the distance.

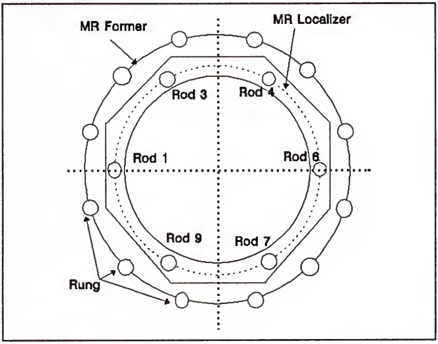

Figure 5.5 Geometric relationship between the rods of the MR localizer and the rungs of the birdcage resonator.

The minimum number of rungs to satisfy the symmetry condition is 12. The symmetry condition is satisfied by placing each rod of the MR localizer between two rungs of the birdcage resonator. To quantitatively analyze the uniformity of the RF magnetic field, the Bio-Savart theorem (see Appendix A) is applied with assumptions that (1) all rungs are infinitely long, (2) loading effects from a head are ignored, (3) the impedance matching network does not disturb symmetrical structures and (4) surface current, running along each rung, is proportional to $\sin(A_i)$, where the A_i is the cylindrical coordinate azimuthal angle.

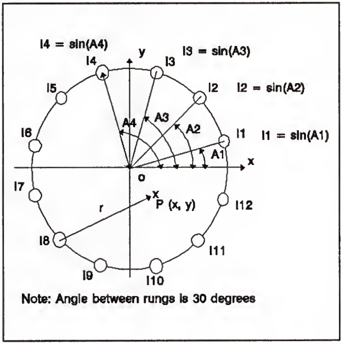

$$dB\big|_{at\ P(x,y)} = \frac{\mu_o}{4\pi}\cdot I_i\cdot\frac{dl\times r}{|r|^3}$$

Eq. 5.1.

Figure 5.6. Application of Bio-Savart equation to get the magnetic field at the point P. The I_i is the current of each rung and A_i is the geometrical angle between x coordinate and the rung i. The dl is assumed to be coming out of the paper.

The magnetic field is obtained at all points in the plane with 512*512 matrix and normalized by the magnetic field at the center point. The computer simulation is shown in Figure 5.7. The regions at the rods of the MR localizer are covered by less than +/- 10 percent. The region within 1cm from each rung is not used to calculate the magnetic field because the copper strips are 1cm wide.

Determination of Birdcage Length

Once the rung number is determined, the length of the birdcage resonator should be determined by considering the mechanical limitation of the MR former. From the electrical point of view, two factors should be considered: (1) uniformity and (2) SNR. The longer the rung, the more uniform is the magnetic field in the volume of interest which is 32cm diameter and 16cm height. The cause of the nonuniformity of the RF magnetic field is the roll-off characteristics at the ends of the coil while the short coil picks up less noise from portions of the head [Hay85]. Theses two factors should be compromised. The uniformity constraint can be easily considered to determine the length of the birdcage resonator. The Bio-Savart equation is applied to estimate the magnetic field at the cylindrical axis. The criterion to get the length of the birdcage resonator is that the magnetic field at the edge of the MR

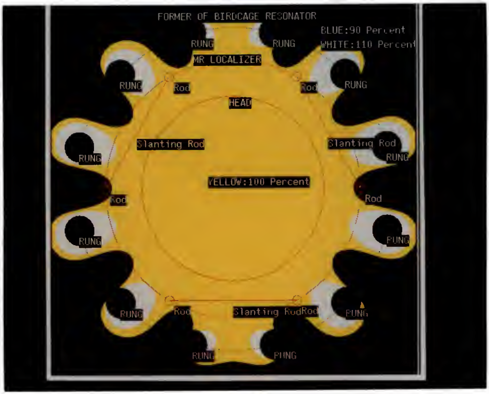

Figure 5.7 Computer simulation of inplane magnetic field when all the rungs are assumed to be infinitely long. The region represented by yellow color is covered by 95 to 105 percent of the magnetic field normalized at the center of the birdcage resonator. Each rung of the birdcage resonator is represented by a green circle. The straight rod of the MR localizer is represented by a red circle. The average size of the head is represented by a red circle in the middle of the diagram.

localizer (8 cm from the center) is covered by 80 percent (see Fig. 5.8). The length of the birdcage resonator is set to 22 cm. The birdcage is about 3 cm longer on both ends than the MR localizer when the MR localizer is placed at the center of the birdcage resonator. In general, 80 percent is very frequently used to describe the inplane uniformity [Dix88] [Vul92]. According to the computer simulation in Fig. 5.8, the magnetic field at the edge of the MR localizer (8cm from the center in Fig.5.8) is about 82 percent with respect to that at the central point of the birdcage resonator.

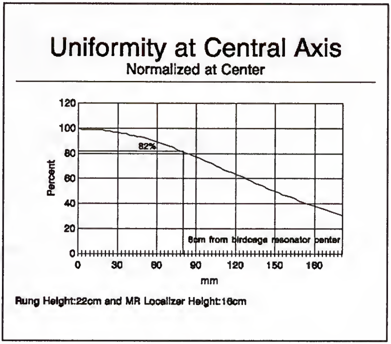

Figure 5.8 Computer simulation at the cylindrical axis of the birdcage resonator. The uniformity is normalized by the magnetic field at the center.

Electrical Characteristics of the Birdcage Coil

Once the length of the birdcage resonator and the number of the rungs are determined, the mode should be determined to calculate the values of capacitors in the rungs, so that the resonant frequency of the birdcage is precisely set to the operating frequency of the MR scanner (41.04MHz), which is the Siemens Magnetom^{SP} SP4000 MR scanner.

The mode represents the resonant frequencies of the birdcage resonator. The number of the resonant frequencies is half of the rung number (6 when the number of rungs are 12). The higher mode resonant frequency produces increasingly less uniform fields [Hay85]. Therefore, the principle mode (M = 1 in Eq. 5.2) is chosen. The lumped element equivalent circuit of a lowpass birdcage coil was shown in the Fig. 5.3. This model was used to calculate the values of the capacitors in the rung. This network has N/2 resonant frequencies in the following equation:

$$w = \frac{2 * \sin(\Pi * M/N)}{\sqrt{L_1 * C + 4 * L_2 * \sin^2(\Pi * M/N)}} \qquad \text{Eq. 5.2}$$

where w = angular frequency (2*π*frequency)

L_1 = the inductor in the ring segment between two rungs

L_2 = the inductor in the rung

C = the capacitor between two circular end rings

M = the mode of the birdcage resonator (set to 1)

N = rung numbers (set to 12)

Theoretical Calculation of Birdcage Coil

Based upon the computer simulation, the total rung number and the length of the birdcage coil are determined. The minimum diameter of the birdcage resonator is limited by the size of the MR localizer, that is, 35.5 cm. In order to reduce the maximum applied voltage across the capacitors, two capacitors are used and each rung is split into three segments. The schematic diagram of the birdcage resonator is shown in Fig. 5.9.

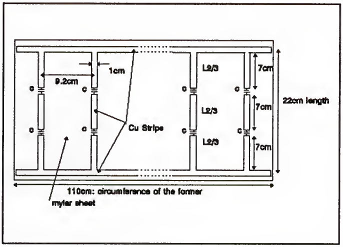

Figure 5.9 Schematic Diagram of the Birdcage Resonator.

Characteristics of Copper Foil

A copper laminate (copper-clad 250 from Electronic Products Division/3M and skin depth = 0.52 mil at 25MHz) was used for inductor fabrication in the rings and rungs [Vul92]. It is 0.1mm thick and 1cm wide with adhesive on one side. The experimental fitting function of the inductance with the length of the copper strips was tabulated by Vullo [Vul92]. The inductor implemented by the copper laminate can be modeled by the following equation [Gro73]:

$$L = 0.00508 * b * [\ln\frac{2*b}{w+h} + 0.5 + 0.2235 * \frac{w+h}{b}] \qquad \text{Eq. 5.3}$$

where L = inductance in uH

b, w, and h = length, width, and thickness in inches

Determination of Capacitors and Inductors

Once the geometric dimensions are defined, the inductors for rungs and rings can be easily calculated using Eq. 5.3. L_1 is 0.121uH and L_2 is 0.1698uH. The capacitance is determined by using Eq. 5.2. The capacitance is found to be 24.25pF. In order to reduce the maximum voltage applied

across the capacitor in the ring (see Fig. 5.9), two capacitors are used serially. Therefore, each capacitance is 48.5pF (actually, 37pF capacitance is used in the final tuning procedure to set the resonance frequency of the MR scanner to the middle of the tuning frequncy range of the impedance matching network). A ceramic capacitor (10TCCQ27 and 10TCCQ10 with 1000VDC and 300VAC rms and copper lead, which is manufactured by the Sprague) is used.

Impedance Matching Network

In order to use the birdcage resonator, the impedance of the resonator should be matched to that of the transmitter and the receiver of the MR scanner in the usual way, i.e., matching it to a 50-ohm resistor. We accomplished the matching by putting a pair of variable capacitors (30pF non-magnetic timmer capcaitor, Model 6030HPC, manufactured by UHF Power Inc.) in series with the resonator. The matching network is connected to one rung and one end ring. The matching network is shown in Fig. 5.10.

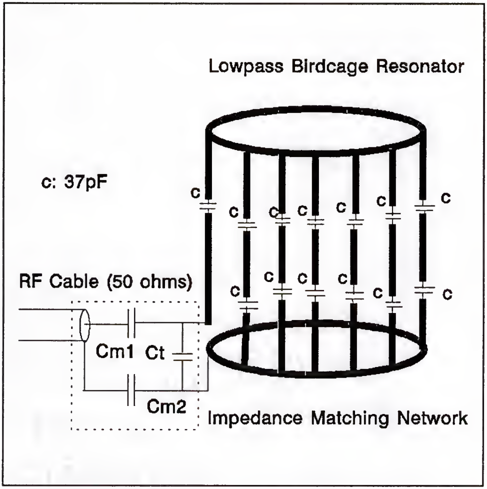

Figure 5.10 Impedance Matching Network. C_T is the tuning capacitor and consists of a variable capacitor (0-30pF) plus a 33pF and a 18pF. C_{M1} is a fixed capacitor (47pF). C_{M2} consists of a variable capacitor (0-30pF) and 18pF. C_{M1} and C_{M2} are called the matching capacitors.

Electrical Characteristics of the Siemens MR Scanner

The electrical parameters should be reviewed to design the impedance network. Table 5.1 lists the important parameters for the fabrication design of the birdcage resonator. The RF bandwidth of the birdcage resonator should be larger than 100 KHz for proper transmission and reception of the RF signals without RF loss. The resonant frequency of the MR scanner should be matched to the birdcage resonator by tuning the impedance matching network.

Table 5.1 Electrical Parameters of the Siemens Magnetom™ SP4000 MR scanner [Sie89]

No	Parameters	Specification
1	Main Magnetic Fields	1.0 Tesla
2	^{1}H resonant frequency	41.039740 MHz
3	Receiver (Rx) Bandwidth	max 66.6 KHz
4	Transmitter (Tx) Bandwidth	max 100 KHz
5	Gradient Magnetic Field	max 10mT/m
6	Rx and Tx Impedance	50 ohms
7	Reflectant Coefficients	less than 30 percent

Tuning Procedure

Four major electrical parameters should be considered in the design of the birdcage resonator: (1) operating frequency, (2) transmitter and receiver bandwidth, (3) reflectance coefficient and (4) loaded Quality Factor (QF) and unloaded QF of the birdcage resonator. Only the Siemens Magnetom™ MR scanner has been used to test the birdcage resonator

First, the frequency response of the birdcage resonator without the BRW ring and the MR water phantom was investigated. This measurement is done using the network analyzer (HP4958 Network Analyzer) in the laboratory over operating frequencies of 0Hz to 120MHz in order to see all resonant frequencies (six frequencies, see Eq. 5.2). The overall frequency response is shown in Fig. 5.11, where the resonance frequency is set to 40.3MHz (compared with the resonant frequency of the MR scanner). Note that there are some perturbations on the higher order resonant frequencies. The perturbation seems to be related to asymmetry of the birdcage coil. Fig. 5.12 shows the frequency response with 5MHz span, bandwidth of 529 KHz and the unload QF (quality factor) of 75. The 3dB bandwidth of the birdcage are larger than the bandwidths of the transmitter and the receiver of the MR scanner (see Table 5.1, Fig. 5.11, 5.12 and 5.13).

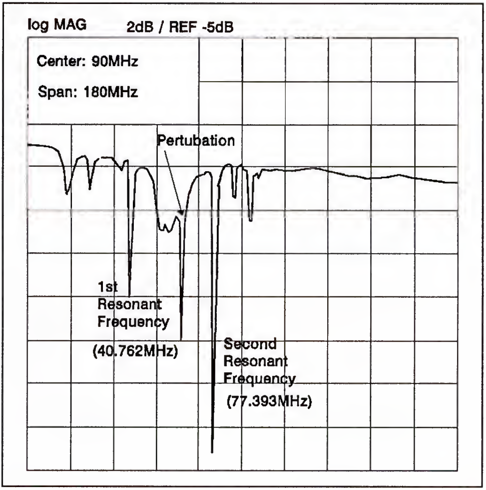

Figure 5.11 Overall Frequency Response of the Birdcage Resonator Only in the Laboratory. The frequency range is DC to 180 MHz. Only two resonant frequencies are shown in the figure.

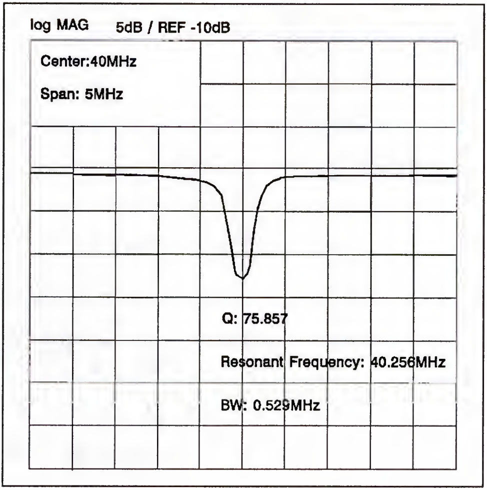

Figure 5.12 Frequency Response of the Birdcage Resonator Only Over Resonant Frequency Region. The unload QF is 75 and the bandwidth is 300 KHz. The resonant frequency is 40.1928 MHz and the bandwidth is 0.529 MHz. The unloaded QF is 75.857.

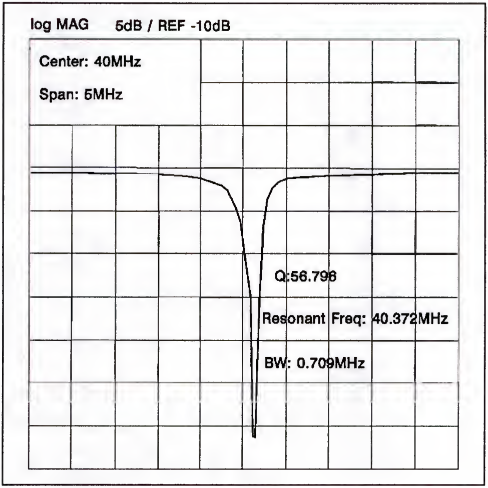

Fig. 5.13. Frequency Response of Test Phantom: MR BRW head ring, MR Localizer and MR water phantom. The loaded QF is 57 and the resonant frequency is shifted upward by approximately 100 KHz because of the inductive coupling between the end rung and the BRW head ring.

Second, the resonant frequency is shifted up by 100 KHz when the water phantom with the BRW head ring is placed in the birdcage resonator. This shifting up is caused by the inductive coupling between the conductive MR BRW ring and the inductors in the ring of the birdcage resonator, thus decreasing the effective inductance in the rung (see Eq. 5.2). The loaded QF is 57 and overall frequency response is shown in Fig. 5.13.

Third, there is another mechanism causing a frequency shift as much as 600 KHz. When the birdcage resonator is placed in the MR scanner, the inductors in the rings and the rungs are coupled inductively with the inductive coils in the MR scanner. The inductance in Eq. 5.2 decreases, thus causing the frequency to be shifted upward. Also the interaction between the birdcage resonator and the MR scanner increases the bandwidth of the birdcage resonator: approximately from 300 KHz to 600 KHz.

The birdcage resonator is rigidly placed by the MR former. Because of the bulky volume of the former, the center of the MR former is about 3cm above the isocenter of the MR scanner. Fig. 5.14 shows the geometric relationship between the birdcage resonator and the MR scanner. There is a 2cm gap between the former and the scanner table in order to prevent interaction between the birdcage resonator and

the body coil placed under the MR scanner table.

Fourth, MR water phantom with MR BRW ring and MR localizer are used to tune the impedance matching network. Adjust the tuning capacitor while monitoring the reflectant coefficient on the MR scanner until the reflectance coefficient is at minimum. Then, adjust the matching capacitor for fine tuning. Since this matching network is adjusted with a water phantom, there might be a situation where the reflectance coefficient is higher than 30 percent with a patient. If that happens, a re-tuning procedure should be done with a volunteer patient. This coefficient has been between 10 to 20 percent for the first fifteen stereotactic patients at the University of Florida.

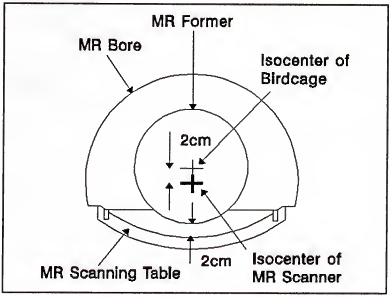

Fig. 5.14 Setup of the birdcage resonator in the MR scanner.

Phantom Study of the Birdcage Coil

The water phantom was used to evaluate the birdcage coil. The MR images are throughly examined in chapter 6. There is no noticeable non-uniformity in the water phantom as well as the localization rods. The detailed image analysis about spatial distortion with the water phantom will be described in chapter 7.

Clinical Application of Birdcage Coil

This birdcage coil has been used to treat more than fifteen stereotactic patient as well as seven depth electrode placement patients. In Fig. 5.15, one set of MR images is shown for demonstration of the clinical significance of the birdcage coil application. The imaging protocol for epilepsy patients is the same as the imaging parameters as mentioned previously. In order to increase the trans-axial resolution, a second set of images are obtained after the first set of images is scanned. The second set is shifted down by 1.5 mm. The resolution of the trans-axial plane is improved to 1.5 mm.

Figure 5.15 MR Film Images of a Epilepsy Patient with Birdcage resonator. Two sets of MR images are usually used to improve the nominal axial resolution to 1.5 mm. One set of MR images (14 slices) are obtained, then the second set is obtained by shifting down or up the whole sets of images by 1.5 mm. The imaging parameters used with an epilepsy patients are: 500 msec TR, 20 msec TE, 512 * 512 Matrix, 2 NEX and 3 mm slice thickness.

Conclusion

In this chapter, the birdcage resonator fabrication is described in detail. The linear type birdcage has been frequently for spectroscopy application, where the ratio of the length to the diameter of the birdcage resonator is larger than one in most applications. Therefore, it is possible to give very uniform magnetic fields in the center of the birdcage resonator [Syk91] [Sco88]. In our application, the ratio is approximately 0.6. The non-uniformity in the edge of the birdcage resonator might be expected. In the design of the birdcage resonator, the end effects due to the standing voltage of the end ring are ignored in the computer simulation even though it contributes magnetic fields in the transverse plane. The uniformity in the edges are expected to be lower than the middle of the birdcage resonator because of the roll-off effects as well as the effects due to the standing voltage in the end rings of the birdcage resonator.

In some publications, a shielding plate, which is called Faraday shielding plate, is used to isolate the resonator from the MR scanner, thus eliminating re-tuning procedure in the MR scanner [Vul92]. At the University of Florida, the shielding plate is not employed. Re-tuning of the birdcage is done with a MR water phantom as well as with

a volunteer patient was carried out. After the initial tuning, The birdcage resonator has been used for approximately two year without the need for re-tuning [Huh92].

In order to increase SNR and reduce RF exposure to a patient, the quadrature type birdcage resonator might be considered [Hay85]. The design concept of the quadrature type is the same as the linear type except for the isolation effects between two ports. Another expected problem is the cross talk between two RF waves. This problem might be solved using a plastic cable holder, where two seperate RF cables are placed with some distance between them (5 cm separation).

CHAPTER 6
ANALYSIS OF MR IMAGES WITH BIRDCAGE RESONATOR

Introduction

The birdcage resonator was designed with several assumptions as described in chapter 5. MR images, obtained by using the birdcage resonator, should be analyzed in order to improve the birdcage resonator. Although the birdcage resonator is frequently used because of higher uniformity and signal-to-noise ratio (SNR), a thorough evaluation of MR images has not been published yet, especially in radiosurgery applications.

In this chapter, the MR images are investigated by using several standard protocols [Dix88]. The following parameters will be used to represent the image quality: (1) uniformity, (2) SNR, (3) image spin/axis tilt angle (see Fig. 2.3 or Fig. 5.12), (4) flatness (defined later in this chapter) and (5) correlation between CT and MR images with square meshy structures (See Fig. 4.2) of the MR water phantom. The first two parameters of the MR images obtained by using the birdcage resonator will be compared to those obtained using the body coil. The image spin/axis tilt angles are used to examine the functionality of the image spin angle control (see Fig. 5.12).

The major sources of spatial distortion are the nonlinearity of the gradient magnetic fields and the artifacts due to the stereotactic frame (called the frame artifacts) [Wil87]. The nonlinearity of the gradient field largely affects the rod position of the MR localizer far away from the sensitive volume (50cm-diameter sphere) and is assumed to be ignored in the central region with the homogeneous water phantom [Sco88] [Sie88]. The frame artifacts were negligible with the body coil and were investigated in chapter 4. The frame deteriorates the image quality (especially uniformity) in the imaging plane close to the BRW head ring because it give asymmetrical loading effects to the birdcage resonator. Also the nonlinearity caused by the gradient magnetic fields introduces significant errors during the registration procedure (mapping CT or MR images in terms of BRW coordinates). The errors largely occur on the trans-axial coordinates because the image spin and axis tilt angle can be controlled mechanically and the resolution in the axial plane is much coarser than in other planes (3 mm vs 0.67 mm).

In this chapter the spatial distortion caused by the inhomogeneity will be investigated with the correlation between CT and MR images using a MR water phantom. In the chapter 7 distortion analysis with radiosurgery patients will be investigated. Inhomogeneity artifacts can be minimized when the MR scanner is properly shimmed according to technical

information supplied by the MR manufacturer when the magnitude of the gradient magnetic fields is 10 mT/m (1 guass/cm) [Sie89].

A computer program (MR QA program) is used to analyze the MR images. The program is written in C and runs on a Sun3/350 using the Sunview™ window environment. The water phantom is scanned using the parameters given in Table 4.1. The MR images are sent through the hospital's electronic network to the radiosurgery computer. The header file of each slice image is stripped and a single image file is generated. The user interface of the MR QA program is shown in Fig. 6.1 and Fig. 6.2. The explanation of detailed figures will be covered in a later section.

Specification of Imaging Parameters

In general, image quality is defined over the central region, eighty percent of a phantom [Dix88] [Pri90]. However, in the radiosurgery application, there are two regions: central region and peripheral region. The central region is very important from the clinical point of view while the peripheral region is used to register each slice. Two different approaches should therefore be examined to evaluate the image quality of the MR images obtained by using the

birdcage resonator. As mentioned in chapter 5, the magnetic field at the peripheral region is considered in the birdcage resonator design.

Signal-to-Noise Ratio (SNR)

The SNR parameter is very useful to represent the image quality of the birdcage resonator and especially to investigate the end effects of the birdcage resonator. Two regions are selected to calculate the SNR: the signal region and the noise region. The window size to calculate the SNR should be large enough to significantly represent the random nature of the noises in the noise region. The region size for the signal and noise is set to a 41 pixel-by-41 pixel window. The window size should be large enough so the statistical fluctuation is independent of window size. The standard deviation of the noise region starts to stabilize when the window size becomes 21 pixel-by-21 pixel. A value for the window size twice this size is chosen to provide margin and to prevent statistitical fluctuation of average and stadard deviation. The signal region is represented by the white box in the right side of the water phantom shown in the right canvas in Fig. 6.1. The average signal is defined as the average pixel value within the signal region. A noise region is represented as the white rectangular box between two rods. The noise is defined as the standard deviation

(represented by noise std) of the pixel values within the noise region. Table 6.1 summarizes the SNR in terms of the BRW Z coordinate (or trans-axial coordinate). The SNR is defined in Eq. 6.1.

$$SNR=\frac{average\ signal\ -\ average\ noise}{noise\ std} \qquad \text{Eq. 6.1}$$

where the average signal is the average pixel value in the signal region and the average noise is the average pixel value in the noise region. The noise std represents one standard deviation of the pixel values in the noise region. The BRW Z represents the trans-axial coordinates of each MR image slice.

From the SNR table, the SNR changes over broad ranges: 1.2 to 8.8. Since the change of the noise average and noise standard deviation, the signal (averaged pixel values in the signal region in Fig. 6.1) can represent the uniformity of the each slice even though the signal region is smaller than that of the phantom size. The signal at BRW Z = -76.7 mm is much smaller than that of the other end (BRW Z = +81.4 mm); this might be related by the eddy current effects induced by the stereotactic frame. The SNR varies on an order of magnitude (1.2 to 8.8) compared to the 80 percent design goal when determining the length of the birdcage resonator (see chapter 5). This means that the Bio-Savart theorem is of limited use

or that the current in the two end rungs should be considered to calculate the magnetic field inside the birdcage resonator. The SNR in the slice close to the BRW head ring is relatively lower than that in the slice in opposite slice.

Table 6.2 Signal-to-Noise Ratio (SNR) with Water Phantom

No	BRW Z (mm)	Signal Pixel	Noise Avg Pixel	Noise Std Pixel	SNR
4	+81.4	169	59	30	3.6
2	+65.6	232	59	30	5.6
3	+49.3	275	59	31	8.9
4	+32.9	312	56	28	8.9
5	+16.8	321	57	31	8.9
6	+0.9	325	59	30	8.8
7	-15.1	303	62	31	7.7
8	-31.0	272	59	29	7.1
9	-46.7	211	58	31	4.8
10	-60.7	148	59	29	3.0
11	-76.7	95	57	31	1.2

<u>Uniformity</u>

Uniformity in considered in two regions: (1) the central region and (2) the peripheral region. The uniformity of the central region is represented by the SNR in the previous section. The uniformity of the peripheral regions can be

quantitatively represented by the pixel values of the straight rods: rod 1, 3, 4, 6, 7 and 9 (see Fig. 5.5). Practically, a large water phantom is needed to cover the peripheral region and analyze the uniformity accurately. However, the larger phantom might give different loading effects to the birdcage resonator, therefore the uniformity thus obtained might not be useful to estimate the uniformity of the birdcage resonator.

Therefore, larger volume of a water phantom could be used to estimate the uniformity of the birdcage resonator. However, the larger phantom might introduce different loading effect to the birdcage resonator. The uniformity obtained with the larger phantom is not clinically useful. Instead of using the larger water phantom, the signal values of the rods of the MR localizer is used to estimate the uniformity of the birdcage resonator. In this dissertation, the signal values of nine rods in each slice are used to represent the uniformity of the birdcage resonator. Because of the partial volume effects, it is not straightforward to set the threshold value to define the rods. The manual thresholding method is used to determine the pixels belonging to each rod. The threshold values are adjusted until the number of pixels belonging to each rod becomes between forty to sixty, which is the range of pixel counts considering the partial volume effects. Once the threshold values are determined, the average pixel values larger than the threshold are averaged

and listed as the average pixel values. When measuring the uniformity, a 4 cm-thick volume of the water phantom is used to determine the uniformity in the peripheral region.

The peripheral uniformity is automatically obtained by using the computer program and is summarized in Table 6.2. From these data, the peripheral uniformity over the six straight rods can be defined as the modified definition of the uniformity commonly used in Eq. 6.2.

$$Peripheral\ Uniformity = \frac{S_{\max} - S_{\min}}{S_{\max} + S_{\min}} \qquad \text{Eq. 6.2}$$

where S_{max} and S_{min} represent the maximum and the minimum average pixel values of a rod over trans-axial coordinates.

The peripheral uniformity for each rod thus defined in the previous page ranges from 5 to 10 percent. When there is perfectly uniform, the peripheral uniformity is zero percent. The average pixel values of rod 4 is lower than those of other rods by 30 percent. This phenomenum might be related to either the asymmetry of the birdcage resonator or the improper configuration of the impedance matching network. The presence of the impedance matching might disturb the symmetry structure of the birdcage resonator.

Another definition of the uniformity can be stated in the following way using the profile along the horizontal and the vertical axis of each images. Because of the large matrix, a smoothing filter should be considered. The nine-point equally-weighted smoothing filter can be employed to remove the random noises. Eq 6.2 is applied along 80 percent of the vertical and horizontal axis of each image. Fig. 6.1 and Fig. 6.2 show two slice of MR images to illustrate the procedure to determine the uniformity along two lines.

The uniformity in the central region can be determined by using Eq. 6.2. S_{max} and S_{min} are obtained over 80 percent of the horizontal and the vertical profile in each slice. For example, S_{max} and S_{min} in the vertical profile (represented by Y profile in the left canvas of Fig 6.1) are 88 and 70 percent, respectively (the profile is normalized by the maximum number). Therefore the vertical uniformity is 11 percent ((88-70)/(88+70)). The uniformity at the axial coordinate of -15.2 mm is about 10 percent.

Image Spin/Axis Tilt Angles and Flatness

In order to investigate the functionality of the MR former, image spin and axis tilt angle are used (defined in the Fig. 2.3). The image spin angle and the axis tilt angle should be checked periodically with the MR water phantom

Table 6.2 Peripheral Uniformity of Birdcage Resonator with T1-Weighted Imaging

No	BRW Z	Rod 1	Rod 3	Rod 4	Rod 6	Rod 7	Rod 9
1	+23.7	1484	1468	850	1395	1406	1079
2	+20.6	1333	1421	833	1259	1319	1099
3	+17.5	1444	1421	873	1317	1357	1151
6	+14.6	1345	1367	851	1303	1333	1156
6	+11.5	1389	1431	908	1330	1207	1184
6	-6.6	1389	1340	883	1307	1357	1184
7	+5.4	1460	1425	960	1338	1232	1145
6	+2.5	1367	1328	945	1296	1343	1172
3	-9.7	1435	1413	1001	1371	1384	1189
10	-3.6	1345	1340	914	1338	1311	1189
11	-6.6	1453	1431	982	1414	1414	1210
12	-9.7	1358	1340	850	1415	1359	1223
13	-12.9	1461	1439	1013	1439	1424	1255
14	-15.9	1509	1435	1067	1475	1495	1317

because the adjustment of the MR scanner (for example, by inhomogeneous shimming of the magnet to achieve the magnetic field homogeneity) can introduce possible distortions. The limit for non-corrected images of the image spin and the axis tilt angle at the UF radiosurgery system is 0.386 degrees. It is easy to adjust the spin angle control within one pixel deviation over 345mm (the distance between rods 1 and 6) to satisfy the specification (see Fig. 5.4.C).

Even though these angles are adjusted with the MR water

phantom, these angles should be verified with a stereotactic patient. The image spin/axis tilt angles are summarized in Table 6.3. All image spin angles are within the specification. The average axis tilt angle is about 0.73 degrees (2 mm deflection over 140 mm). That means that the MR former is tilted by 2 mm. The MR former should be carefully placed on the MR scanner in order to decrease the axis tilt angle within the specification

Table 6.3 Image Spin/Axis Tilt Angles and Flatness of a Radiosurgery Patient ("*" indicates within the specification.)

No	BRW Z	spin angle	tilt angle	flatness
1	81.4	*	0.585	1.31
2	65.6	*	0.421	1.41
3	49.3	*	0.787	1.10
1	32.9	*	0.578	*
5	16.8	*	0.714	*
6	0.9	*	0.743	*
7	-15.1	*	0.435	*
8	-31.0	*	0.454	*
9	-46.7	*	0.838	1.38
10	-60.7	*	1.745	1.03

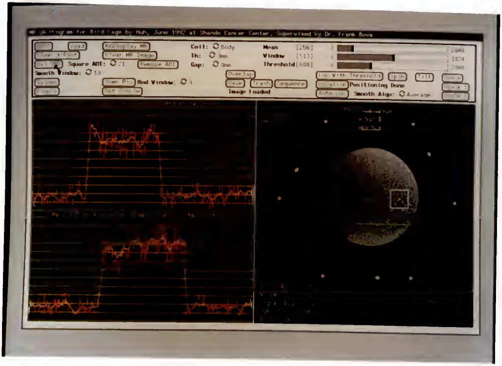

Fig. 6.1 Computer program to calculate the SNR of the MR image with the trans-axial coordinate of -15.2 mm. The white window (noise region and signal region) in the right canvas is used to calculate the SNR. The SNR is 7.6 or 18dB.

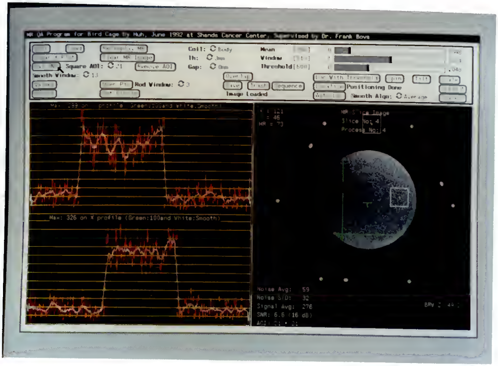

Fig. 6.2 Profile in the trans-axial plane of +49.2 mm in BRW coordinate. The white line in the left canvas represents the averaged profile with 9-pixel smoothing. The red line is the actual pixel value without smoothing. Two profiles in the left canvas are obtained along two lines represented by the green lines in the right canvas.

Flatness

In order to represent the spatial distortion, the flatness is a very useful parameter in the peripheral regions for the image registration procedure. The flatness is defined as the maximum deviation of three distances (the distance between rods 1 and 6, between rods 3 and 7 and that between rods 4 and 9) from the average distance of the three distances. The flatness of a stereotactic patient over 14 slices is summarized in Table 6.5. The specification of the flatness is one pixel. From Table 6.3, the flatness increases in both ends, as expected. This is related to the nonlinearity of the gradient magnetic field (see Table 6.5).

Correlation between CT and MR Images

In order to investigate the correlation between two imaging modalities, the square meshy structure is placed in the MR water phantom (see Fig. 4.2). The experimental phantom might be called the 2D phantom because it is used to investigate the spatial distortion in a single plane only. For our radiosurgery system, the correlation procedure is to locate sixteen hollow plastic tubes in CT and MR images in the axial plane and then the discrepancies between two coordinates in CT and MR images are examined. In order to reduce the

tube localization error, the CT and MR images are four times magnified (one pixel is 0.17 mm * 0.17 mm) and the center of each tube is determined by averaging three coordinates with manual fitting.

This 2D approach is carried out with three sets of CT and MR images with the axial coordinates of -47.3 mm, +5.7 mm, and 56.8 mm. The volume covered by the 2D phantom is 7.6 cm * 7.6 cm * 10 cm. This volume is within the sensitive volume (50 cm-diameter sphere), where the inhomogeneity is less than 0.7 ppm according to the Siemens manufacturer [Sie90]. The major source of the spatial distortion is the susceptibility artifacts between the hollow plastic tube and 0.25 percent saline water. For example, the susceptibility artifacts at air/water interface is about 15 ppm [Sie89] [Wil87]. When the strength of the gradient magnetic fields is 10 mT/m (1 Gauss/cm), 10 ppm in the susceptibility means a spatial shift of 1 mm. The expected maximum spatial distortion might be 1.5 mm according to this calculation.

Table 6.4 and 6.5 and 6.6 list the absolute coordinates in CT and MR images and the differences between them. Fig. 6.3 illustrates the tube identification number used in Tables 6.4 through 6.6.

Table 6.4 CT/MRI Correlation with Axial Coordinate of +56.8 mm

No	AP BRW coordinate (mm)			LAT BRW coordinate(mm)		
	CT	MR	Error	CT	MR	Error
1	+37.5	+37.3	+0.2	+29.1	+31.0	-1.9
2	+34.3	+33.9	+0.4	+3.7	+5.8	-1.9
3	+31.3	+30.9	+0.4	-21.6	-19.7	-2.1
4	+28.0	+28.0	0.0	-47.1	-45.1	-2.0
5	+12.2	+11.5	+0.7	+32.3	+34.3	-2.0
6	+9.1	+8.6	+0.5	+7.1	+9.0	-1.9
2	+5.7	+5.6	+0.1	-18.6	-16.8	-1.8
[illegible]	+2.7	+2.7	0.0	-43.9	-42.1	-1.8
9	-13.0	-13.6	+0.6	+35.5	+37.1	-1.6
10	-16.2	-16.6	+0.4	+10.1	+12.0	-1.9
11	-19.4	-19.7	+0.3	-15.2	-13.6	-1.6
1[illegible]	-22.8	-23.1	+0.3	-40.5	-39.0	-1.5
13	-4[illegible].4	-4[illegible].7	+0.3	+38.7	+40.0	-1.3
14	-41.4	-41.7	+0.3	+13.5	+14.9	-1.4
15	-44.6	-44.9	+0.3	-12.0	-10.5	-1.5
16	-48.0	-48.0	0.0	-37.2	-36.1	-1.1

Table 6.5 CT/MRI Correlation with Axial Coordinate of 4.7 mm

No	AP BRW coordinate (mm)			LAT BRW coordinate(mm)		
	CT	MR	Error	CT	MR	Error
1	-38.4	-38.8	+0.4	+29.7	+30.4	-0.5
8	+34.5	+33.6	+0.9	+4.2	+5.1	-0.9
3	+31.1	+30.7	+0.4	-20.9	-20.2	-0.7
6	+27.9	+27.5	0.4	-46.3	-45.1	-0.8
9	+12.3	+11.4	+0.9	+33.1	+33.6	-0.5
6	+9.1	+8.5	+0.4	+7.4	+8.3	-0.9
7	+5.7	+5.4	+0.3	-17.9	-17.1	-0.8
8	+2.7	+2.2	+0.5	-43.3	-42.6	-0.7
9	-12.8	-13.7	+0.9	+35.6	+36.3	-0.7
10	-16.2	-16.8	+0.4	+10.8	+11.4	-0.6
11	-19.4	-19.8	+0.2	-14.5	-13.9	-0.6
12	-22.8	-23.1	+0.4	-39.7	-39.2	-1.5
10	-38.4	-38.8	+0.4	+39.5	+39.7	-0.2
14	-41.6	-42.1	+0.5	+14.0	+14.2	-0.2
15	-44.6	-45.1	+0.5	-11.2	-11.2	0.0
16	-48.0	-48.2	+0.2	-36.5	-36.3	-0.2

Table 6.6 CT/MRI Correlation with Axial Coordinate of -47.3 mm

No	AP BRW coordinate (mm)			LAT BRW coordinate(mm)		
	CT	MR	Error	CT	MR	Error
1	+37.3	+36.0	+1.3	+30.1	+29.3	+0.8
8	+34.0	+33.4	+0.6	+4.7	+2.5	+2.2
3	+30.6	+30.4	+0.2	-20.6	-21.7	+1.1
4	+27.4	+27.1	0.3	+4[illegible].0	+37.1	+2.5
5	+12.0	+11.2	+0.8	+33.3	+31.2	+2.1
8	+8.8	+8.1	+0.7	+8.1	+5.4	+2.7
7	+5.4	+5.1	+0.3	-17.2	-19.5	+1.7
8	+2.0	+1.7	+0.3	-42.6	-45.1	-0.5
8	-13.5	-14.1	+0.6	+36.5	+33.7	+2.8
11	-16.7	-17.3	+0.6	+11.3	+8.5	+2.8
11	-19.9	-20.2	+0.3	-14.0	-16.6	+2.6
12	-23.3	-23.2	-0.1	-39.2	-41.9	+2.7
13	-38.7	-39.2	+0.5	+40.0	+37.1	+2.5
13	-42.1	-42.4	+0.3	+14.5	+11.9	+2.6
15	-45.3	-45.5	+0.2	-10.6	-13.2	+2.6
16	-48.5	-48.3	+0.2	-35.8	-38.7	+2.9

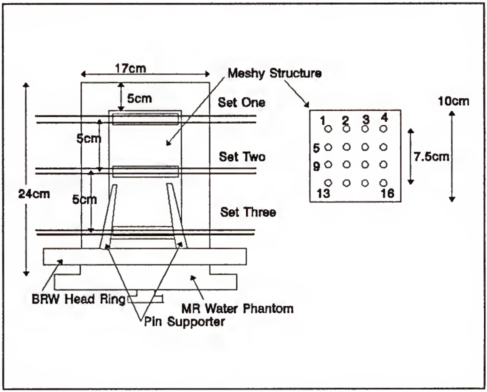

Figure 6.3 Experimental Setup for Spatial Distortion. The meshy structure is tilted by 2mm over 10cm. There are three sets of slices: Set One, Two and Three. Set Two is placed 1cm over the localization pins to prevent star pattern artifacts (or beam hardening artifacts). The isocenter of the MR scanner is set to the center of Set Two by using the laser of the MR scanner. The meshy structure is rotated by fifteen degrees. The tube number under the No column in Tables 6.4 through 6.6 represent the order of the tubes shown in the right figure.

From three tables about the coordinate information, the following table is obtained to analyze the trends of the tube position in CT and MR images.

No	AP Coord. Diff. average	std	LAT Coord. Diff. average	std	Axial Coord.
1	0.30	0.20	-1.7	0.3	+56.8mm
2	0.53	0.26	-0.61	0.35	+4.7mm
3	0.44	0.31	+2.35	0.60	-47.3mm

From the results, Set Two (the slice at the isocenter on the MR scanner, or 4.7 mm axial coordinate) has one pixel (one pixel is 0.68 mm) error in AP and lateral coordinate between CT and MR images. Set One (the slice far way from the BRW head ring) has a half pixel in AP and two pixels error in lateral coordinate. Set Three (about three cm from the surface of the BRW head ring) has one pixel in AP and about four pixels error in the lateral coordinates. The tube localization errors in Set One and Set Three give very interesting results: the displacement errors are about 4 mm in the lateral coordinate even though there are 0.1 mm errors in the AP direction. Set One has the least perturbation from the stereotactic frame and the Set Three might be affected most by

the frame. These error ranges are much larger than that of the inhomogeneity or nonlinearity of the gradient magnetic fields. The major source of at least "five pixel error" displacement is related the stereotactic frame. The displacement error might be larger if 3D distortion were included. This error analysis should be carried out by using the 3D phantom.

Conclusion

These procedures have been used to treat more than fifteen radiosurgery patients and seven depth electrode placement patients at the University of Florida. Clinically, there has been excellent agreement between the CT and MR images for depth electrode placement. For the depth electrode patients, the middle or central portion of the volume occupied by the MR localizer has been very frequently used. Even though there is detailed measurement data, fairly good agreement has been observed from the postoperative CT scanning (from personal communication with the neurosurgeon).

For the stereotactic radiosurgery patients, MR images have been used to treat meningioma, glioma and brainstem tumors. From personal communications with the neurosurgeon, the displacement errors observed were more than 3 mm (whenever the brain stem or the tumor was located close the stereotactic

frame). This clinical situation is related to the five-pixel errors in the lateral direction discussed above. For other cases where the tumors are placed in the middle or the upper portion of the MR localizer, there has been at most two-pixel errors.

CHAPTER 7
CORRELATION ANALYSIS

Introduction

There are many reports regarding the correlation accuracy between CT and MR images in the radiosurgery society [Kon89] [Lun86] [Mos91] [Pel89] [Syk91]. The correlation accuracy has been investigated in two different fields: (1) functional procedure (2) target localization. In the functional procedure [Kon89], a mid-sagittal MR image is used to identify the anterior commissure (AC) and the posterior commissure (PC). Axial and coronal slices are then taken to the center of the AC and the PC. Measurement using two imaging modalities showed that the MR plane differed by 1mm or less in approximately 20 of 33 patients. Also, in the target localization, correlation between CT and MR images for right-left, anterior-posterior, and superior-inferior measurements were 0.98, 0.99 and 0.99, respectively. A slight variation was observed with the non-central (more than 2cm from frame center) and was not mentioned in the publication.

In a later paper from the discussion from Kondziolka et al [Kon92], the discrepancies between CT and MR images were

caused by the physical properties of data acquisition, but the one pixel (1.95 mm in x-axis and 2.16 mm in y-axis) difference, resulting in 3.25 mm distance error in the hypotenuse vector measurement in target selection accounts totally for the variance observed. The range of errors even occurs in the comparison of sequential CT scans depending upon the CT pixel size. They suggested a larger matrix or smaller FOV to decrease the errors and more images (or less slice thickness, for example, 3 mm) to reduce the errors in the axial coordinate. The errors were reduced, but could not be eliminated. In this publication, the errors caused by the functional procedures are not mentioned.

Heibrun et al. [Hei87] estimated the spatial distortion between MR images with a test phantom rather than using CT and MR images. The 3D localizer was developed to register the images on axial, sagittal and coronal plane. This method is straightforward, but could not be employed with our MR localizer, which is limited to using a plane other than axial.

Lunsford et al [Lun86] reported from postoperative CT images that the target precision is within 1 mm using CT and MR stereotaxis. They presented three surgical cases (astrocytoma, glioblastoma and hematoma) for the coordinate differences between CT and MR images shown in Table 7.1:

Table 7.1 Comparison of stereotactic coordinates in mm with CT and MR images in three surgical cases [Lun86].

No	Lesion site	MR x	CT x	MR y	CT y	MR z	CT z
1	rf frontoparietal	60	61	98	96	90	92
2	rf deep frontoparietal	70	69	76	76	76	80
3	rf parietal	72	73	79	78	66	65

From the table, most errors are within 1 to 2 mm except the z-axis for rf deep frontoparietal. This comparison might give some idea about the correlation between CT and MRI, but two imaging modalities give different pathological information. Therefore, 1 to 2 mm errors in the target localization on the radiographic images do not have any significance.

Villemure et al. [Vil87] investigated the correlation between MR images and ventriculography in six patients undergoing stereotactic localization. The correlation of coordinates and measurements of the anterior (AC) and posterior commissures (PC) is +/-1 mm in most cases, but up to 4 mm in two cases. They assumed that the frame itself and a piece of brass in one bar of the frame introduced such large errors. The frame and its fixtures are away from the target (AC or PC) and the brass does not introduce significant spatial distortion even though the target might be obscured.

Judging from the 4mm error, the major source of the spatial distortion might be related to either the frame artifacts or improper shimming of the MR scanner.

Peters et al. [Pet87] also investigated the correlation between CT and MR images. They reported that the coordinate determination is +/- 1mm and there are 3 to 4 mm errors in the axial coordinate because of the misplacement of fiducial markers caused by the paramagnetic effects associated with the stereotactic frame. From their discussion, the misregistration of the fiducial markers should be considered when the MR-compatible head ring with MR localizer is scanned to investigate the spatial distortion.

From the investigations from other institutions to correlate CT and MR images, several facts should be mentioned: (1) the errors in coordinates between CT and MR images might be caused by the registration procedure or coordinate determination procedure, and these error occur, in general, in the axial coordinates, (2) the target should be defined in CT and MR images without ambiguity, (3) the target, occupying finite volume, is also used to correlate CT and MR images. This approach might be misleading when the targets are visualized differently in CT and MR images.

Procedure for the Correspondence

In this section, the correlation procedure between CT and MR images will be described. CT and MR images of the stereotactic patients and depth electrode placement patients are used to investigate the correlation. The MR images are obtained by using the birdcage resonator and the scanning techniques mentioned the Table 4.1 with 3 mm slice thickness and T1-weighted images. For stereotactic patients, only one set of MR images are used, taking eight minutes for each patient. For the depth electrode placement patients, two sets of MR images are used to improve the axial resolution to 1.5 mm. Therefore, two different types of MR are used and are separately summarized to investigate the effects of the thinner slice thickness upon the correlation accuracy.

Background

CT and MR images are obtained using the GE9800 Advantage™ and the Siemens Magnetom™ SP4000, respectively. Most MR images could be registered without a user intervention by properly setting the threshold value. For some MR images with low SNR, for example, T2-weighed images, the registration procedure might need user intervention to process the rods of the MR localizer. Protons in the rod have short T2 times (20 msec) and decay very fast with long TR times (approximately 2

sec). Therefore, the pixel values of the rods are on the same order of that of background noise. In some clinical situations, the pixel values of certain rods become lower because of asymmetrical loading effects which are patient specific.

Target Type and its Selection

Two types of targets are compared in the CT and MR images: a point target or a tumor target. The point target is the anatomical feature with small volume (for example, the center of the eyeball, aqueduct) which can be located with +/- one pixel errors. The reason to select a small target is to get rid of the possibility which introduces intra-user variability. The selection of the point targets is done with the help of a neurosurgeon (Dr. William Friedman, a PH.D committee member of the author).

The procedure to locate the point target is carried out in two different ways: (1) select the target center in the sagittal plane and locate the target center in the trans-axial plane and (2) select the target center in the axial plane and locate the target center in the sagittal plane.

The tumor target is also used to correlate the CT and MR images. The localization procedure for the tumor target is

carried out by using the geometric center method (see chapter 2) in three planes and the coordinates of the tumor target are averaged. The procedure is repeated in CT and MR images. The coordinate differences in three coordinates (CT coordinate minus MR coordinate of the target) are used to investigate the possible trends among the tumor targets. For example, if only chemical shifting artifacts are the dominant factor in spatial distortion, the coordinate difference in the y-axis (or lateral direction) should be positive (depending upon the physical characteristics of the target and its neighbor organs) and the relative coordinate in x-axis (or AP direction) and the coordinate difference in x-axis should be random because conventional directions of frequency coding and phase coding are used at the University of Florida. The detailed explanation about the chemical shift artifacts will be given in a later section.

Correlation with Radiosurgery Patients

At the University of Florida, radiosurgery patients are scanned with 3 mm slice thickness without any gap using the T1-weighted imaging. For some patients, two sets of images are used to cover fairly big tumors, for example, 3 cm diameter sphere. With TR = 500 msec, 28 slice images are used with two sets of scanning. It takes about sixteen

minutes. The spatial resolution in the trans-axial coordinate is 3 mm and the intermediate slices are obtained in the tumor localization using linear interpolation. The maximum possible error might be 1.5 mm. The point organ and the tumor correlations are used with radiosurgery patients. This correspondence has been done with ten of the patients treated at the University of Florida.

Point Correspondence

The landmarks used to correlate the CT and MR images should be defined with minimum uncertainty of locating them. The seventeen point organs in Table 7.1 were selected by a neurosurgeon. These organs or the centers of these organs are identified in the CT and MR images by a neurosurgeon. The spatial differences between two coordinates are listed as dAP, dLAT and dAx. For example, the dAP represents the difference in the AP coordinates in the CT and MR images.

The spatial differences in the trans-axial coordinate are less than 1mm. This implies that the spatial distortion is limited in the AP and the lateral planes for thin slices. Most spatial distortion occurs in the lateral planes. It might be related to the chemical shifting artifacts which occur in the frequency modulation axis.

Table 7.1. Correspondence between CT and MRI. The dAP, dLat and dAx are the difference in mm in stereotactic coordinates.

No	Landmark	dAP	dLat	dAx
1	aqueduct	+1.9	+0.1	+0.4
2	cerebral aqueduct	-0.1	-0.3	-0.5
3	cerebral aqueduct in mid brain	+0.2	-0.3	-1.0
4	foramen of Monro	+0.2	-0.3	+0.0
5	center of pineal gland	+0.9	+0.9	+0.5
6	sulcus hits midline falx	+0.2	-2.3	+0.4
7	sulcus meets skull	+0.1	-0.3	+0.4
8	fastigium on mid sagittal	+1.3	+0.7	+0.4
9	right optic nerve junction	+1.3	-2.3	-0.3
10	left optic nerve junction	-0.6	-1.0	-0.3
11	right optic nerve meets eyeball	-0.7	+0.9	+0.1
12	left optic nerve meets eyeball	-0.1	+1.6	+0.0
13	center of lens of left eye	+0.1	+0.1	-2.0
14	center of right MCA bifurcation	+0.0	-3.6	-0.5
15	center of left MCA bifurcation	+0.0	-0.3	+0.5
16	right cerebellum tonsil	+0.4	+1.3	-0.9
17	left cerebellum tonsil	+1.3	+2.7	-0.9

Tumor Correspondence

Patients with small acoustic, meningioma, glioblastoma and metastasis have been analyzed with MR and CT at the University of Florida. These tumors have very similar shapes in the CT and MR images. The spatial differences are less than about 1.0 mm except with the meningioma. This might be related to the susceptibility artifacts. Its effects are pronounced in the boundaries of the regions which have different susceptibilites. Susceptibility artifacts and its effects will be described in the later section of this chapter.

Correlation With Depth Electrode Placement

The MR images have been used to place depth electrodes for seven patients in the past six months. The MR images are primarily used to locate the part of the brain where the electrode is to be placed and to investigate the path from the surface to the target. The CT images are used to calculate the entry point of the depth electrode and are reviewed along the path of the depth electrode. The MR technique is the same as for radiosurgery patients except for thin slice thickness. The effective slice thickness used is 1.5mm, while the nominal slice thickness is 3mm. The MR images for depth electrode

Table 7.2 Tumor Correspondence (Note: #1 and #2 represent acoustic tumors in different patients)

No	Tumor	dAP	dLAT	dAX
1	acoustic (#1)	+0.2	-1.9	+0.4
2	acoustic (#2)	-0.7	+1.1	-0.6
3	metastasis	-0.1	-0.4	+0.4
4	pituitary adenoma	+0.7	-0.2	+0.4
5	meningioma	+1.8	-1.6	-2.1

placement covers about 4 cm thick volume of the brain with 28 slices (14 slices with 3 mm slice thickness two times), therefore the resolution in the trans-axial coordinates should be more accurate than that of the radiosurgery patients. The major source of the discrepancies between the CT and MR images might be related to susceptibility artifacts, that is lateral coordinates rather than trans-axial coordinates.

<u>Point Analysis With Fastigium</u>

The fastigium is defined in the trans-axial planes of the MR images and the lateral coordinate of the center of the fastigium is chosen first. In the sagittal planes, the trans-

axial and the AP coordinates are determined by finding the center of the fastigium. Next, this procedure is repeated in the CT images. According to the results, most distortion occurs in the trans-axial and the AP coordinates. The fastigium of four patients was investigated with the same localization procedure. Most errors occur in the AP and trans-axial coordinates. This is opposite to the findings in Table 7.1. This interesting result might be related to the chemical shifting distortion (will be described in the later section) and any localization errors performed by the user. If the image were shifted only in the lateral direction, the AP and the trans-axial coordinates should be the same.

Table 7.3 (A) Correlation Results with Fastigium

Anatomical Feature	dAP	dLAT	dAX
fastigium (#1)	+0.9	+0.0	-0.9
fastigium (#2)	+0.[illegible]	+0.0	-1.2
fastigium (#3)	+1.3	+0.0	-1.4
fastigium (#4)	-0.5	+1.0	-1.4

For the following organs, the localization procedure used with radiosurgery patients is employed to determine the spatial distortion. For the optic nerves and the aqueduct, there is no noticeable shift in any coordinate.

Table 7.3 (B) Correlation with Optic Nerve Meeting Eye Ball

Left/Right	dAP	dLAT	dAX
Right	-0.5	-0.5	-2.2
Left	-0.3	-0.3	-2.2
Right	+2.4	-0.5	+0.9
Left	+0.6	-1.4	+0.9
Right	+0.9	+1.6	-1.1
Left	+0.9	+0.5	-1.1
Right	-1.1	+1.5	-2.9
Left	-0.8	-1.5	-2.9

Table 7.3 (C) Correlation Results with Aqueduct

No	dAP	dLAT	dAX
Aqueduct (#1)	-0.2	+0.7	-1.5
Aqueduct(#2)	+1.1	+0.3	+0.1
Aqueduct(#3)	-1.6	+1.3	-3.3

For some organs mentioned in Table 7.3 (E), the spatial distortions have the same trends as shown in the radiosurgery patients in Table 7.1. The difference is that the trans-axial distortions are much smaller because of the higher resolution.

Table 7.3 (D) Correlation Results with Other Organs

No	Organ	dAP	dLAT	dAX
1	right mammillary body	+1.0	+0.4	+0.0
2	left mammillary body	+1.4	-1.0	+0.0
3	right inferior temporal horn	+1.0	+1.2	+0.0
4	left inferior temporal horn	-0.2	-0.2	+0.0
5	anterior commissure (#1)	+2.0	+0.3	+0.5
6	anterior commissure (#2)	+0.6	+0.6	+0.1

Artifacts in MR images

There are four possible sources of distortion in the MR images: (1) misregistration of the MR images due to the nonlinearity of the magnetic fields, (2) susceptibility artifacts, (3) chemical shifting artifacts and (4) frame artifacts, (4) motion, (5) blood flow and (6) CSF flow. The nonlinearity effects of the magnetic fields should explain the displacements in the trans-axial coordinates. However, its effects can be ignored clinically from the analysis data in Table 7.1. In this section, the second and the third artifacts are described.

Susceptibility Artifacts

In general, the signal obtained from a macroscopically homogeneous tissue will not be compromised by susceptibility artifacts, because the magnetic field is locally homogeneous [Tho86] [Sie89]. On the other hand, at interfaces between tissues of different magnetic susceptibility, hence different magnetic fields, a local field gradient will be present causing dephasing of the signals and spatial misregistration. Figure 7.1 illustrates the local field gradient between tissue and air. In most cases, this gradient in the intracranial imaging is small. However, the large susceptibility difference present, for example, at the interfaces between the tissue and air can lead to substantial signal losses. This is especially true for gradient-echo sequences. In the SE sequences, the 180-degree RF pulse usually eliminates this signal loss by reversing the dephasing. The actual misregistration with 10 ppm is about 1 mm. This error range can not be significant considering the one pixel limitation to define a tumor in the treatment planning.

Chemical Shifting Artifacts

Chemical shifting is the reason for artifacts in MR images which are manifested as misregistration of signals at the fat/water interface in the readout direction, that is, the

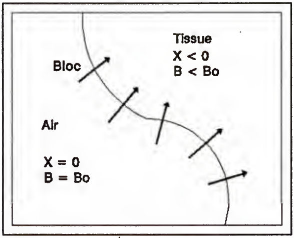

Figure 7.1 Schematic diagram of an air/tissue interface, generating a local magnetic gradient field B_{loc} due to the different magnetic susceptibility of air and tissue [Sie89]

lateral direction [Tho86]. This effect is due to the different chemical environments of protons associated with a shielding effect with respect to the main magnetic fields, thus causing a different resonant frequency of the involved protons. The chemical shift for the fat/water interface is 3.5 ppm, which is translated to 147 Hz at the 1.0 Tesla MR unit. For example, the lipid proton has lower resonant frequency than that of the protons in water. When applying the readout gradients in order to spatially encode the protons, the computer reconstruction algorithm does not differentiate between frequency changes caused by chemical shifting and frequency changes generated by a gradient magnetic fields; the signals from the fat will be misregistered to an incorrect position. The displacement of fat and water signals appears in the MR images as bright and

dark boundaries perpendicular to the readout direction along the interface between tissues differing significantly in water and fat contents (for example, eye orbits in the stereotactic radiosurgery).

The magnitude of chemical shifting artifacts is directly proportional to the field strength and inversely proportional to the strength of the readout gradient. The magnitude of the gradient magnetic fields is set to 10 mT/m in the Magnetom™ SP4000 MR scanner. This higher strength of the gradient magnetic fields requires an increased receiver bandwidth, thus picking up more noise. Although not so important in intracranial imaging, the chemical shift artifacts are important at the fat/water interface. The fat protons precess more slowly than the water protons in the same plane. The signal for the fat protons then may be misregistered to an incorrect location. However, the chemical shift artifacts are clinically irrelevant, since the lipid (myelin) signal intensity from the brain is negligible to that from water. Therefore, the chemical shifting artifacts can not be a significant factor.

Stereotactic Head Ring Artifact

As reviewed in the previous chapter, the misregistartion occurs up to five pixels in the lateral coordinate. This

misregistration might be increased in the regions close the stereotactic frame. The misregistration might be caused by two mechanisms: (1) the frame directly disturbs the gradient magnetic field, thus introducing the spatial distortion and (2) the frame disturbs the magnetic field around the rods of the MR localizer, thus distorting the rod positions which causes the misregistration in the axial coordinate [Wis88] [You89] [Xu90] [Pri90].

Even though an aluminum alloy was used to minimize the artifacts due to the stereotactic frame, there should further investigation regarding to the spatial distortion which might be introduced by the stereotactic frame. In order to do that, the specially designed 3D phantom should be used to analyze the spatial distortion in three dimensions. Also, a calibration phantom might be needed to collect the information about the spatial distortion, specially in the peripheral regions (where the rods of the MR localizer are). This information is retrieved when the MR images are registered for the radiosurgery treatment. This procedure should be done whenever the MR scanner is shimmed or calibrated.

Conclusion for Correspondence

According to the previous investigation, the spatial

differences between the CT and the MR images occur in the lateral plane, where frequency encoding is used to excite the proton molecules in the brain. Generally, chemical shifts occur along the frequency axis. Our investigation follows the general theory about chemical shift artifacts. Also, the spatial distortion seems to be limited in the AP or the lateral plane rather than the trans-axial plane assuming that the 3 mm or 5 mm slice thickness does not introduce any spatial distortion in the trans-axial coordinates.

Another explanations for smaller spatial distortion would have to do with the magnitude of the gradient magnetic fields, that is, 10 mT/m. Generally, the higher the gradient magnetic fields, the less the spatial distortion caused by chemical shifting artifacts. The gradient magnetic field of 10 mT/m is the maximum magnitude available with the Siemens Magnetom™ SP4000. The overall spatial distortions are about 1.0 mm to 2.0 mm, except in a few cases.

CHAPTER 8
REGISTRATION OF MR IMAGES

Introduction

Current techniques to register MR images were briefly mentioned in chapter 2. The correlation analysis with a water phantom and with stereotactic patients were discussed in the previous chapters. The source of the correlation errors more than 1mm are frame artifacts, susceptibility artifacts, chemical shifting artifacts, motion artifacts and image registration procedures [Cal91] [Dix88]. In this chapter, only the image registration procedure is discussed. The image registration procedure is, in the literature, frequently called coordinate determination procedure. Because of spatial distortion in the MR scanner, the MR image registration is not as straightforward as in the CT image registration. In this chapter, the MR image registration procedure which is based upon statistical distribution of the pixel values in the localization rods and "overall registration" rather than slice-by-slice registration is introduced [Huh92] [Pra78].

The MR image registration procedure is currently carried out by using the fixed threshold value (called global

thresholding) specified in the reference image by a user. The registration procedure is carried out automatically based upon the rod position in the previous image. The automatic rod detection procedure very often needs user intervention when the pixel value in a localization rod is smaller than previous images. This situation occurs when the birdcage resonator is mis-tuned because of asymmetric loading from the patient head. This technique has two problems: (1) the registration procedure depends upon the threshold value and (2) it also depends upon random and structured noises (for example, external noises like RF interference). In order to accurately register the MR images, adaptive thresholding technique should be employed. The adaptive thresholding technique is proposed to use the histogram of the noise in the background and of the rod region, where the rod is found. In most publications, the rod detection procedure is not mentioned at all, even though the rods in the MR images are not well defined.

Once all rods in each slice are found, each MR slice image is registered in the BRW coordinates. When the spatial information is not complete, an overall registration procedure might be useful to get rid of the spatial distortion in each slice, with the assumption that the slice thickness is known accurately. This procedure is called global registration. Obviously, this procedure should be verified using the 3D phantom which has landmarks with known locations.

The overall registration procedure will be used with the MR water phantom to demonstrate the possible usefulness of the new procedure. According to the literature survey, the coordinate determination [Kon88] [Kon92] provides the same function as the global registration procedure.

Review of Global Thresholding Technique

In order to review the thresholding technique, the water phantom images with T1-weighted MR imaging and the birdcage resonator are used to demonstrate the potential problems. Several threshold values are selected to show the shape of the localization rods from the water phantom. Fig. 8.1 shows the reference images with nine white crosses (which are input by a user) and the red circular shapes indicate the rods which are determined by using the global threshold method [Pra78]. The shapes of the localization rods are distorted by partial volume effects as well as by background noises. Fig. 8.2 shows processed rod images by using the adaptive thresholding methods (this will be covered in later sections) [Gon87]. The blue crosses indicated the center of each localization rod and the red lines are drawn to demonstrate the accuracy of the rod detection algorithm.

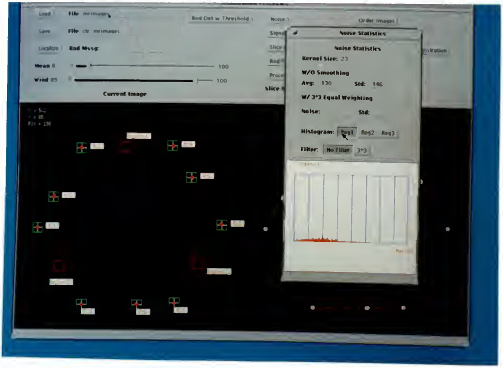

Fig. 8.1 Computer output to demonstrate the rod detection algorithm based upon the global thresholding method. Three regions marked "Region: number" (red square box) are used later to sample the background noise statistics. The red pixels in each rod detection region marked "R:number" represent the pixels larger than the threshold values for each rod. The green box represents the rod region of each rod for the rod detection algorithm.

Fig. 8.2 Rods found by using the adaptive thresholding techniques. The blue crosses indicate the center coordinates and the red line shows the accuracy of the rod detection procedure by connecting three rods: two axially oriented rods and one slanting rod.

In order to illustrate the global thresholding technique graphically, one MR slice image is used to indicate the potential problem which the global threshold technique might introduce during the rod detection procedure. In Fig. 8.3, each row in the figure shows nine localization rods with different threshold values and the number of pixels. The reference image (in which a user indicates initial rod positions) without any image processing (represented by the "No Filter" in the figure) is taken to show one example of the global thresholding in terms of the threshold values and the number of pixels in each rod. The number of pixels represents the number of pixels larger than the global threshold value. Obviously, the number of pixels are decreasing with the threshold values.

The axial coordinate is calculated by using those localization rods which are also dependent upon the threshold value, thus introducing mis-registration. Therefore, there should be a new method which reduces the uncertainty caused by the selection of the threshold values as well as the random fluctuations in the background noises.

The sources of introducing the uncertainty in the detection of the localization rods are patient-related effects, like asymmetric loading to the birdcage resonator, motion artifacts or external RF interference. These factors

Fig. 8.3 Localization rods with the global thresholding. In each row, the shapes and pixel numbers of nine localization rods are shown with threshold value for each row. In the last row, threshold value (starting with T:) used is 676 and the pixel numbers in each rod with the threshold value of 676 range from 39 to 51.

should be considered in the rod detection procedure to reduce the uncertainty of mis-registration of the MR images.

Registration Procedure

In the registration proposed in this chapter, the MR image registration procedure consists of two steps: (1) detect the localization rods with the use of a histogram and (2) register all the MR images with BRW coordinates at the same time. The localization rod detection is carried out by selecting a threshold value from a gray-level histogram. The threshold value is used to segment two regions: rod and background.

There are two steps to register the MR images: (1) rod detection procedure to process each localization rod accurately and (2) overall registration procedure to determine BRW coordinates of all MR images.

Rod Detection Procedure

A user indicates nine rod positions in the reference MR images (see Fig. 8.1). Because of the interaction between the birdcage head coil resonator and a patient, the distributions of the pixel values in the rods are not fixed for every clinical situation. According to the past six month

experience with the MR images of stereotactic patients or epilepsy patients at the University of Florida, the pixel values of the localization rods are not fixed like those of CT images. For example, the pixel values of rod number 4 are smaller than those of other localization rods (see Tables 6.2 and 6.3). In order to take care of this situation, different threshold values for different localization rods are determined for each slice.

The histogram of the rod region (47 pixel-by-47 pixel) is investigated before the adaptive threshold technique is introduced [Gon87] [Bal82]. Two regions (see Fig. 8.1 for the regions 1 and 3) are chosen to show their histograms as well as the statistical characteristics (average and one standard deviation) in Fig. 8.4. With the proper kernel size, the noise characteristics are very predictable. This kernel size is experimentally found by examining the fluctuation of the standard deviations in terms of kernel size. The relationship between the window size and the statistical fluctuation such as average and standard deviation is summarized in the Appendix C.

A threshold value for each rod is determined by considering a histogram sampled in three places between two rods and the pixel value specified by a user. The smoothing filter with 3*3 pixel kernel is applied to the rod regions,

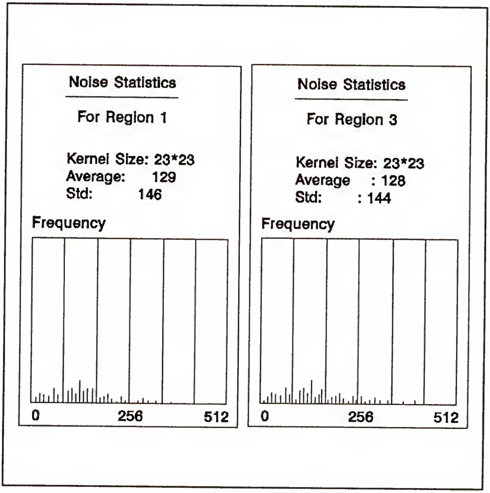

Fig. 8.4 Histograms of region 1 and 3 in the noise regions defined in Fig. 8.1. The maximum pixel values are set to 512. The average and standard deviation (STD) of two regions are average 128 with STD 145 and average 130 with STD 146. Without image processing, the standard deviation is on the order of the average values in the noise regions.

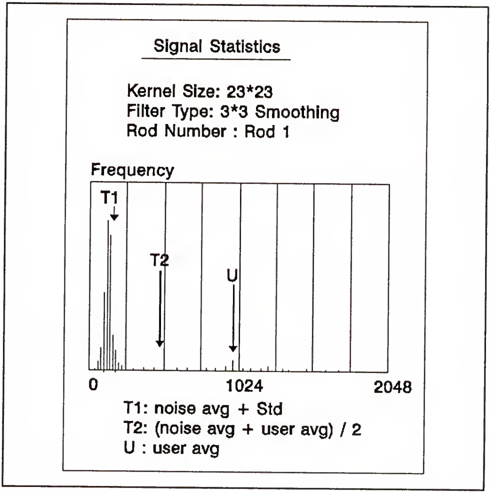

Fig. 8.5 Histogram of the rod region, where two regions are placed: the background noise and the rod. The maximum pixel values are set to 2048. The histogram is represented by red areas and T1 and T2 represent the threshold values. The T1 is the value defined by the average values plus one standard deviation of three noise regions with 3*3 smoothing filter. The T2 is the middle value between the noise average and the average value of the user-indicated point with 3*3 smoothing filter. The pixel distribution of the background noise is smaller than without filtering.

which are indicated by the red crosses in Fig. 8.1. The histogram of rod 1 (see Fig. 8.1 for the rod region indicated by R:1) is shown in Fig. 8.5.

A typical histogram has two peaks due to the background and the rod. The region segmentation is carried by setting the proper threshold value based upon the pixel distribution in the region, where each rod is placed with additive random noises. The thresholded images can be carried out by defining the threshold T,

$$f(x,y) = 1 \quad \text{if } g(x,y) > T \qquad \text{Eq. 8.1}$$
$$f(x,y) = 0 \quad \text{if } g(x,y) < T$$

where the f(x,y) is the binary image to segment the rod from the background and the g(x,y) is the gray-level images. Once the f(x,y) is determined, the geometric center (GC) of the segmented pixels is employed to calculate the center of each rod.

Slice-by-Slice Registration Procedure

In order to register MR images, each image should be processed. Generally, the MR images are not sequentially ordered when the MR images are electronically sent to the computer. Therefore, two steps of MR image registrations

are necessary: (1) order MR image and (2) registration. The reason two steps are needed is that the threshold values of the previous slice are used to determine the threshold values of the current slice image.

The ordering procedure is not necessarily accurate, therefore the threshold value defined by T1 (shown in Fig. 8.5), thus involving more pixels to locate the rod. The lower threshold value can reduce the possibility to locate the potential rod in the current image even though the rod information in the previous image is used. The lower threshold value is used during the ordering procedure.

Once all MR images are ordered, the fine registration procedure is carried out to calculate the axial coordinates. Even though the lower threshold is used, the coordinate of each rod is very close to that obtained by using the fine registration procedure. The most important step is to determine the threshold value from two parameters: the average of the noise values and the average pixel values of the center of the rod. The initial threshold value is the average value of two average values which are the average pixel values of the rod and the noise. The lowest threshold value is the average of the noise region plus one standard deviation of the noise region. The flow chart of estimating

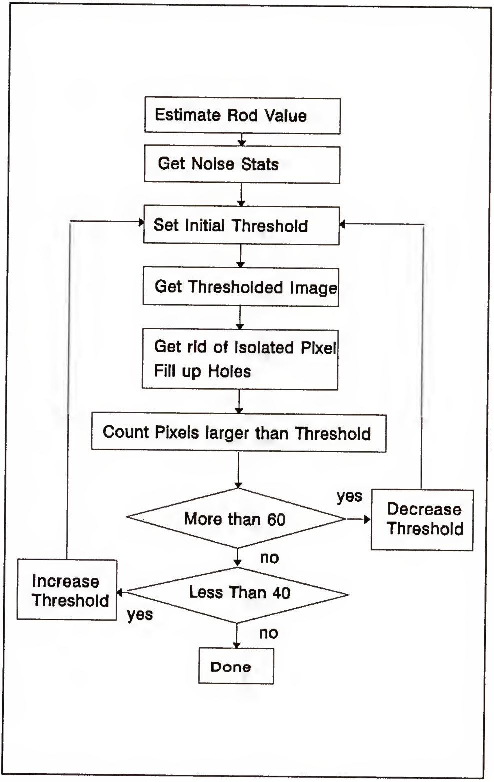

Fig. 8.6 Flow chart for rod detection

the coordinates of the rod is described in Fig. 8.6. A detailed explanation will be given in the next paragraphs.

The threshold value is set by two values: rod value and the average and standard deviation of the noise regions in the current slice image. The rod value is the average pixel value of the 3 pixel-by-3 pixel region of the coordinates of the rod region in the previous slice. The rod value is assumed to be the average pixel value in the rod region. Three noise regions (see Fig. 8.1) are used to calculate the average and standard deviation of the noise regions.

The initial threshold is set to the average of two average pixel values: the rod value and the noise average. The threshold is decreased or increased depending upon the number of pixels in the rod regions. The number of pixels in the straight rods are 40 to 60 because of the partial volume effects. Once the threshold value is determined, the thresholded image (consisting of one's and zero's) is obtained using Eq. 8.1. When the SNR is low (for example, T2-weighted image), the thresholded image has many holes and there are many isolated pixels (representing a one in the thresholded image). The isolated pixel should be removed and the holes should be included. This filling or removing procedure should be included in the iterative procedure.

The pixels of each rod are counted in each loop. If the number of pixels are larger than 60 or smaller than 40, the threshold value is adjusted. This procedure is done for nine localization rods.

Overall Registration Procedure

Once the coordinates of the localization rods in all the slices are obtained, a 3D linear fitting function is carried out for a rod over three or five slices. This procedure is done for all nine localization rods. In order to use the 3D linear fitting function, the slice thickness is fixed (3mm or 5mm). The rod should be straight in the sagittal plane even though a curved rod is very possible because of the nonlinear magnetic fields or the frame artifacts.

As mentioned earlier, the slice-by-slice registration is not accurate because of the nonlinear features introduced by the MR scanner as well as the stereotactic frame. Therefore, overall registration based on minimization of the least-square mis-match can be useful. The overall mismatch can be represented by the following equation:

$$\text{Minimize} \sum_{i=1}^{i=N} \left(\left[\left(\frac{\bar{q}}{Q}\right)-0.5\right] \cdot H - (z_0 + S \cdot i) \right)^2 \qquad Eq.8.2$$

where H is height of the MR localizer (190 mm),

(q/Q) is defined in Fig. 2.2,

z_0 is BRW Z-coordinate of the first slice,

N is the Nth number of the MR images (usually 14)

S is the slice thickness (3 mm or 5 mm)

From the rod detection procedure, the average value of (q/Q) in each slice is determined. The unknown variable is the z_0, the z-coordinates of the first slice in BRW coordinates. Eq. 8.2 can be solved by using differentiation with respect to the variable z_0. Once the z_0 is determined, all the MR images can be registered at the same time.

Conclusion

In this chapter, overall registration is proposed to minimize the possible sources of mis-registration using the adaptive thresholding technique, which adjusts the threshold value based upon the pixel values of the detected rods and the background noise. The procedure to get rid of isolated pixels in the background (not part of a rod) as well as filling procedure within the rod is not explicitly described

in this chapter. This procedure should be included when the threshold values are updated in the iterative procedure.

The final comment about the new registration procedure is that the verification procedure should be carried with a specially-built phantom. The nonlinearity of the gradient magnetic fields might be predicted from the phantom test. However, the frame artifacts should be carefully investigated.

CHAPTER 9
DIGITAL RADIOGRAPHY

Introduction

Conventional biplane angiography utilizing cut film has been used for stereotactic localization of AVM patients at the University of Florida. The UF procedure calls for the centers of the fiducial markers in the AP and lateral films to be digitized. Target boundaries are identified on both films and traced using the same digitizing technique. Because of the high resolution of conventional cut film angiography, a high level of spatial accuracy can be achieved (0.3 mm) [Sid87] [Bov91] [Fri89].

There are many advantages of using the digital radiography. The major advantage is the possibility to directly use digital subtraction angiography (DSA), thus enhancing the low contrast blood vessels. The digital system is controlled electronically, therefore eliminating the timing delay during image acquisition procedure mentioned in chapter 2. The images are stored in the computer, which makes it easy to manipulate the images with various processing techniques, for example, to enhance the structures of the small arteries

or veins. Also, images from the digital angiography could be integrated with images from other imaging modalities such as CT and MR to give physicians more anatomical information.

The disadvantage of digital radiography is that the digital images are distorted by the image intensifier or the TV tube chain (see chapter 3). The most pronounced feature is spatial distortion called pincushion distortion and nonuniformity (or shading). The detailed explanations about these sources are well described in the literatures [Boo91] [Cas76]. This distortion is not acceptable with the stereotactic radiosurgery system (see Appendix D). Therefore, a correction (or unwarping) procedure should be included to accurately register the fiducial markers as well as the target information (target size and target center coordinates).

In order to verify the accuracy of the correction algorithm, a special phantom was fabricated. This was termed "the angio target phantom". Since spatial distortions are space-dependent in digital angiography, an angio target phantom should have various targets. The various targets should be able to be identified very accurately in order to examine the accuracy of the correction algorithm. The target identification procedure can be carried out by using the current angio localization procedure. The procedure should be repeated several times to minimize user-dependent errors

because of uncertainty in defining the fiducial markers and the target position [Sid89]. This verification procedure or the accuracy of the correction algorithm has not been reported in recent literature surveys.

Our approach to correct the geometric distortion of digital radiography within reasonably accuracy (on the order of one pixel) is to use the grid plate, which contains orthogonal patterns of 2 mm-diameter stainless steel wire with 2cm gaps between the wires on a Plexiglass™ plate. There are two methods to use the grid plate: (1) the grid plate is placed on the image intensifier and used during the entire scanning procedure and (2) the grid plate is used during the acquisition of the calibration images and removed during the patient scanning procedure. The first has the potential of introducing uncertainty in locating the fiducial markers, especially when smaller magnification factors (fiducial markers in the plate close to the image intensifier) are used. It is a time-consuming procedure to avoid overlapping problems even when the phantom is positioned under fluoroscopic control: (1) between fiducial markers and grid patterns and (2) between BRW head ring and grid patterns for lateral view. Also, another difficulty of using the first method is that some residual artifacts due to the grid patterns can potentially show up when two images are subtracted to get DSA images.

The second method is chosen for an experimental setup. This setup will be used for the unwarping procedure. The disadvantage of using this method is that one more image called "the calibration image" is needed for unwarping algorithm. An advantage is that the calibration image will be retrieved and can used to unwarp an angio image once it is stored. This procedure should guarantee that there are no changes in the angiography unit. For example, the calibration images should be updated whenever the angiography unit is re-calibrated or image acquisition parameters, which effects image chain parameter, are altered.

In this chapter, the experimental setup, the grid plate design, the target phantom, the unwarping algorithm and the accuracy of the unwarping algorithm compared with that of the biplane film angiography will be discussed.

Experimental Setup for Phantom Test

The Angiorex™ Fluoroscopy Unit (biplane digital radiographic scanner with 30 cm-diameter image intensifier, DFP-65A Model by Toshiba) was used to develop the unwarping algorithm with the angio localizer. A standard head imaging technique (120 KVp, 100 mA) was used to scan the target phantom with the angio localizer and the above mentioned grid plate with 2 cm-thick solid water phantom. The grid plate was

taped onto the image intensifier and the solid water phantom was setup at the isocenter of the digital radiographic unit. The source-to-film distance (SFD) and the source-to-image intensifier distance (SID) were 100 cm and 105 cm, respectively. The target phantom was placed at the isocenter so the magnification factor was approximately 1.2 to 1.4.

The grid plate was constructed using the Plexiglass™ and is shown in Fig. 9.1. The base plate is 6 mm-thick, 30 cm square Plexiglass™ plate (which fully covers the 30 cm-diameter image-intensifier) with the 1 mm-diameter stainless wires inserted in the grooves on both sides of the plate.

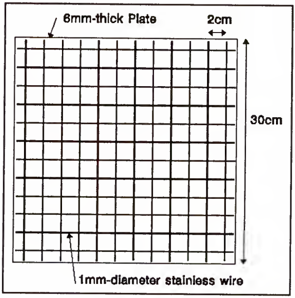

Fig. 9.1 Schematic diagram of the grid plate

The target phantom consists of two plates: the target phantom base and the target plate. The target phantom base has a groove in which the BRW head ring is rigidly placed and several holes with 30 degree increments which are used to rotate the target plate. The target plate contains ten targets (each target is a 6 mm-diameter aluminum ball) mounted on a 9 mm-thick Plexiglass™ plate. The target plate can be rotated in steps of thirty degrees. Therefore, the spatial distortion in a 15cm-diameter and 13cm-height volume can be tested. The target phantom is shown in Fig. 9.2.

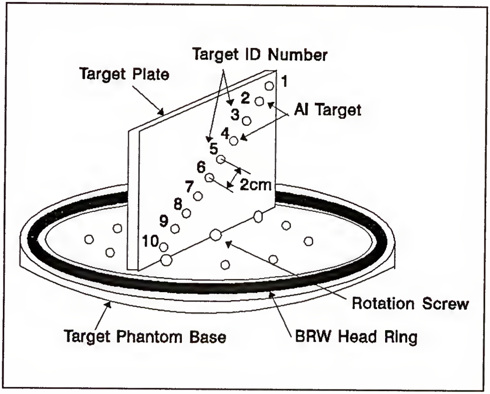

Figure 9.2 Schematic Diagram of the Digital Angio Target Phantom with BRW Head Ring

The digital angio (DA) target phantom with angio localizer and the grid plate are used to develop an unwarping procedure. The grid plate is securely taped onto the surface of the image intensifier. Film images and digital angiographic image are taken using a standard angiographic localization procedure and a standard head scanning technique. Those two images are shown in Fig. 9.3 and the digital angio image shows the typical pincushion distortions.

DA Target Phantom Information

Two angiographic plane films are taken for the AP and the lateral planes with the digital angio target phantom using the Toshiba angiographic unit. User-defined center (UC) was employed to define the center of each target even though the geometric center (GC) is frequently used for the AVM boundary [Fri90]. It is much easier to use the UC than GC because of the circular shapes of the aluminum targets on both films. By using the UC of the spherical aluminum targets, the target coordinates are determined and shown in Table 9.1. The skew values of the center coordinates of ten sphreical targets vary from approximately 0.12 to 0.86 mm. The large skew value of the targets in the boundar is related to unsymmetrical magnification of the spherical target in the AP and lateral images.

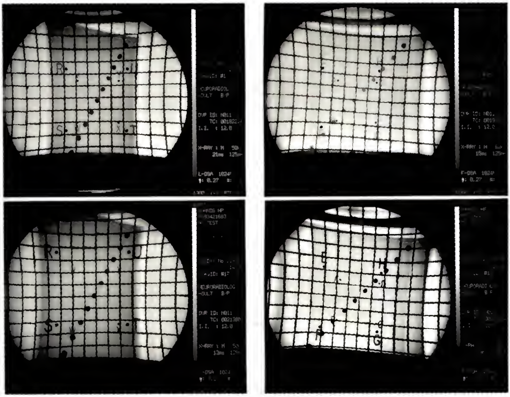

Figure 9.3 Typical Film image (left) and Digital angiographic Image (right) to illustrate Spatial Distortion. The right figure conceptually shows typical pincushion distortion. The actual images are shown in later pictures. The source of the spatial distortion is the nonlinearity of the image intensifier, TV camera, and external magnetic fields. The spatial distortion includes the pincushion distortion and S-type distortion.

Table 9.1 Target Coordinates and Skew Distance.

No	AP +/- Std	Lat +/- Std	Ax +/- Std	Sk +/- Std
1	+35.59+/-0.07	-61.45+/-0.04	+71.30+/-0.07	0.86+/-0.10
2	+28.37+/-0.06	-49.14+/-0.05	+56.95+/-0.05	0.60+/-0.08
3	+21.19+/-0.05	-36.95+/-0.04	+42.67+/-0.03	0.36+/-0.06
4	+14.15+/-0.02	-24.66+/-0.06	+28.56+/-0.02	0.21+/-0.03
6	+7.19+/-0.04	-12.22+/-0.04	+14.27+/-0.03	0.13+/-0.01
6	+0.10+/-0.04	-0.01+/-0.06	+0.06+/-0.04	0.12+/-0.02
7	-6.61+/-0.06	+12.37+/-0.05	-14.00+/-0.02	0.17+/-0.05
8	-13.54+/-0.03	+24.62+/-0.05	-28.14+/-0.04	0.23+/-0.06
9	-20.53+/-0.05	+36.93+/-0.03	-42.68+/-0.05	0.36+/-0.08
10	-27.39+/-0.05	+49.40+/-0.03	-56.25+/-0.07	0.76+/-0.09

Note: Std means one standard deviation with ten measurements. AP, Lat, Ax and Sk represents anterior-posterior, lateral, axial coordinates and skew distance in mm in the stereotactic coordinates.

Unwarping Algorithm

An eight step unwarping procedure is used to investigate the accuracy of the unwarping algorithm: (1) area-of-interest (AOI) definition for unwarping operation, (2) define four corners, (3) grid detection, (4) bilinear mapping, (5) detect

fiducial marker detection, (6) target definition, (7) projective geometry and (8) verification. The definition of four corners, fiducial marker detection and the target definition need the following user intervention: (1) define the AOI of each view, (2) define four corners (or crosses) for automatic grid detection, (3) indicate starting points for eight fiducial marker and (4) indicate starting points for ten target definition detection procedure. The overall schematic diagram for the unwarping procedure is shown in Fig. 9.4. In this section, each procedure will be described.

Two types of images are used in this procedure: (1) calibration image and (2) target phantom image. The purpose of the unwarping algorithm is to remove the spatial distortion in the target phantom image (which is the actual patient image in the clinical situation or the target phantom image in the algorithm testing procedure) based upon the information of the spatial distortion in the calibration image. The calibration image is used to determine the coefficients of piecewise bilinear mapping functions, which are used to unwarp the target phantom image. If the calibration image is not used during the angiographic examination, the target phantom image should be used to determine the coefficients of the bilinear mapping functions and the AOI. Two methods (with and without calibration image) are also possible to unwarp the warped image. These two methods are conceptually shown in Fig. 9.5.

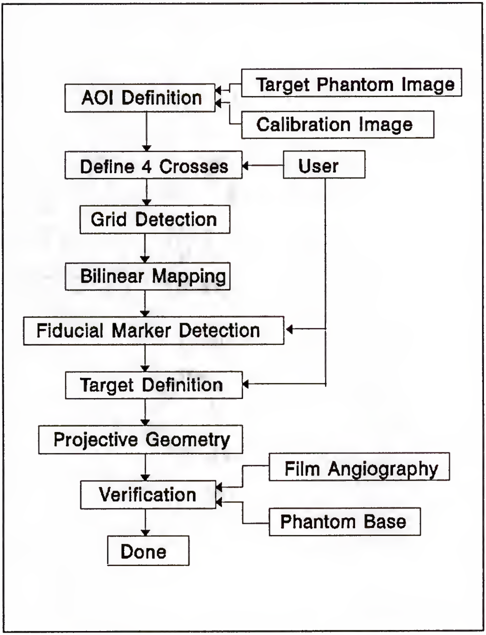

Fig. 9.4 Flowchart of Unwarping Procedure
Two images are used to unwarp the warped image: calibration image and target phantom image (or warped image). In this dissertation, the calibration and the target phantom images are used to correct spatial distortion.

AOI Definition

Typical digital angiographic images are represented by 1024 pixels-by- 1024 pixels matrix and approximately 75 percent of the matrix is used to represent the images. Thus, a middle portion of the digital radiographic images is chosen. The regions should include eight fiducial markers in each plane (even though six fiducial markers are enough when there is accurate location of the six fiducial markers) [Sid87]. In the computer program, the AOI selection procedure is carried out using the horizontal and vertical scroll bars, which are attached to the displayed canvas. This process is shown in Fig. 9.6. The right canvas is scrolled horizontally or vertically to define the AOI so that ten targets and eight fiducial markers are included. The corresponding portion of the AOI images in the left canvas is utilized to determine the spatial transformation.

Define 4 Crosses

In order to reduce the processing time of the cross detection algorithm, 4 crosses in the upper left portion of the image are indicated by a user. The cross detection algorithm is used to define the center coordinates of each cross and fill up a buffer called "accumulator". The maximum number of crosses are set to 32 by 32, which is determined by

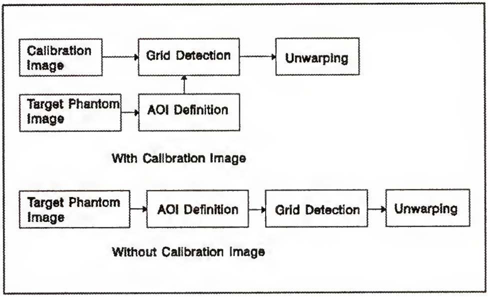

Fig. 9.5 Two Unwarping Procedures
With a calibration image two images are utilized to define the AOI and the grid patterns. The target phantom image is used to select the AOI and the corresponding portion in the calibration image is used to define the grid patterns. Without a calibration image, the target phantom image only is used to define the AOI and the grid patterns. This approach might cause difficulty detecting some grid patterns which overlap with the BRW head ring. However, this portion of the image is not clinically useful to define the fiducial markers as well as the target. It is still possible to estimate the grid patterns in this region utilizing the neighbor crosses.

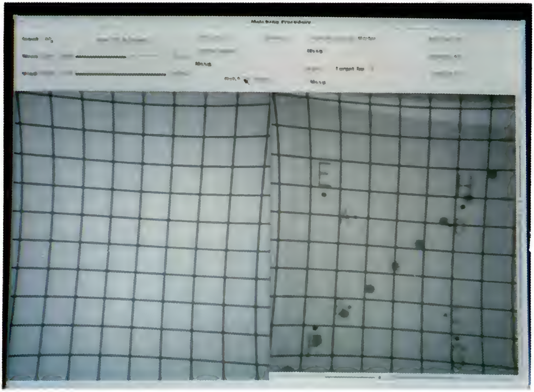

Fig. 9.6 AOI Image and Calibration Image
The image in the right canvas is reviewed and the AOI is defined by using two scrollbars attached onto the right canvas. The AOI image in the right canvas should include eight fiducial markers as well as ten targets. The left canvas includes the corresponding AOI image of the calibration image. The AOI image of the calibration image is used to determine grid patterns and a mapping function. This procedure is carried out in the AP and lateral views, respectively.

the number of grid patterns. Each cross contains two lines (vertical and horizontal lines) and center coordinates of the cross in the data structure for a cross shown in Table 9.2. The center coordinates are obtained by solving two line equations. Each line is represented by two variables: a slope and an intersection on the arbitrary coordinates.

Once the four crosses are indicated by a user, the cross detection algorithm starts to fill up the buffer for each cross. In order to create some margins to find the cross, the search region for the possible cross is set to +/- 10 pixels. This size is dependent upon the spacing between the horizontal and the vertical lines in the grid plate. If the spacing is smaller, the search region should be smaller in order to give some margins between two crosses. The ranges of the slope and the intersection of the horizontal and the vertical line are experimentally determined by the characteristics of the pincushion distortion by using the angio target phantom and a human skull phantom and various combinations of solid water phantom. The following heuristic knowledge is found and utilized to develop the cross detection algorithm:

(1) The horizontal line and the vertical line are distinguished by the slope of each line, thus setting the slope within -1/2 to 1/2 for the horizontal line. There are some margins between the two lines. The schematic diagram to determine the vertical and horizontal lines with B=0 is shown

Table 9.2 Data Structure for Crosses

```
struct line {
     int intersection;
     int slope;
};

struct coord {
     float x;
     float y;
};

struct cross_database {
     struct line horizontal_line;
     struct line vertical_line;
     struct coord center;
};

struct cross_database ap_cross[32][32], lat_cross[32][32];
```

in Fig. 9.7. The horizontal and vertical lines with B=-10, B=0 and +10 are shown in Fig. 9.8.

(2) Instead of using the image coordinate, the user-indicated location is used as the origin of the search region to define the intersection of two lines in the cross search region. The O in Fig. 9.7 and Fig. 9.8 is indicated by a user for the initial four crosses.

(3) The vertical and horizontal lines are assumed to be linear over the cross search region (see Fig. 9.7 and 9.8). This assumption is based upon experimental examination. This assumption is easily satisfied with the typical experimental setups or the clinical situations during the angiographic examinations. If this condition is not satisfied, the grid plate should have smaller spacing between the grid patterns or

a higher-order fitting function to accurately represent the grid patterns should be utilized.

Once the slopes and the intersections of the vertical and the horizontal lines are determined, the center coordinates of the 4 crosses are calculated by solving two linear equations. The horizontal equation can be represented by an equation: Y = A*X + B, where A is the slope and B is the intersection of the horizontal line. The A and B determine the search region from the user-indicated location. The A is limited from -1/2 to +1/2 and the B varies from -10 to +10. In order to avoid the divide-by-zero situation for the vertical line, the equation is represented by X = A*Y + B. The A and B have the same range as the horizontal lines.

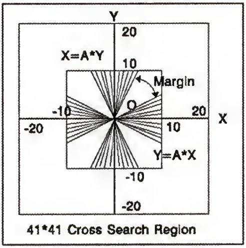

Fig. 9.7 Definition of Horizontal and Vertical Line of Cross B is set to zero for illustrating the possible lines for the horizontal and vertical lines. The margin between the horizontal and vertical lines is set experimentally from the typical clinical situation. O is the origin of the cross search region.

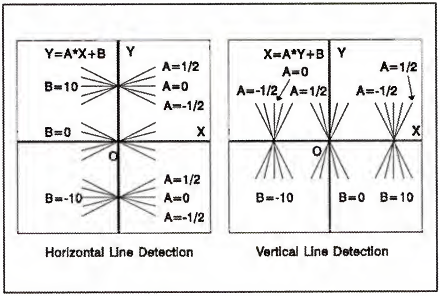

Fig. 9.8 Horizontal and Vertical Line Detection Algorithm O represents the origin of the search region and also the location which a user indicates using the mouse. In both figures, the B is set to -10, 0 and 10 for the illustration of the possible ranges to define the lines.

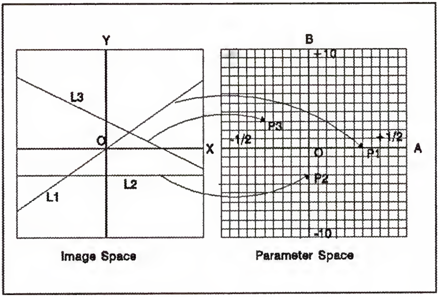

Fig. 9.9 The Relationship between Image Space and the Parameter Space. A line L_i in the image space is mapped to a discreet point P_i in the parameter space. The parameter space is quantized into discreet coordinates. For a line, A ranges from -1/2 to +1/2 and B ranges -10 to +10.

The lines are mapped to the parameter space consisting of A and B. The mapping relationship is shown in Fig. 9.9 in the parameter space. The parameters A and B are quantized into discreet value. The sub-pixel representation will bedescribed later to improve the accuracy of the cross detection algorithm. The pixel values along the lines are added and stored in the buffer called "accumulator" in the parameter space. The combination of the A and B, giving the minimum pixel values in the buffer, are selected to represent the vertical and the horizontal line.

Once the A and the B are determined, the center coordinates of a cross is calculated by solving two linear equations: $Y=A_1*X+B_1$ and $X=A_2*Y+B_2$. Since the A_i and B_i values are quantized, the center coordinates are also quantized, thus limiting the accuracy of the grid detection algorithm. This cross detection algorithm is repetitively used to detect all initial four crosses in the image. Once the four are determined, the grid detection algorithm is carried out to define the remaining crosses in the area of interest.

<u>Grid Detection Algorithm</u>

Once the initial crosses are found, the grid pattern (or crosses) are defined automatically. Instead of finding all vertical and horizontal lines at the same time using Radon

[Rei92] or Hough Transformation [Bal82] [Gon87], all crosses are determined by using the previously determined four crosses. The line detection algorithm mentioned in the earlier section is used to define the horizontal and vertical lines in the AOI images.

The grid detection algorithm is implemented automatically utilizing the previously determined crosses. The grid detection algorithm consists of five different procedures to estimate the next crosses: (1) the crosses in the first row, (2) the crosses in the first column and (3) the crosses in the first column, (4) the crosses in the second column and (5) all remaining crosses except the first and second rows and the first and second columns.

The grid detection algorithm is represented in the flowchart shown in Fig. 9.10. The grid detection algorithm is modified depending upon the cross position in the AOI. The crosses in the first row are determined by using two previously found crosses. The estimated position of the next cross is found by extrapolating from the center position of the left cross with the distance between two crosses. This procedure is shown in Fig. 9.11.

The crosses in the second row are estimated using the slope of the vertical lines of the cross in the first row and

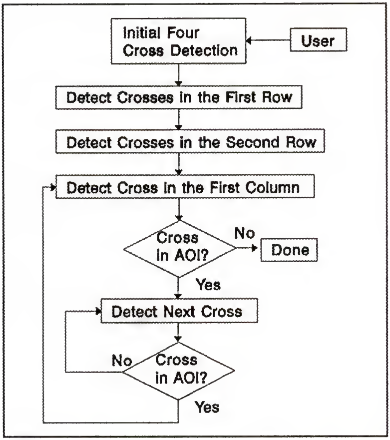

Fig. 9.10 Flowchart for the Grid Detection Procedure
Initial four crosses are indicated by a user. The crosses in the first rows and the first column are determined by a previous crosses to estimate the locations of the next crosses. The estimation procedure for the crosses in the first column and the first row is shown in Fig. 9.11. The crosses in the middle portion of the AOI images are estimated by using the information of the four neighbor crosses. The estimation procedure is pictorially shown in Fig. 9.12.

the slope of the left cross. This procedure is shown in Fig. 9.12. The cross in the first column and the second column are determined by using the same concept as used in the first rand the second row. The crosses in the middle portion of the image are determined by using the line information of the left two crosses and the upper two crosses, thus estimating the

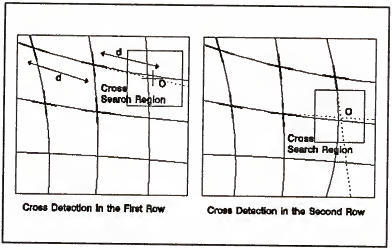

Fig. 9.11 Grid Detection Procedure in the First and Second Row. The thick lines represent the horizontal and vertical lines which are previously determined using the cross detection procedure based upon the user-indicated positions. The dotted line represent the extrapolated line from the previously determined crosses. In the left figure, the extrapolation line is solely determined by using the slope of the horizontal line and the distance between two center coordinates of two crosses. In the right figure, the extrapolation is carried out to estimate the crosses in the second row. The extrapolated lines from the neighbor crosses are chosen and estimate the origin of the cross search region.

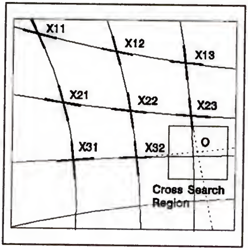

Fig. 9.12 Grid Detection Algorithm in the Middle Portion The crosses in the first and second rows (X_{1i} and X_{2i}) and the fist and second column (X_{i1} and X_{2i}) are found previously. The origin of the cross search region is determined by finding the intersection of the two dotted interpolated lines.

coordinates of the next cross. This procedure is shown in Fig. 9.12.

There is an exceptional case to apply the cross detection algorithm in the AOI. When the estimated center of the cross search region is in the background, a special procedure should be carried out because the pixel values in the background are all zeroes. This situation might occur when the target (AVM) is placed in the peripheral regions of the head. Four crosses in each rectangle could not be identified. If that occurs, affine transformation should be carried out [Wol92]. This situation is shown in Fig. 9.13.

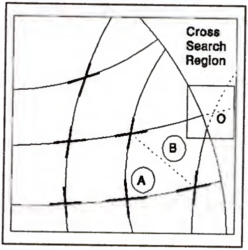

Fig. 9.13 Exceptional Case with Grid Detection Algorithm When the target is located at A in the figure, only three crosses could be used. When it is placed at B, four crosses are needed. The cross in the background should be estimated from neighbor crosses for bilinear transformation.

Unwarping Algorithm

A spatial transformation defines a geometric relationship (called geometric-based transformation) between each point (i.e, each cross) in one image (warped image) and the corresponding point in the image to be unwarped [Sei88] [Gon87] [Pra78]. An unwarped image consists entirely of reference points (very often called control points or landmarks, and called crosses or grid in this dissertation), which are known precisely. The unwarped image is the grid pattern shown in Fig. 9.1 or Fig. 9.14. The warped image is the image which is transformed into the unwarped image using a mapping function. General mapping functions can be represented in two ways: either relating the unwarped coordinate system to the warped coordinate system, or vice versa. Simply, they can be represented as

$$[x, y] = [X(u,v), Y(u,v)] \qquad \text{Eq. 9.1}$$
$$[u, v] = [U(x,y), V(x,y)]$$

where [u,v] refers to the unwarped image coordinate system corresponding to the pixel coordinate [x, y] in the warped images, and the X, Y, U, and V are arbitrary mapping functions that uniquely determine the spatial transformation between two image coordinates (see Fig. 9.14). Since U and V map the warped image to the unwarped image, they are

referred to as forward mapping. Similarly, the X and Y are known as inverse mapping.

Forward Mapping and Inverse Mapping

Forward mapping consists of copying each warped pixel onto the unwarped image at positions determined by the U and V mapping functions. Fig. 9.14 illustrates the mapping relationships between two image coordinates. Each pixel in one image is passed through the spatial transformation (U and V, or X and Y) where it is assigned a new coordinate in another image [Wol92] [Van88] [Sei88] [Boo86a] [Ben91].

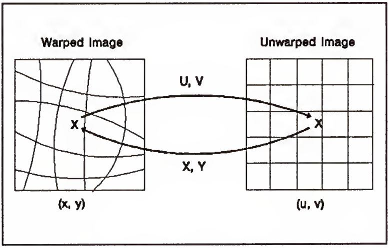

Fig. 9.14 Geometric Transformation between the Warped and Unwarped Image. The coordinates (x,y) and (u,v) are in the warped and unwarped images, respectively. U and V are the forward mapping function to a point in the warped image into a corresponding point in the unwarped image. X and Y are called the inverse mapping, opposite to the mapping of the U and V.

The mapping function called polynomial unwarping function can be implemented without knowledge of the warping mechanism. It is totally based upon locating the crosses (called control points or landmarks) in the warped and unwarped images. In general, the polynomial mapping functions can be represented by Eq. 9.2. The N is called the order of the fitting function. Generally, the order of the fitting function is up to 3 (commonly called spline fitting) or 4 [Pra78] [Gon87].

$$x = \sum_{i=0}^{i=N} \sum_{j=0}^{j=N} A_{ij} u^i v^j \ , \ \ y = \sum_{i=0}^{i=N} \sum_{j=0}^{j=N} B_{ij} u^i v^j \qquad \text{Eq. 9.2}$$

where A_{ij} and B_{ij} are the constant polynomial coefficients. For example, for N=1 (bilinear transformation), the polynomial relationship can be rewritten

$$\begin{aligned} x &= A_{00}+A_{01}*u+A_{10}*v+A_{11}*u*v \\ y &= B_{00}+B_{01}*u+B_{10}*v+B_{11}*u*v \end{aligned} \qquad \text{Eq. 9.3}$$

where the coefficients A_{ij} and B_{ij} are determined by the constraints from the correspondence between a pair of the crosses in the warped and unwarped images. The first-order mapping function (N=1 in Eq. 9.2) is called bilinear mapping function in Eq. 9.3. Four crosses are needed to solve 8 unknown coefficients in Eq. 9.3. This is the minimum condition to solve the bilinear equations (four unknown variables for each mapping function and four crosses).

The procedure to find the unknown coefficients for the case of bilinear mapping functions is described using matrix manipulation in Eq. 9.4 and Fig. 9.15. The exact solution of the linear mapping function can be determined for each cell (which consists of four crosses) since the minimum number of the crosses is four. The constraints for the mapping function look like the following matrix relationship:

$$\begin{vmatrix} x_1 \\ x_2 \\ x_3 \\ x_4 \end{vmatrix} = \begin{vmatrix} 1 & u_1 & v_1 & u_1v_1 \\ 1 & u_2 & v_2 & u_2v_2 \\ 1 & u_3 & v_3 & u_3v_3 \\ 1 & u_4 & v_4 & u_4v_4 \end{vmatrix} \times \begin{vmatrix} A_{00} \\ A_{01} \\ A_{10} \\ A_{11} \end{vmatrix} \qquad \begin{vmatrix} y_1 \\ y_2 \\ y_3 \\ y_4 \end{vmatrix} = \begin{vmatrix} 1 & u_1 & v_1 & u_1v_1 \\ 1 & u_2 & v_2 & u_2v_2 \\ 1 & u_3 & v_3 & u_3v_3 \\ 1 & u_4 & v_4 & u_4v_4 \end{vmatrix} \times \begin{vmatrix} B_{00} \\ B_{01} \\ B_{10} \\ B_{11} \end{vmatrix} \qquad Eq.9.4$$

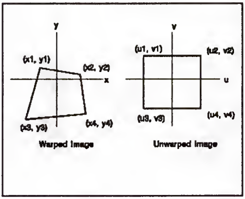

Fig. 9.15 Geometric Relationship between Two Coordinates X_i, Y_i, U_i and V_i are known coordinates for mapping function. X_i and Y_i are determined from the grid detection algorithm and U_i and V_i are known coordinates and can be assigned any arbitrary positions.

Eq. 9.4 can be represented by a simple matrix notations as shown in Eq. 9.5.

$$X = W * A, \qquad Y = W * B \qquad \text{Eq. 9.5}$$

The matrix W can be filled up from the known geometry of the four crosses from the grid patterns. The coefficient matrix A and B can be obtained by using the inverse matrix on both sides as shown in Eq. 9.6.

$$A = W^{-1} * X, \qquad B = W^{-1} * Y \qquad \text{Eq. 9.6}$$

Once the A and B matrix are determined, the spatial transformation can be found. To implement this algorithm, a computer program is written in the C-language, running on the Sun™ Sparc Station 10 with X-window-based graphics. It takes only a few seconds to define all crosses and unwarp the warped images.

In order to examine the cross detection and the unwarping procedure, the calibration image is used to test the cross detection algorithm. In Fig. 9.16 the larger blue cross marks the origin of the cross search region and the smaller red cross marks are the center of the cross determined by the cross detection algorithm. In the right canvas, a Sobel filter is applied to get a gradient image.

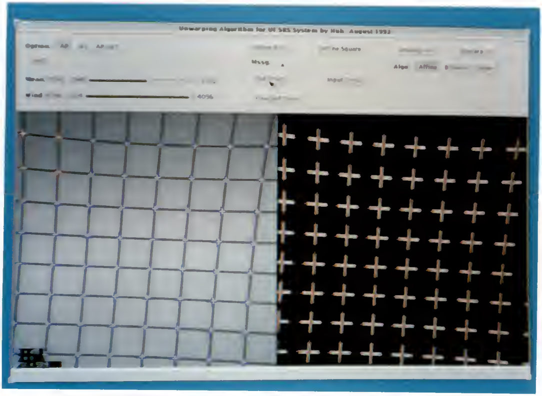

Fig. 9.16 Results of the Grid Detection Procedure
In the left canvas, all the crosses in the area of interest are determined by the cross detection algorithm and the horizontal and vertical lines are drawn on the gradient image, which is obtained by applying the Sobel filter upon the left image.

The gradient image is obtained by applying the filter kernel in Fig. 9.17 and normalized with the maximum value in the window. Each pixel value in the window is quantized into integers 0 to 31. This procedure is shown in Fig. 9.18.

A_1	A_2	A_3
A_4	F_{jk}	A_5
A_6	A_7	A_8

$$F_{jk} = (X^2 + Y^2)^{1/2} \qquad \text{Eq.9.7}$$

where F_{jk} is the pixel value of the gradient image,

A_i is the pixel value in the gray image,

$X = (A_1+2*A_2+A_3) - (A_6+2*A_7+A_8)$ and

$Y = (A_1+2*A_4+A_6) - (A_3+2*A_5+A_8)$.

Fig. 9.17 Numbering for 3*3 Sobel Edge Detection Operator

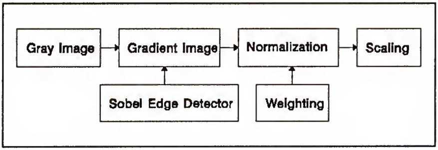

Fig. 9.18 Procedure to Obtain the Gradient Image
The pixel values in the gradient image are normalized by the maximum value in the window and re-scaled into 32 steps for display. The weighting is a useful parameter to enhance the edges in the manual fiducial marker detection procedure.

The "weighting" in Eq. 9.8. and Fig. 9.18 varies from 5 to 100. The weighting is a parameter used to stretch the range of a pixel value in the gradient image. It is termed the "Sobel Weighting" in the manual fiducial marker detection algorithm in Fig. 9.29. It can be manually adjusted to get the optimum edges of a small fiducial marker. Therefore, the pixel values in the gradient image are normalized by the maximum pixel value in the window of the gradient image. In order to display the image in the canvas and to quantize the pixel values, the pixel values are scaled to 0 to 31.

$$G_{jk} = \frac{F_{jk}}{Maximum} \times 31 \times \frac{100}{Weighting} \qquad \text{Eq. 9.8}$$

where F_{jk} is the pixel value obtained by using Eq. 9.7, Maximum is the maximum pixel value in the window and the G_{jk} is the integer value from 0 to 31.

In order to verify the AOI selection procedure, the calibration image and the target phantom image are used. The crosses identified by using the cross detection algorithm are displayed onto the target phantom image in Fig. 9.19. In the left canvas, the markers "+" are displayed to indicate the center coordinates of the crosses in the target phantom image.

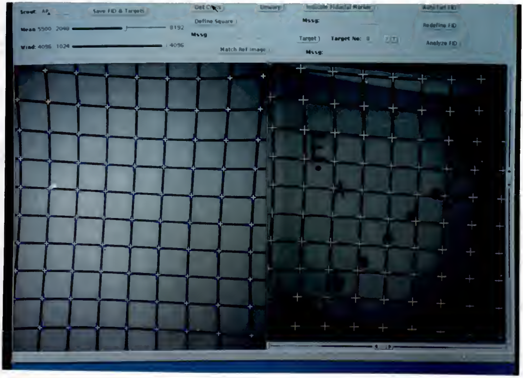

Fig. 9.19 Computer Output for Cross Detection Algorithm
The crosses in the left canvas are determined by the grid detection algorithm by using the calibration image and thus determined crosses are overlapped upon the target phantom image.

The markers are also drawn in the right canvas to verify that two images (the calibration image and the target phantom images) are obtained at the same experimental setup.

The bilinear transformation is carried out by applying the cross detection algorithm on the calibration image. The target phantom image on the right canvas of Fig. 9.20 is unwarped onto the left canvas of Fig. 9.20. The interpolation method used in Fig. 9.20 is the nearest-neighbor interpolation, in which the integer operation is used during the spatial transformation procedure. This integer operation introduce sagged feature in the unwarped image. The procedure to eliminate the sagged feature will be described in the next section using the bilinear interpolation.

Image Resampling Procedure

Image resampling is the process of transforming a sample image from one coordinate to another. The two coordinate systems are related to each other by the mapping function of the spatial transformation, the bilinear mapping function in our case. This permits the unwarped image to be generated by the following simple procedure. The inverse mapping function is applied to the unwarped image sampling grid, projecting it to the warped image. This results in a

Fig. 9.20 Unwarped Image and Warped Image
The warped image in the right canvas is mapped to the left canvas using the spatial transformation using the nearest-neighbor interpolation.

resampling grid, specifying the locations at which the warped image is sampled at these points and the pixel values at these points are assigned to their respective pixels in the unwarped image. This procedure is shown in Fig. 9.21

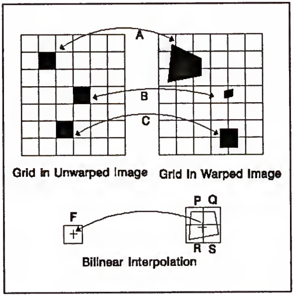

Fig. 9.21 Resampling Procedure for Three Cases. For A, the scale is larger than 1 and for B it is smaller than 1. For C, the scale is 1. When the scale is much larger than 1 or much smaller than 1, special techniques like super-sampling or higher order interpolation should be utilized in order to prevent artifacts due to irregular sampling.

In the clinical situation of the typical radiosurgery procedure, the scale is approximately 1. The bilinear interpolation (called the first-order interpolation) is utilized to resample the grid in the unwarped and the warped images. Four neighbor pixels are used to estimate the pixel

values using the bilinear interpolation shown in Fig. 9.21 and Fig. 9.25. The bilinear interpolation is the same concept used in the later section dealing with the generation of 3X images. Very often zeroth-order interpolation (the nearest neighbor interpolation) is used in the resampling procedure in order to reduce the mathematical complexity. However, it results in sagged features in the edge region because of the truncation process in the integer operation. The unwarped image with the bilinear interpolation using only four neighbor pixels is shown in Fig. 9.22.

Semi-Automatic Fiducial Marker Detection

In biplane film angiography, the fiducial markers are defined by using the magnifier in order to perform the user-defined center (UC) method. Often, the skew distance is larger than 1mm because of human errors in defining the fiducial markers. In digital radiography, the resolution is decreased on the order of one pixel. Therefore, sub-pixel accuracy to detect the fiducial markers is mandatory.

The fiducial marker detection procedure determines the center coordinates and the radius of the circle using the user-specified starting point. The three parameters for each fiducial marker should be accurately determined to

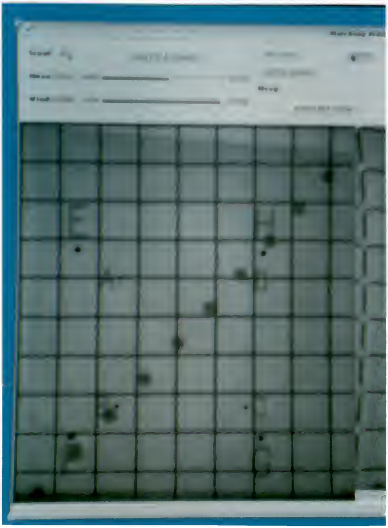

Fig. 9.22 Unwarped Image with Bilinear Transformation using the Bilinear Interpolation

estimate the target position in BRW coordinates. The three parameterare determined by using two different images: gray image and gradient image. Each image is magnified three times using the bilinear mapping function. 3X gray image and 3X gradient image represent the three times magnified image. They are used to estimate the position of the fiducial markers.

In order to represent the procedure in a simple formalism, two parameters are defined as in the following way:

$F(R,X_0,Y_0)$: pixel values along the circumference of the circle radius R divided by a number of pixels along the circumference of the circle center at X_0 and Y_0 in the 3X gradient image

$G(R,X_0,Y_0)$: pixel values along the circumference of the circle radius R divided by a number of pixels along the circumference of the circle center at X_0 and Y_0 in the 3X gray image

These two parameters are used to separately determine the radius and the center position of the fiducial markers in the 3X gradient and the gray image. The example of using the parameter F(R,X0,Y0) to determine the circumference of the circle with radius R is demonstrated in Fig. 9.23.

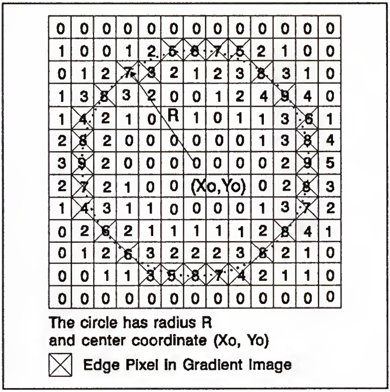

Fig. 9.23. Procedure to Determine $F(R,X_0,Y_0)$
The gradient image is obtained by using the Sobel edge detection filter and $F(R,X_0,Y_0)$ = (5+8+7+5+8+9+6+8+9+8+7+8+8+4+ 7+8+5+3+6+6+4+7+9+8+8+7+3)/28 = 6.5, where 28 is the number of edge pixels represented by the "X" in the pixels.

$F(R,X_0,Y_0)$ is used to determine the radius of the circle with the given center coordinates (X_0,Y_0), which is obtained from using the $G(R,X_0,Y_0)$. $G(R,X_0,Y_0)$ is obtained by applying the same concept as used to determine the $F(R,X_0,Y_0)$ except using the gray image instead of using the gradient image. This parameter is used to determine the center coordinates of the circle with the given radius R, which is determined from the $F(R,X_0,Y_0)$. This procedure is

used to separately determine the two parameters of the circle: radius and center coordinates.

The semi-automatic fiducial marker detection procedure consists of five steps: (1) a user indicates initial locations of the fiducial markers, (2) increase the radius of the fiducial marker (radius determination procedure) with given center coordinate and choose the radius such that $F(R,X_0,Y_0)$ is maximized, (3) change the center coordinates of the fiducial marker (center determination procedure) with given radius and choose the center coordinates of the circle such that $G(R/2,X_0,Y_0)$ is minimized, (4) change the radius of the fiducial marker (radius determination procedure) with the given center coordinates and choose the radius such that $F(R,X_0,Y_0)$ is minimized and (5) termination condition.

Overall procedures are shown in the flowchart in Fig. 9.24. A manual fiducial marker detection procedure (not shown in Fig. 9.24, but shown later in Fig. 9.29) is used as well when the automatic detection does not define the fiducial marker because of overlapping objects onto the fiducial markers. Basically, the manual procedure is the same as the automatic detection procedure except for manually changing the radius and the center coordinates of the fiducial marker by a step size of a half pixel or one pixel.

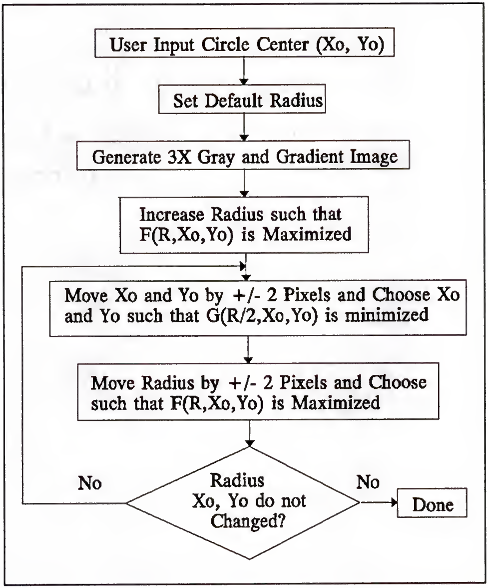

Fig. 9.24 Flow Chart of the Semi-automatic Fiducial Marker Detection Algorithm. All pixel values are rescaled and quantized to 0 to 31 integer values. Manual fiducial marker detection procedure is the same as the automatic fiducial marker detection procedure.

The user indicates the initial locations of eight fiducial markers in each plane. The initial location is assumed to be a center of the fiducial marker with default radius, for example, one pixel-radius (refer to the circle with the radius of R_0 in Fig. 9.26). The region, which includes a fiducial marker, is set to 21-pixel-by-21-pixel, which is large enough to cover the fiducial markers in the typical clinical situation. The region, where the fiducial marker is located, is magnified by three times (called 3X image) using the bilinear interpolation described in Fig. 9.25. The gradient images are generated by using the same Sobel edge detection filter in the grid detection algorithm and used to determine the center coordinate of the fiducial markers by placing the circumference of the circle onto the edges of the fiducial markers.

From the initial location of the fiducial marker, the initial radius is found by increasing the radius so that $F(R,X_0,Y_0)$ is maximized. This procedure is conceptually described in Fig. 9.26. If the radius is larger than the edges of the fiducial marker, the average pixel values are decreased. This procedure limits the radius of the circle within the edges of the fiducial markers. In most cases, the initial radius stays within the fiducial markers. This procedure works well when the grid patterns overlaps onto smaller fiducial markers.

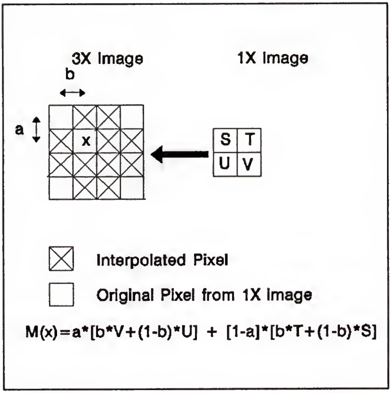

Fig. 9.25 The Bilinear Interpolation Procedure to Make 3X Magnified Image in the Gray and the Gradient Images. The S, T, U and V represent the pixel values in the original image without magnification (1X image); a and b have the value 0, 1/3, 2/3, and 1 depending upon the distance from the pixel position with the pixel value, S.

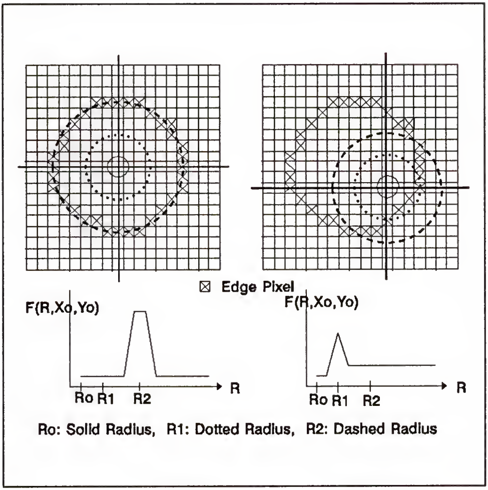

Fig. 9.26 The Procedure to Determine the Center of a Fiducial Marker in the 3X Gradient Image. The origins are the pixel locations which a user indicates. The R_0 is the default value for the radius and choose the radius, R such that $F(R,X_0,Y_0)$ is maximized. $F(R,X_0,Y_0)$ increases with R and reached to the maximum when R = R1 and $F(R,X_0,Y_0)$ decreases when the radius is larger than R1. The R1 is chosen in the procedure to estimate the radius of the fiducial markers. This figure illustrates two cases: a user indicates two possible locations for the fiducial marker detection algorithm.

Once the initial radius is found, a fine tuning procedure to find the center coordinates is carried out by changing the radius by +/-2 pixels (radius determination procedure) and moving the center (x and y coordinates) of the circle by +/-2 pixels (center determination procedure). The radius is found by selecting the radius (obtained from the center determination procedure) such that $F(R,X_0,Y_0)$ is maximized. The center coordinates are determined by choosing the center coordinates of the circle with the half radius such that $G(R/2,X_0,Y_0)$ is minimized. The half of the radius, instead of full radius, is used because the edge of the fiducial marker is smeared due to various reasons: scattered radiation [Lov89] [Boo86] [Boo91] or Veiling Glare [Nai87] [Luh90]. The half of the radius is experimentally determined with different magnification factors of the AP and lateral images. When the fiducial marker detection procedure starts, the radius obtained from the initial radius determination procedure in Fig. 9.26 is used to determine the center of the circle. The center coordinates of the circle are fixed while the radius is increased or decreased to put the circumference of the circle on the steepest region in the gradient image. These two procedures are repeated until the termination condition is satisfied.

Once the initial radius is determined from the procedure in Fig. 9.26, the fine tuning procedure is called

for. A radius and a center determination procedure are alternatively executed to get the coordinates of the circle center. This fine tuning procedure is repeated at most eight times. Based upon the experiments testing the algorithm, the fine tuning procedure determines the center coordinates after eight repetitions at most. The fine tuning procedure is illustrated in Fig. 9.27.

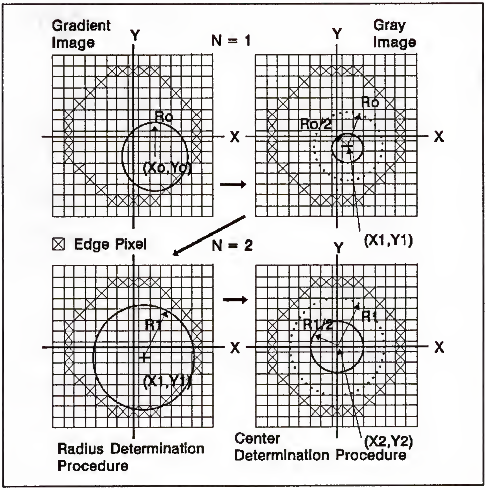

Fig. 9.27 Fine Tuning Procedure to Determine the Center Coordinates

The termination condition is satisfied when two center coordinates (one from the radius determination procedure and the other from the center determination procedure) are the same. If two coordinates are not the same, the radius determination and the coordinate determination procedure are carried out until the termination condition is satisfied. There is another termination condition (not shown in the flow chart in Fig. 9.24). The iterative procedure is terminated if the iteration is more than eight times.

The fiducial marker detection algorithm is applied with the warped image in order to demonstrate the power of the algorithm. The iterative procedure of the semi-automatic detection algorithm is shown in Fig. 9.28. The warped images with the grid patterns are used to simulate the worst clinical condition (several thick bony structures are overlapped onto the fiducial markers).

Manual Fiducial Marker Detection

The manual detection procedure is developed by using the same concept as the automatic detection procedure except using the gray image. Only the 3X gradient images are employed with manually controlled thresholding, which is very useful when the edges of the fiducial markers are seriously affected by a larger object close to the fiducial

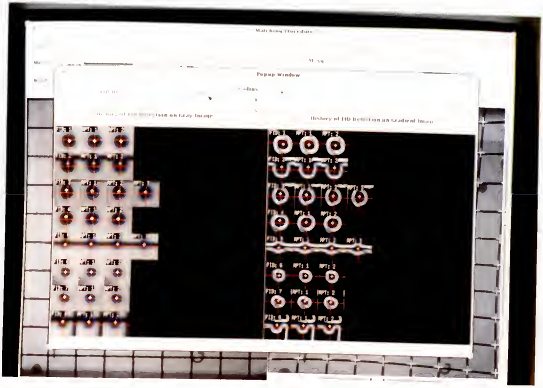

Fig. 9.28 Iterative Procedure of the Semi-Automatic Fiducial Marker Detection Algorithm. In most cases, the iterative process is being executed three to four times to get the center coordinates and the radius of the fiducial markers.

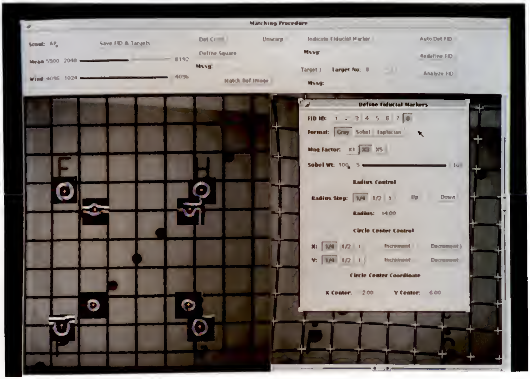

Fig. 9.29 Manual Determination of Fiducial Markers. The pop-up window shown on the right canvas is used to adjust the center coordinates and the radius of the fiducial marker in the gradient images using different weightings in the gradient represented by Eq. 9.8.

marker. The procedure is carried out by placing the circumference of the circle on the steepest boundary in the gradient image and adjusting the center coordinates and the radius by a step of 1/4, 1/2, and 1 pixel. This procedure is applied to the unwarped image and shown in Fig. 9.29 with different Sobel weighting.

Target Determination Procedure

The target determination procedure is exactly the same procedure as the manual fiducial marker detection procedure. Targets in the DA target phantom are 6 mm-diameter spherical aluminum balls and the 2 cm-solid water phantom is used to introduce some scattered radiation. The boundary of the target is easily determined by using the 3X gradient images and the manual fiducial marker detection procedure. This procedure is exactly the same procedure to determine the fiducial marker detection procedure. In Fig. 9.30, four targets (for demonstration purpose) are identified in the left canvas by using the manual procedure on the right canvas while changing the gradient called Sobel weighting.

Projective Geometry

The unwarping procedure is repeated on AP and lateral images. The target detection with a manual detection and

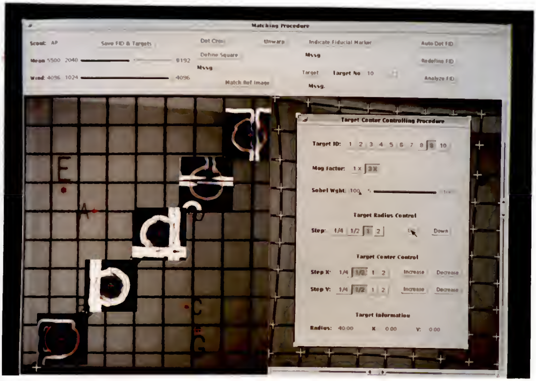

Fig. 9.30 Target Identification Procedure with DA Target Phantom Image. Different Sobel weightinhs are used to help a user to determine the optimum boundary of each target.

the fiducial marker detection with automatic and manual detection in AP and lateral images are used to calculate the coordinate using the stereotactic localization procedure cited in the paper [Sid87].

In order to quantitatively analyze the accuracy of the unwarping algorithm, the target locations in BRW coordinates are compared with those obtained using regular film radiography. The actual locations of the ten targets in three coordinates as well as the skew distance (See Fig. 2.5 for the definition of the skew distance) are summarized in Table 9.2 and the errors between two methods are summarized in Table 9.3. The statistical analysis with the ten targets are summarized in Table 9.4. The absolute distance differences of the ten targets using the film angiographic localization and the digital angiographic localization is 0.26 mm +/- 0.0 25mm.

The skew distance is larger for the targets in the boundary (target number 1 and 10). This should be further investigated using other phantom whose targets should be identified using two methods: film angiograpgy and digital angiography [Sid87].

Table 9.2 Target Coordinates in mm in the Stereotactic Coordinates and skew distance in mm. These coordinates are determined by using the projective geometry with the unwarping algorithm. The skew distances of the target 1 and 10 are larger than that of other targets.

No	AP	LAT	Ax	Skew Distance
1	+35.66	-61.22	+71.55	0.61
2	+28.29	-48.97	+57.10	0.61
3	+21.05	-36.63	+42.71	0.[illegible]8
4	+13.96	-24.72	+28.29	0.42
5	+7.17	-12.10	+14.05	0.33
6	+0.03	-0.07	-0.07	0.08
7	-6.56	+12.56	-14.16	0.15
8	-13.38	+24.96	-28.27	0.27
9	-20.57	+36.98	-42.32	0.37
10	-27.25	+49.43	-56.34	0.94

Table 9.3. Coordinate Difference between Digital Radiography and Film Radiography (in mm)

No	AP	LAT	Ax	Skew	Distance
1	-0.07	+0.23	+0.25	+0.78	+0.35
2	-0.13	+0.17	+0.15	+0.01	+0.26
3	-0.14	+0.32	-0.04	-0.07	+0.35
4	-0.19	-0.06	+0.17	+0.21	+0.26
5	-0.02	+0.17	+0.2[illegible]	+0.20	+0.26
6	-0.07	+0.09	-0.13	-0.04	+0.17
7	+0.04	+0.19	-0.13	-0.04	+0.17
8	+0.16	+0.34	-0.13	+0.04	+0.40
9	-0.04	+0.05	-0.14	+0.01	+0.16
10	+0.14	+0.03	-0.09	+0.18	+0.17

Table 9.4 Statistical Analysis with Ten Targets

No	Item	Average (mm)	One Std (mm)
1	AP	-0.02	0.035
2	Lat	+0.15	0.038
3	Ax	-0.06	0.047
4	Skew	+0.13	0.075
5	Distance	+0.26	0.025

Experiment with Stereotactic Phantom Base

In order to test the accuracy of the unwarping algorithm the phantom base is also used to get the coordinates of the tip of the probe. The tip is set to three positions: (0,0,0). The coordinates are compared with three measurements: mechanical setup of the phantom base, film angiography and digital angiography. The correlation data are listed in Table 9.5. The axial coordinate of the digital angiography has larger difference from that of the film angiography because of the finite resolution in the axial coordinates even though the AP and lateral coordinates are less than 0.1 mm. The manual fiducial marker detection procedure using the 3X gradient images are used to identify the tip of the probe in the phantom base.

Table 9.5 Target Coordinates with Phantom Base

No	localization	AP (mm)	Lat (mm)	Ax (mm)	Skew (mm)
1	mechanical setup	+0.0	+0.0	+0.0	NA
2	film angiography	+0.27 +/-0.04	0.12 +/-0.03	0.17 +/-0.05	0.14 +/-0.02
3	digital angiography	0.27 +/-0.08	0.05 +/-0.06	0.78 +/-0.06	0.35 +/-0.05

Conclusion

From the correlation analysis between the digital radiography and the film radiography, the error is about 0.26 +/-0.025 mm. Two methods of the fiducial marker detection procedures are used because some fiducial markers are overlapped with the grid patterns. When the target phantom images without the grid plate are used, the fiducial marker detection procedure can be automatically determined by using the automatic fiducial marker detection procedure.

In order to decrease the errors further, several methods could be included in the unwarping procedure. First, the sub-pixel detection of the cross should be employed. In the proposed method (cross detection algorithm) in this chapter, the cross location is within one-pixel accuracy. The reason is that one-pixel

uncertainty is washed away when many squares (consisting of four crosses) are involved between the fiducial markers. Statistically, the one-pixel uncertainty disappears. When the distance between the fiducial markers are smaller than the distance shown in this chapter, the one-pixel uncertainty can affect the accuracy.

Sub-pixel accuracy can be implemented in two methods. The first uses interpolation based upon the least-square fitting to estimate the horizonal and the vertical lines and the second method uses using polynomial fitting functions. The first procedure will be illustrated in Fig. 9.31. for horizontal line detection with sub-pixel accuracy. Several smaller lines (three line segments are shown in Fig. 9.31) are estimated with one-pixel accuracy (same as the line detection procedure). The least-square fitting with three points is used to estimate the coefficients in the linear equation, Y = A*X + B.

When the line has zero slope as in Fig. 9.32, the previously mentioned method fails to estimate the B coefficient (intersection of the linear equation in Y = A*X + B). Because of the discrete nature of the digital imaging, the estimation procedure for the coefficient B should use the shapes of the profile of the summed pixel values.

In order to improve the accuracy of the automatic fiducial marker detection, the step (used to move the circle or increase or decrease the radius of the circle) should be less than one pixel in the 3X image. The second method for sub-pixel accuracy uses polynomial fitting functions as in Eq. 9.2. As the order (N) is increased, more constrains are necessary. For example, for N = 3, the W matrix in Eq. 9.4 and 9.5 becomes 6 * 6. The minimum number of the crosses are 16, which means that at least 9 squares should be employed. When the number of crosses is 16, the exact solution is possible. Therefore, each cross should be determined with sub-pixel accuracy.

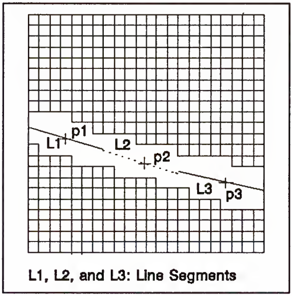

Fig. 9.31 Procedure to Estimate the Horizontal Line with the Least-Square Fitting with Three Line Segments (L_1, L_2 and L_3). Three points (P_1, P_2 and P_3) are used to estimate the coefficient of the horizontal line.

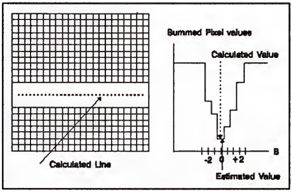

Fig. 9.32 Illustration to Estimate the Coefficient of the Linear Function with Sub-pixel Accuracy. The B of the linear function is 0 in this example, but is between 0 to 1. Based upon the profile, the B values should be estimated in order to get the B with sub-pixel accuracy.

CHAPTER 10
CONCLUSION AND FUTURE WORK

Introduction

In this dissertation the BRW stereotactic frame and its fixtures were modified to be compatible with the magnetic resonance (MR) scanner without any major modification in the hardware and software of the UF radiosurgery system. This MR-compatible BRW head ring (MR ring) and its fixtures have been used to treat five stereotactic patients with acoustics neuroma, meningiomas and metastatic disease. In order to improve the signal-to-noise ratio (SNR), a custom-made head coil was fabricated. The head coil was implemented by using a linear type birdcage resonator. The combination of the MR ring and the birdcage head coil has been used to treat more than fifteen stereotactic patients as well as seven depth electrode placement patients. The correlation between CT and MR images was investigatedd with a water phantom and patient scans. Also, the MR registration procedure was introduced using least-square fitting. This procedure should be verified with a specially built 3D phantom.

Digital radiography was reviewed as a secondary imaging modality for venous radiosurgery targets. A geometric transformation was employed to remove spatial distortion, which prevents the direct use of digital radiography in the application of stereotactic radiosurgery. The bilinear transformation and the sub-pixel detection algorithm for fiducial markers in the angio localizer were utilized to achieve the error of 0.4 mm (average distance for ten targets between two coordinates using the film angiography and the digital radiography), which is on the order of the errors in the film angiography.

Magnetic Resonance Imaging

In order to accurately register the MR imaging as a part of the stereotactic radiosurgery system, three factors should be considered: (1) nonlinearity of the gradient magnetic fields, (2) frame artifacts and (3) susceptibility artifacts. The nonlinearity of the gradient magnetic fields can introduce mis-registration of the MR images. In order to remove the nonlinearity of the gradient magnetic field, a calibration phantom with 2D and 3D structures should be fabricated in order to be used when a patient's images are registered during the image registration procedure.

The frame artifacts introduce spatial distortion of up to

4 mm (approximtaley 3 cm from the sterotactic frame) with a water phantom test. The frame artifact can be reduced by using material which is non-ferromagnetic (for example, titanium alloy) as well as satisfying mechanical strength. The material should be carefully chosen and experimentally verified with a phantom which can give spatial correlation with CT.

In order to reduce patient-induced artifacts such as susceptibility artifacts, the DANTE (Delays Alternating with Nutations for Tailored Excitation) pulse sequence may be the best choice to analyze susceptibility distribution in the brain [Gee89] [Mos90] [Blo87] [Fre78] [Cal91]. The DANTE pulse technique has been also used to investigate the heart wall with motion [Axe89] [Blo87] or magnetic susceptibility effects [Vil88]. This technique can be implemented on the GE or the Siemens MR unit with pulse programming language as a means of drawing the grid patterns in the 2D images. Even though there is still uncertainty about the spatial distortion in axial planes, the DANTE pulse sequence can give us more information about the susceptibility artifacts.

With the DANTE pulse technique combined together, the MR images are reliably used with CT to define tumors and also to estimate the dose distribution in critical organs. The MR images can be used with the unwarping algorithm developed with

digital radiography, so 2D unwarped MR images can be achieved to help a physician to directly use the MR images during the computer treatment planning [Xu90] [You89] [Wil87] [Wis88].

Digital Angiography

The unwarping algorithm with sub-pixel fiducial marker detection algorithm was developed to correct the digital radiography. The fiducial marker detection algorithm still needs user intervention to define the center of the fiducial markers. The correction algorithm also needs user intervention to define the area-of-interest in the calibration images. A fully automatic correction algorithm could be employed, thus reducing the user intervention as well as improving the accuracy of digital radiography. Therefore, digital radiography could be successfully used to take advantage of image processing techniques like digital subtraction angiography as well as flow studies of the blood vessels [Ter83] [See85] [Van88] [Sei88].

APPENDIX A
BIO-SAVART LAW

For an general arrangement of current carrying wires, the magnetic field, B, can be caluclated by integrating the value from individual current elements (dl) using Eq. A.1,

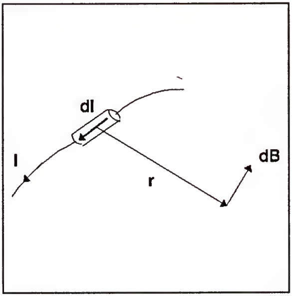

$$\overline{dB}\Big|_{at\ P(x,y)} = \frac{u_0}{4\pi} I \frac{\overline{dl} \times \overline{r}}{|r|^3} \qquad Eq. A.1$$

where dB, dl and r are vectors.

APPENDIX B
SIGNAL-TO-NOISE RATIO (SNR)

The signal intensity of a picture element depends upon the magnetization in the corresponding volume element. The MR signal is a linear function of the voxel size V which is computed from the field-of-view (FOV), matrix size (MS), and slice thickness (ST).

$$V = dx * dy * dz$$

$$= (FOV_{phase} * FOV_{frequency} * TH) / (N_{phase} * N_{frequency}) \quad \text{Eq. B.1.}$$

where N_{phase} represents the number of phase encoding steps

$N_{frequency}$ represents the number of sampling points.

A certain amount of noise is added to the MR signal. The noise (N) is considered to be uncorrelated and distributed uniformly across the MR image. Ths summing of signal (S) over several measureemnts does not apply to randomly distributed positive or negative noise. Based upon statistics, uncorrelated noise sould increase only with the square root of the number of acquisitions. As a result of

S/N is inversely proptional to $NEX^{1/2}$ Eq. B.2.

where NEX is the number of excitation for MR imaging.

As previoulsy mentioned, noise is also a function of the receiever bandwidth inculding the following dependence:

N is proportional to $BW^{1/2}$ Eq. B.3

where, BW is the bandwidth of the receiver of the MR scanner.

The Eqs B.1., B.2. and B.3. are combilned into the following formula:

S/N is proportional to

$$(FOV^2 * TH * NEX^{1/2}) / (N_{phase} * N_{frequency} * BW^{1/2}) \qquad \text{Eq.B.4.}$$

The most important SNR relationship may be derived from this formula. For example, the SNR decreases by a factor of two by halving the slice thickness. In radiosurgery application, the NEX, the N_{phase}, the $N_{frequency}$, the FOV and the BW are set to 2, 512, 512, 345mm and 100KHz.

APPENDIX C
STATISTICS IN BACKGROUND NOISE

In order to set a threshold to discriminate a rod from a background in MR slice image, the statistical data such as average or standard deviation of the background should be chosen. The statistical data is also a function of window size because of the random nature of the background noise. The average and the standard deviation of the noise region are obtained with different window sizes. Those values start to converge with approximately 21*21 window size. The region is set to 41*41 to get the average and the standard deviation of the noise region considering a margin. The relationship between the statistical data and the window size is demonstrated in Fig. C.1.

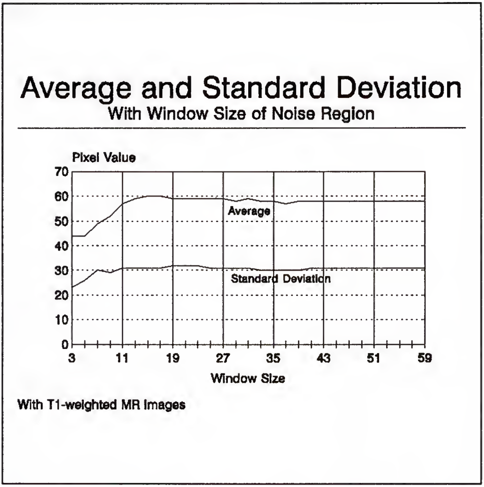

Fig. C.1 Average and Standard Deviation of the Noise Region Defined in Fig. 6.1 and 6.2. The window is set to 41*41 to determine the statistical data of the random noises in the noise region.

APPENDIX D
SPATIAL DISTORTION OF DIGITAL RADIOGRAPHY

The distortion analysis was carried out using biplane film angiography and the digital angio target phantom. The target phantom is placed such that eight fiducial markers are located in the middle of each view, thus minimizing the spatial distortion of the fiducial markers. The fiducial markers for each view were defined using the 2-dimensional digitizer at Shands Cancer Center. The distortion of each view was represented by "flatness", which is the measure of spatial distortion between estimated and measured coordinates of any measured fiducial marker from the film image. Theoretically, the coordinates of any two fiducial markers can be determined by the remaining six fiducial markers [Sid87]. The flatness is defined as the average deviation of all fiducial markers for each view. Flatness may be improved when the fiducial markers are placed in the peripheral regions of the digital images. This procedure is repeated in both AP and lateral views.

Ten targets are also selected by a user. The coordinate of each target is determined by averaging eight estimated coordinates, which are obtained with different sets of

fiducial markers in each view. The spatial distortion is represented by the coordinate differences between the cut film and the digital images. This information is shown in Table D. The flatness are approximately 2 mm to 4 mm in the AP and lateral views. The spatial distortion of the target is more pronounced with the boundary targets, for example, targets 1 and 10. In the middle of the digital images with targets 3, 4 and 5, the spatial distortion is approximately less than 0.5 mm in either AP or lateral or trans-axial plane.

Table D Spatial Distortion of Digital Images

Target Number	dAP (mm)	dLat (mm)	dAx (mm)
1	-0.7	+4.3	-3.6
2	+0.8	+2.0	-1.3
4	+0.5	+0.8	-0.2
4	+0.5	+0.2	+0.1
5	+0.3	-0.1	-0.2
6	+0.2	+0.1	-0.4
7	+0.1	+0.2	-0.6
8	-0.2	+0.2	-0.4
9	+0.3	-0.2	+0.4
10	+0.1	-1.3	+2.4

Note: The flatness was ranges from 2mm to 4mm in the AP and lateral views.

REFERENCE LIST

Aug87 N. Augustiny, G.K. von Schulthess, D. Meier, and P. Boesiger, "MR Imaging of Large Non-ferromagnetic Metallic Implants at 1.5 T," J. of Computed Tomography, 11(4), pp.678-683, July/Aug 1987

Bal82 D.H. Ballard and C.M. Brown, "Computer Vision", Prentice-Hall Inc. 1982

Bal92 James M. Balter, Charles A. Pelizzari, and George G.Y. Chen "Correlation of Projection Radiograph in Radiation Therapy Using Open Curve Segments and Points," Med. Phys. 19(2), pp. 329-334, Mar/Apr 1992

Ben91 A. Bengtsson and J. Eklundh, "Shape Representation by Multiscale Contour Approximation," IEEE transaction on pattern analysis and machine intelligence, Vol.13, No.1, pp.85-93, January 1991

Bol91 R.M. Bolle, and B.C. Vemuri, "On Three-Dimensional Surface Reconstruction Methods," IEEE Transaction on Pattern and Machine Intelligence, Vol.13, No.1, pp.1-12, January 1991

Boo86a F.L. Bookstein, "Size and Shape Spaces for landmark data in Two Dimensions", Statistical Science, Vol.1, No.2, pp.181-242, 1986

Boo86b J.M. Boone, B.A. Arnold, and J.A. Seibert, "Characterization of the Point Spread Function and Modulation Transfer Function of Scattered Radiation Using a Digital Imaging System", Med. Phys. 13(2), pp.254-256, Mar/Apr 1986

Boo91 J.M. Boone, J.A. Seibert, W.A. Barrett, and E.A. Blood, "Analysis and Correction of Imperfections in the Image Intensifier-TV-digitizer Imaging Chain", Med. Phys. 18(2), pp.236-242, Mar/Apr 1991

Bor87 J.A. Borrello, T.L. Chenevert, C.R. Meyer, A.M. Aisen, and G.M. Glazer, "Chemical Shift-based True Water and Fat Images: Regional Phase Correction of Modified Spin-Echo MR Images," Radiology, vol.164. No.2, pp.531-537 1987

Bov90 F.J. Bova, "Radiation Physics," Neurosurgery Clinic of North America, Vol.1 No.4 pp.909-931, Oct 1980

Bov91 F.J.Bova and W.A.Friedman, "Stereotactic Angiography: An Adequate Database for Radiosurgery?," Int. J. Rad. Onc. Biol. Phys, Vol:20, pp.891-895, 1991

Bov93 F.J. Bova, W.A. Friedman and W.M. Mendenhall, "Stereoatctic Radiosurgery," Medical Progress through Technology, 18: pp.239-251, 1993

Bra88 M. Brant-Zawadzki, "MR Imaging of the Brain", Radiology, Vol.166, No.1, 1988

Cal91 P.T. Callaghan, "Principle of Nuclear Magnetic Resonance Microscopy," Oxford Science Publication, 1991

Cas76 L.W. Casperson, P. Spielgler, and J.H. Grollman, Jr., "Characterization of Aberration in Image-Intensified Fluoroscopy," Medical Physics, Vol.3, No.2 pp.103-106, Mar/Apr 1976

Cha87 D.P. Chakraborty, "Image Intensifier Distortion Correction", Medical Physics, 14(2), Mar/Apr, pp.249-pp.252, 1987

Che88 Z. Chen and D. Perng, "Automatic Reconstruction of 3D Solid Objects From 2D Orthographic Views", Pattern Recognition, Vol.21, No.5, pp.439-449, 1988

Con87 B.R. Condon, J. Patterson, D. Wyper, M. Inst, A. Jenkins, and D.M. Hadley, "Image Nonuniformity in Magnetic Resonance Imaging: its Magnitude and Methods for its Correction", The British Journal of Radiology, 60, pp.83-87, 1987

Cut60 L.J. Cutrona, E.N. Leith, C.J. Palermo, and L.J. Porcello, "Optical Data Processing and Filtering Systems," IRE trans. Inf. Theory, Vol.IT-16, pp.380-400, 1960

Cur90 T.S. Curry, J.E. Downey, R.C. Murry, Jr. "Christensen's Physics of Diagnostic Radiology," fourth edition, Lea and Febiger, 1990

Dix88 R.L. Dixon, MRI: Acceptance Testing and Quality Control, published by Medical Physics Publishing Corporation, Madison, Wisconsin, 1988

Dun86 J.G. Dunham, "Optimum Uniform Piecewise Linear Approximation of Planar Curves," IEEE Transaction on Pattern and Machine Intelligence, Vol. PAMI-8, No.1 Jan. 1986

Fab85 J,I, Fabrikant, J.T. Lyman, and K.A. Frankel, "Heavy Charge Particle Bragg peak Radiosurgery for Intracranial Vascular Disorders," Radiat Res 104 [Suppl] S244-S258, 1985

For85 W.D. Foley, M.W. Milde, "Intra-Arterial Digital Subtraction

Angiography," Radiologic Clinics of North America, Vol.23, No.2, pp.293-318, 1985

Fra87 B.A. Fraass, D.L. McShan, R.F. Diaz, R.K. Ten Haken, A.Aisen, S. Gebarski, G. Glazer, and S. Lichter, "Integration of Magnetic Resonance Imaging into Radiation Therapy Treatment Planning: 1. Technical Consideration," Int. J. Radiation Oncology Biol. Phys. vol:13, pp.1897-1908, 1987

Fen90 L.E. Fenil and C.E. Metz, "Propagation and Reduction of Error in Three-Dimensional Structure determined from Biplane Views of Unknown Orientation", Med. Phy. 17(6) Nov/Dec, 1990

Fri92 W.A. Friedman, F.J. Bova, R. Spiegelmann, "Linear Accelerator Radiosurgery at the University of Florida," Neurosurgery: Clinic of North America, Vol. 3 No.1 January pp.141-161, 1992

Fuj88 H. Fujita, M.L. Giger, and K. Doi, "Investigation of Basic Imaging Properties in Digital Radiography. 12. Effects of Matrix Configuration on Spatial Resolution," Med. Phys. 15(3) pp.384-391 May/Jun, 1988

Gee89 H. Geen, X. Wu, P. Xu, J. Friedrich, and R. Freeman, "Selective Excitation at Two Arbitrary Frequencies. The Double-DANTE Sequence," Journal of Magnetic Resonance, 81, pp.646-652, 1989

Gig85 M.L. Giger, and K. Doi "Investigation of Basex Imaging Properties in Digital Radiography. 3. Effects of Pixel Size on SNR and Threshold Contrast," Med. Phys. 12(2), Mar/Apr, 1985

Gig88 M.L. Giger, K. Doi, and H. MacMahon, "Image Feature Analysis and Computer-Aided Diagnosis in Digital Radiography. 3. Automated Detection of Nodules in Peripheral Lung Fields," Med. Phys. 15(2), pp.158-166, Mar/Apr, 1988

Gol90 J.E. Golston, R.H. Moss, and W.V. Stoecker, "Boundary Detection in Skin Tumor Images: An Overall Approach and Radial Search Algorithm," Pattern Recognition, Vol.23, No.11, pp.1235-1247, 1990

Gon87 R.C. Gonzalez, P. Wintz, "Digital Imaging Processing," second edition, Addison-Wesley Publishing Company, 1987

Gro73, F.W. Grover, "Inductance Calculation," Dover, New York, 1973

Har89 M.D. Harpen, "Analysis of Capacitive Coupling and Associated Loss for a Solenoidal Magnetic Resonance Imaging Radio-Frequency Coil," Med. Phys. 16(2), pp.234-238, Mar/Apr, 1989

Har90 M.D Harpen, "Harmonic Structure of Cylindrical Imaging

Coils", Med. Phys. 17 (4), pp.686-691, Jul/Aug 1990

Har91 M.D. Harpen, "Theoretical Description of the Interaction Between Birdcage Coils and Lossy Samples," Med. Phys. 18(5), pp.1052-1055, Sep/Oct 1991

Har85 G.H. Hartman, W. Schlegel, V. Sturm, B. Koba, O. Pasty, W.J. Lorenz, "Cerebral Radiation Surgery Using Moving Field Irradiation at a Linear Accelerator Facilities," Int J Radiat Oncol Biol Phys 11:pp.1185-1192, 1985

Hay85 C.E. Hayes, W.A. Edelstein, J.F. Schenck, O.M. Mueller, and M. Eash, "An Efficient, Highly Homogeneous Radiofrequency Coil for Whole-Body NMR Imaging at 1.5T," Journal of Magnetic Resonance 63, pp.622-628, 1985

Hei87 M.P Heilbrun, P.M. Sunderland, P.R. McDonald, T.H. Wells, Jr., E. Cosman, and E. Ganz, "Brown-Roberts-Wells Stereotactic Modifications to Accomplish Magnetic Resonance Imaging Guidance in Three Planes", Appl. Neurophysiol. 50: pp.143-152, 1987

Hen91 C.J. Henri, D.L. Collins, and T.M. Peters, "Multimodality Image Integration for Stereotactic Surgical Planning," Med. Phys. 18(2), pp. 167-177, Mar/Apr, 1991

Hin88 D.B. Hinshaw, Jr., B.A. Holshouser, H.I.M. Engstrom, A.H.L. Tjan, E.L. Christiansent, and W.F. Catelli, "Dental material Artifacts on MR Images", Radiology, Vol.166, No.3, 1988

Hol84 B.A. Holland, M. Brant-Zawadzki, D. Norman, and T.H Newton, "Magnetic Resonance Imaging of Primary Intracranial Tumors: A Review", Int. J. Radiation Oncology, Biol. Phys. Vol. 11, pp.315-321, 1984

Huh93 S.N. Huh, F.J. Bova, J.R. Fitzsimmons, W.A Friedman, "Integration of MR-compatible BRW Head Ring and Custom-made Birdcage Resonator in Stereotactic Radiosurgery", AAPM Works-in-Progress Session, presented to 35th Annual conference of AAPM, Washington, Oct. 28 1993

Huh92 S.N. Huh, "Design Concept of Linear Birdcage Resonator for Stereotactic Radiosurgery System", (internal report), Department of Radiation Therapy, Shands Cancer Center, University of Florida, 1992

Huh92, S.N. Huh, "Introduction to Radiosurgery and Recent Progress," presented to the 35th Florida Society of Radiation Therapists (FSRT), Daytona, Nov.7 1992

Kaw86 A. Kawanaka and M. Takagi, "Estimation of Static Magnetic Field and Gradient Fields from NMR Image", J. Phys. E: Sci.

Instrum. 19, pp.871-875, 1986

Kje77 R.N. Kjellberg, C.E. Roberson, and G.H.Adams, "Bragg-Peak Proton Beam Treatment of Arterivenous Malformation of the Brain," Exe. Med. 433, pp.181-186, 1977

Kon89 D. Kondziolka, E.J. Dolan, and R.R. Tasker, "Functional Stereotactic Surgery and Stereotactic Biopsy Using a Magnetic Resonance Imaging Directed System: Results and Comparison to CT Guidance," Stereotact Funct Neurosurgery, 54+55, pp.237-249, 1989

Kon93 D. Kondziolka, P.K. Dempsey, L.D. Lunsford, J.R.W. Kestle, E.J. Dolan, E. Kanal, and R.R. Tasker, "A Comparison between Magnetic Resonance Imaging and Computed Tomography for Stereotactic Coordinate Determination," Neurosurgery, Vol.30, No.3, pp.402-407, March, 1993

Kru84 R.A. Kruger and S.J. Riederer, Basic Concept of DSA, G.K. Hall Medical Publisher, Boston, Massachusetts, 1984

Lar58 B. Larson, L. Leksell, B. Rexed, P. Sourander, W. Maiv, B. Anderson, "The High Energy Proton Beams as a Neurosurgical Tool," Nature, 182 pp.1222-1223, 1958

Lar74 B. Larsson, K. Liden, and B. Sarby, "Irradiation of Small Structures through the Intact Brain," Acta. Radiol. 13, pp.512-534, 1974

Lau90 H.H. Ehricke and G. Laub, "Integrated 3D Display of Brain Anatomy and Intracranial Vasculature in MR Imaging", J. Computer Assisted Tomography, 14(5): pp.846-852, Sep/Oct, 1990

Lek51 L. Leksell, "The Stereotactic Method and Radiosurgery of the Brain", Acta. Chir. Scan 102: pp.316-319, 1951

Lek83 L. Leksell, "Stereotactic Radiosurgery", J. Neurosurg Psych. 46: pp.797-803, 1983

Loo85 L.D. Loo, K. Doi, and C.E. Metz, "Investigation of Basic Imaging Properties in Digital Radiography. 4. Effects on Unsharp Masking on the Detectability of Simple Pattern," Med. Phys. 12(2), Mar/Apr, 1985

Lov87 L.A. Love and R.A. Kruger, "Scatter Estimation for a Digital Radiographic System Using Convolution Filtering," Med. Phys. 14(2), pp.178-185, 1987

Lue85 K.M. Luedeke, P. Roeschman, and R. Tischler, "Susceptibility Artefacts in NMR Imaging", Magnetic Resonance Imaging," Vol.3, pp.329-343, 1985

Luh90 R. Luhta and J.A. Rowlands "Origins of Flare in x-ray Image Intensifiers", Med. Phys. 17(5), pp.913-921, Sep/Oct (1990)

Lun89 L.D. Lunsford, J. Flickinger, C.T. Lindner, A Maitz, "Stereotactic Radiosurgery of the Brain Using the First United States 201 Cobalt-60 Source Gamma Knife," Neurosurgery, 24: pp.151-159, 1989

Lut88 W. Lutz, K. Winston, N. Maleki, " A System for Stereotactic Radiosurgery with a Linear Accelerator", Int J Rad Oncol Biol Phys 14: pp.373-pp.381, 1988

Lux93 G. Luxton, Z. Petrovich, G. Jozsef, L.A. Nedri, and M.L.J. Apuzzo, "Stereotactic Radiosurgery: Principles and Comparison of Treatment Methods", Neurosurgery, Vol.32, No.2 February, pp.241-259, 1993

Mal87 J.A. Malko and R.C. Nelson, "Controlled Eddy Currents: Application to MR Imaging," J. of Computer Assisted Tomography, 11(6), pp.1044-1049, 1987

Meh90 R. Mehrotra, and S. Nichani, "Corner Detection," Pattern Recognition, Vol.23, No.11, pp.1223-1233, 1990

Mor86 P.G. Morris, "Nuclear Magnetic Resonance Imaging in Medicine and Biology", Oxford Science Publication, 1986

Mos90 T.J. Mosher and M.B. Smith, "DANTE Tagging Sequence for the Evaluation of Translational Sample Motion", Magnetic Resonance in Medicine, 15, pp.334-339, 1990

Mos91 T.J. Mosher and M.B. Smith, "Magnetic Susceptibility Measurement Using a Double-DANTE Tagging (DDT) Sequence", Magnetic Resonance in Medicine, 18, pp.251-255, 1991

Mos92 D.C. Moss, "Conformal Stereotactic Radiosurgery with Multileaf Collimation", Ph.D Dissertation, University of Florida, 1992

Nai87 S. Naimuddin, B. Hasegawa, and C.A. Mistretta, "Scatter-glare Correction Using a Convolution Algorithm with Variable Weighing", Med. Phys. 14(3), pp.330-334, May/Jun, 1987

Nel85 J.A. Nelson, "Newer Subtraction and Filtration Techniques", Radiologic Clinics of North America," Vol.23, No.2, pp.185-192, June, 1985

Oha72 D.A. O'handley, W.B. Green, "Recent Development in Digital Image Processing at the Image Processing at the Jet Propulsion Laboratory," Proceedings of the IEEE, Vol.60, No.7, July, 1972

Oha86 K. Ohara, H. Chan, K. Doi, M.L. Giger, and H. Fujita,

"Investigation of Basic Imaging Properties in Digital Radiography. 8. Detection of Simulated Low-Contrast Objects in Digital Substraction Angiographic Images," Med. Phys 13(3) pp.304-311, May/Jun, 1986

Ovi85 T.W. Ovitt, J.D. Newell, "Digital Subtraction Angiography: Technique, Equipment, and Techniques," Radiologic Clinics of North America, Vol.23 No.2 June, pp.177-pp.184, 1985

Pas91 R.J. Pascone, B.J. Garcia, T.M. Fitzerald, T, Vullo, R. Zipagan, and P.T. Cahill, "Generalized Electrical Analysis of Lowpass and Highpass Birdcage Resonator," Magnetic Resonance Imaging, Vol.9, pp.395-408, 1991

Pel89 C.A. Pelizzari, G.T.Y Chen, D.R. Spelbring, and R.R. Weichselbaum, "Accurate Three-Dimensional Registration of CT, PET, and/or MR Images of the Brain", J. of Computer Assisted Tomography 13(1):20-26, January/February, 1989

Per87 T.K. Peters, J. Clark, P.M. Dragova, and A. Olivier, "Stereotactic Surgical Planning with Magnetic Resonance Imaging, Digital Substraction Angiography and Computed Tomography", Proceeding of the Meeting of the American Group for Stereotactic and Functional Neurosurgery, Montreal, Appl. Neurophysiol 50: 33-38, 1987

Phi92 Stereotactic Radiosurgery Operator's Manual by Philips Medical System, 1992

Pic87 D.R. Pickens, and R.R. Price, "Digital Image Motion Correction by Spatial Warp Methods", Med. Phy. 14(1), pp.56-61, Jan/Feb, 1987

Pod88 E.B. Podgorsal, A. Oliver, A. Pla, M. Lefebvre, and P.Y. Hazel, "Dynamic Stereoatctic Radiosurgery," Int. J. Radiat. Oncol. Biol. Phys. 14:pp.115-126, 1988

Pra78 W.K. Pratt, "Digital Imaging Processing", John Wiley and Sons, Inc. 1978

Pri90 R.R. Price, L. Axel, T. Morgan, R. Newman, W. Perman, N. Schneiders, M. Selikson, M. Wood, S.R. Thomas, "Quality Assurance Methods and Phantoms for Magnetic Resonance Imaging: Report of AAPM Nuclear Magnetic Resonance Task Group No.1," Medical Physics, 17(2), Mar/Apr, pp.287-295, 1990

Rei92 D.A. Reimann and M.J. Flynn, "Automated Distortion Correction of X-ray Image Intensifier Image," Conference Record of the 1992 IEEE Nuclear Science Symposium and Medical Imaging Conference, Vol.2, pp.1339-1341, Orlando, Florida, 1992

Rit85 R.T. Ritchings, A.C.F. Colchester, and H.Q. Wang, "Knowledge-

based Analysis of Carotid Angiograms," Image and Vision Computing, vol.3, No.4, pp.217-222, November, 1985

Rou91 J. Rousseau, P. Clarysse, S. Blond, D. Gibon, C. Vasseur, and X. Marchandise, "Validation of a New Methods from Stereotactic Localization using MR Imaging", J. Computed Tomography," pp.291-296, Mar/Apr, 1991

Rud91 S. Rudin, D.R. Bednarek, R. Wong, "Accurate Characterization of Image Intensifier Distortion," Medical Physics, 18(6), Nov/Dec, pp.1145-pp.1151, 1991

Saw87 C.B. Saw, K. Komanduri, and N. Suntharalingam, "Coordinate Transformations and Calculation of the Angular and Depth Parameter for a Stereotactic System," Med. Phys. 14(6), Nov/Dec 1987

Sch92 L.R. Schad, H.H Ehricke,B. Wowra, G. Layer, R. Engenhart, H.U. Kauczor, H.J. Zabel, G. Brix, W.J. Lorentz, "Correction of Spatial Distortion in Magnetic Resonance Angiography for Radiosurgical Treatment Planning of Cerebral Arteriovenous Malformation," Magnetic Resonance Imaging, Vol.10, pp.609-pp.621, 1992

See85 J.F. Seeger, R.F. Carmody, "Digital Subtraction Angiography of the Arteries of the Head and Neck," Radiologic Clinics of North America, Vol.23, No2, June, 1985

Sei88 W. Seidlecki, K. Siedlecka, and J. Sklansky, "An Overview of Mapping Techniques for Exploratory Pattern Analysis," Pattern Recognition, Vol.21, No.5, pp.411-429, 1988

Sie88 Siemens Magnetom SP/Magnetom SP4000 Applications Guide Version A2.5, Siemens Co., Germany, 1989

Sot88 A. Sotgiu, G. Gualtiere, and R. Pascone, "Highly Homogeneous Circularly Polarized RF Field for Whole Body NMR Imaging," Magnetic Resonance Imaging, Vol.6, pp.249-254, 1988

Spi92 R. Spiegelmann, W.A. Friedman, F.J. Bova, "Limitation of Angiographic Target Localization in Planning Radiosurgical Treatment," Neurosurgery, Vol.30, No.4, 1992

Suh90 T.S. Suh, "Optimization of Dose Distribution for the System of Linear Accelerator-based Stereotactic Radiosurgery," Ph.D. Dissertation, University of Florida, 1990

Syk91 S. Sykora, "The Limits of NMR Imaging," Magnetic Resonance Imaging, Vol.9, pp.833-838, 1991

Ter83 D. Terzopoulos, "Multilevel Computational Processes for Visual Surface Reconstruction," Computer Vision, Graphics, and

Image Processing, No.24, pp.52-96, 1983

Tho86 S.R. Thomas, R.L. Dixon, "NMR in Medicine," American Association of Physicists in Medicine, Medical Physics, Monograph No.14, 1986

Tob52 C.A. Tobias, H.O. Anger, J.H. Lawrence, "Radiological Use of High Energy Deuteron and Alpha Particle," Am J. Roentgen and Radium Ther Nucl Med 67: pp.1-pp.27, 1952

Tro89 J. Tropp, "The Theory of the Birdcage Resonator," Journal of Magnetic Resonance, 82, pp.51-62, 1989

Van88 M.W. Vannier and D.E. Gayou, "Automated Registration of Multimodality Images", Radiology, vol.169. No.3 pp.860-862, 1988

Vil87 J.G. Villemure, E. Marchand, T. Peters, G. Leroux, A. Olivier, "Magnetic Resonance Imaging Stereotaxy: Recognition and Utilization of the Commissures", Proceedings of the Meeting of the American Group for Stereotactic and Functional Neurosurgery, Montreal, Appl. Neurophysiol 50: 57-62, 1987

Vul92 T. Vullo, R.T. Zipagan, R. Pascone, J.P Whalen, and P.T. Cahill, "Experimental Design and Fabrication of Birdcage Resonator for Magnetic Resonance Imaging," Magnetic Resonance in Medicine 24, pp.243-252, 1992

Wat88 J.C. Watkins and E. Fukushima, "High-Pass birdcage coil for Nuclear Magnetic Resonance," Rev Sci Instrum, Vol.50, No.6, pp.927-931, June 1988

Wen88 R.E. Wendt, M.R. Wilcott, W. Nitz, P.H. Murphy, and R.N. Bryan, "MR Imaging of Susceptibility-induced Magnetic Field Inhomogeneities", Radiology, vol.168, No.3, pp.837-841, 1988

Wil87, M.R. Willcott, G.L. Mee, and J.P. Chesick, "Magnetic Field Mapping in NMR Imaging", Magnetic Resonance Imaging Vol. 5, No.5, 1987

Win88 K.C. Winston, W. Lutz, "Linear Accelerator as a Neurosurgical Tool for Stereotactic Radiosurgery" Neurosurgery 22: pp.454-464, 1988

Wis88 G.L. Wismer, R.B. Buxton, B.R. Rosen, C.R. Fisel, R.F. Oot, T.J. Bradley, and K.R. Davis, "Susceptibility Induced MR Line Broadening: Application to Brain Mapping", J. of Computer Assisted Tomography 12(2): pp.259-265, Mar/Apr, 1988

Xu90 Y. Xu, J.B. Balschi, and C.S. Springer, Jr.,"Magnetic Susceptibility Shift Selected Imaging:MSSI" Magnetic Resonance in Medicine, 16, pp.80-90, 1990

You89 I.R. Young, G.M. Bydder, S. Khenia, and A.G. Collins, "Assessment of Phase and Amplitude Effects due to Susceptibility Variation in MR Imaging of the Brain", J Computer Assisted Tomography, 13(3): pp.490-494 May/June 1989

BIOGRAPHICAL SKETCH

Soon-Nyung Huh was born on January 28, 1957, in Seoul, Korea. He grduated from KyungDong High School and HanYang University in Korea. He received a Bachelor of Science in the Department of Electronic Engeering, HanYang University in 1979. He had worked for seven years as an electrical engineer at the Institute of Technology and Development, GoldStar Electric company. He came to the United States to continue studying the electrical engineering. He earned a Master of Engineering at the Electrical Engineering, University of Florida. In 1989, he switched to the Nuclear Engineering Science to study the medical physics in the doctoral program. Since 1989, he had been involved in several projects in the Department of Radiation Oncology at the University of Florida: Megavolatge Imaging System (MVI), Electron Beam Dosimetry, and Stereotactic Radiosurgery System. He is a member of the American Association of Physicist in Medicine.

I certify that I have read this study and that in my opinion it conforms to acceptable standards of scholarly presentation and is fully adequate, in scope and quality, as a dissertation for the degree of Doctor of Philosophy.

Frank J. Bova, Chair
Professor of
Nuclear Engineering Science

I certify that I have read this study and that in my opinion it conforms to acceptable standards of scholarly presentation and is fully adequate, in scope and quality, as a dissertation for the degree of Doctor of Philosophy.

Janice C Honeyman

Janice Honeyman
Associate Professor of
Radiology

I certify that I have read this study and that in my opinion it conforms to acceptable standards of scholarly presentation and is fully adequate, in scope and quality, as a dissertation for the degree of Doctor of Philosophy.

Jeffrey Fitzsimmons
Associate Professor of
Radiology

I certify that I have read this study and that in my opinion it conforms to acceptable standards of scholarly presentation and is fully adequate, in scope and quality, as a dissertation for the degree of Doctor of Philosophy.

William Properzio
Associate Professor of
Nuclear Engineering Science

I certify that I have read this study and that in my opinion it conforms to acceptable standards of scholarly presentation and is fully adequate, in scope and quality, as a dissertation for the degree of Doctor of Philosophy.

William Friedman
Professor of
Neuroscience

I certify that I have read this study and that in my opinion it conforms to acceptable standards of scholarly presentation and is fully adequate, in scope and quality, as a dissertation for the degree of Doctor of Philosophy.

Lawrence T. Fitzgerald
Associate Professor of
Nuclear Engineering science

I certify that I have read this study and that in my opinion it conforms to acceptable standards of scholarly presentation and is fully adequate, in scope and quality, as a dissertation for the degree of Doctor of Philosophy.

Genevieve Roessler
Associate Professor of
Nuclear Engineering science

This dissertation was submitted to the Graduate Faculty of the College of Engineering and to the Graduate School and was accepted as partial fulfillment of the requirements for the degree of Doctor of Philosophy.

April 1994

Winfred M. Phillips
Dean, College of Engineering

Karen A. Holbrook
Dean, Graduate School